

MOLECULAR MOTOR FORCES AND NUCLEAR POSITIONING IN LIVING CELLS

By

JUN WU

A DISSERTATION PRESENTED TO THE GRADUATE SCHOOL
OF THE UNIVERSITY OF FLORIDA IN PARTIAL FULFILLMENT
OF THE REQUIREMENTS FOR THE DEGREE OF
DOCTOR OF PHILOSOPHY

UNIVERSITY OF FLORIDA

2012

© 2012 Jun Wu

To my Parents

ACKNOWLEDGMENTS

I would like to acknowledge all the people who supported me during this very important time of my life. First I would like to acknowledge the guidance and support of my advisor, Dr. Tanmay Lele. He brought me into a new world of science. He not only taught me a lot of new things, but also taught me how to learn and how to think. He is always supportive and extremely patient. His expertise helped me to select problems and complete projects, and grow to be an independent researcher. Without him, I wouldn't accomplish so much during the past five years. I also would like to thank my other committee members. Dr. Richard Dickinson is such a great teacher. I learned so much from him in and out of the class. We also had very good collaborations in most of my publications. I always enjoyed talking to Dr. Yiider Tseng. To me, he is a teacher, but also a friend. We had a lot of wonderful discussions about both research and life. Professor Pramod Khargonekar has been supportive and offered helpful advice. I would also like to thank Professor Kyle Roux for the valuable discussion and support on the nuclear movement project. I want to thank Professor Daniel Purich for holding the Cytoskeleton Journal Club through which I gained so much beyond my own research by interacting with other scientists. Professor Scott Grieshaber kindly provided some plasmids, which are of great help for my research.

I would also thank all my labmates and other students who were always helpful throughout my time in University of Florida. Jiyeon Lee taught me the basic biology lab skills at the beginning of my PhD study. I also learned from her the carefulness and patience in scientific research. Robert Russell's knowledge of biology benefited me a lot. Discussions with him always gave me good idea to improve my research, and we had an enjoyable time working together on the microtubule project. He is also a great

tennis partner. T.J. Chancellor is a good friend, and he was always helpful with the experiments and the life. David Lovett was supportive at the end of my time in the lab. Shen-Hsiu Hung in Dr. Yiider Tseng's lab has been very helpful all the time. Heather Brown and Andrea Knowlton in Professor Grieshaber's lab were very kind and helpful. I also would like to thank the master students and undergraduates who worked with me over the years, most specifically Nandini Shekhar, Agnes Mendonca and Kristen Lee. I want to specifically thank my roommate and best friend here, Robert Colmyer. He was always there whenever I needed. Without him, I wouldn't adapt to the life in US so fast and enjoy my life here so much, and his family is full of nice people.

Finally, I would like to thank all my family members who supported me throughout so many years and made my dream come true. My parents have always been encouraging, loving and have motivated me to achieve my goals. They gave a healthy body, smart brain and most importantly, they taught me how to be a better person. My uncle Daiyi Wu always gave me good advice and helped me come here to pursue my PhD.

TABLE OF CONTENTS

	<u>page</u>
ACKNOWLEDGMENTS.....	4
LIST OF TABLES.....	10
LIST OF FIGURES.....	11
LIST OF ABBREVIATIONS.....	14
ABSTRACT.....	16
CHAPTER	
1 INTRODUCTION.....	18
Nuclear Positioning is an Important Cell Function.....	18
Dynein-Based Torque Generation on the Nucleus.....	19
Actomyosin Forces on the Nucleus.....	22
Dynein Force Generation on Microtubules.....	24
Fluorescence Recovery after Photobleaching (FRAP).....	27
2 DYNEIN MOTOR FORCES ON THE NUCLEUS.....	31
Materials and Methods.....	31
Cell Culture, Plasmids and Transfection.....	31
Time-Lapse Imaging and Analysis.....	32
Immunofluorescence.....	33
Cell Shape Patterning.....	33
Results.....	34
Nuclear Rotation is a Persistent Random Walk.....	34
Cytoplasmic Dynein is Required for Nuclear Rotation in Stationary Fibroblasts.....	35
Model Formulation.....	35
Model Results.....	40
Nuclear Rotation Depends on Nuclear-Centrosomal Distance.....	41
Discussion.....	42
Summary of Findings.....	46
3 THE NUCLEUS IS IN A TUG-OF-WAR BETWEEN ACTOMYOSIN PULLING FORCES IN A CRAWLING CELL.....	57
Materials and Methods.....	57
Cell Culture, Plasmids and Transfection, Drug Treatment.....	57
Time-Lapse Imaging and Analysis.....	58
Confocal Microscopy and Protein Photo Activation.....	58

	Image Analysis	59
	Micromanipulation by Microinjector	60
	Results.....	60
	Myosin Inhibition In the Trailing Edge Causes Nuclear Motion Toward the Leading Edge without Change in Cell Shape.....	60
	Solid-Like Coupling Between the Nucleus and the Trailing Edge.....	61
	Forward Nuclear Movement does not Require Trailing Edge Detachment.....	62
	Forward Motion of the Nucleus Occurs due to Actomyosin Contraction Between the Leading Edge and the Nucleus	62
	Discussion	64
	Summary of Findings	65
4	EFFECTS OF DYNEIN MOTOR ON MICROTUBULE MECHANICS AND CENTROSOME CENTERING	75
	Materials and Methods.....	76
	Cell Culture, Plasmids and Transfection	76
	Time-Lapse Imaging and Analysis	76
	Cell Shape Patterning	77
	Laser Ablation	77
	Results.....	81
	Dynamics of Severed Microtubules	81
	Model for Dynein-Generated Microtubule Forces.....	83
	Simulations of Microtubule Buckling Dynamics	85
	Centrosome Centering by Motor-Driven Microtubules.....	86
	Discussion	89
	Summary of Findings	92
5	MODELING OF FLUORESCENCE RECOVERY AFTER PHOTBLEACHING ..	106
	Materials and Methods.....	106
	Cell Culture, Plasmids and Transfection	106
	Confocal Microscopy and FRAP.....	106
	Results.....	107
	Modeling Bleaching During Image Capture.	107
	FRAP Model to Account for Photobleaching due to Image Capture	109
	Accounting for Bleaching of Free Protein	112
	FRAP Model to Account for an Immobile Fraction.....	113
	Calculations of Normalized Recovery: the Behavior of Equation 5-6A and 6B.....	114
	Effect of the Immobile Fraction on FRAP Recovery Without Bleaching of Free Protein)	115
	Analysis of Focal Adhesion Protein Exchange	116
	Discussion	117
	Summary of the Model.....	121
6	CONCLUSIONS	128

Summary of Findings	128
Nuclear Rotation in Living Cells.....	128
Nuclear Translation in Living Cells	128
Effects of Dynein on Microtubule Mechanics and Centrosome Centering	129
FRAP Model Accounting for Immobile Molecules and Bleaching due to Image Capture	129
Future Work	130
Further Investigation on Nuclear Movement.....	130
Microtubule motor kinesin in nuclear rotation.....	130
Actomyosin contraction and nuclear positioning	131
The role of intermediate filament in nuclear movement	132
Nuclear Positioning under the Influence of Extracellular Forces	133
Cell Migration During Wound Healing	133
Effects of Other Motor Forces on Microtubule Mechanics	134
 APPENDIX	
A MATLAB CODE FOR NUCLEAR ROTATION ANALYSIS.....	140
B MATLAB CODE FOR NUCLEAR TRANSLATION ANALYSIS	143
C MATLAB CODE FOR CENTROSOME POSITION ANALYSIS	145
D MODEL FOR MICROTUBULE MECHANICS AND CENTROSOME CENTERING.....	148
Microtubule Mechanics	148
Model for Dynein Forces.....	149
Simulation Methods.	150
Simulations of Microtubule Buckling	152
Simulations of Centrosome Centering	152
Centrosome Relaxation Time	154
E λ for BLEACHING OF FREE PROTEIN IN THE CYTOPLASM	156
F MATLAB CODE FOR FRAP MODELING AND SIMULATION.....	157
Simulation of Bleaching Dynamics in Image Capture Process	157
Comparison of Observed Dynamics and Actual Dynamics	157
Modeling of Normalized Bleaching Dynamics	158
Simulation of FRAP	159
Model Fitting of FRAP.....	159
Define Fitting Function of FRAP Model	159
Fitting Focal Adhesion FRAP Experiment Data to the Model	160
Define Fitting Function for Free Molecule Intensity	161
Fitting Free Molecule Intensity in Focal Adhesion FRAP Experiments.....	161
Simulation of FRAP with Multiple Time Intervals	162

LIST OF REFERENCES 164
BIOGRAPHICAL SKETCH..... 179

LIST OF TABLES

<u>Table</u>		<u>page</u>
2-1	Nuclear Rotation Model Parameters.....	56
4-1	Microtubule Mechanics and Centrosome Centering Model Parameters.....	105

LIST OF FIGURES

<u>Figure</u>	<u>page</u>
1-1 Cartoon of dynein structure and walking on the microtubule.	30
2-1 Nuclear rotation is a biased random walk in NIH 3T3 fibroblasts.....	47
2-2 Dynein inhibition significantly reduces nuclear rotation.	48
2-3 Microtubules drive nuclear rotation.....	49
2-4 The centrosome does not rotate with the nucleus.	49
2-5 Schematic of the nuclear rotation model.	50
2-6 Simulations of nuclear rotation in a circular cell.....	51
2-7 Distance between the centrosome and the nucleus decreased in patterned square NIH 3T3 cells.	53
2-8 The centrosome is underneath the nucleus.....	54
2-9 Nuclear rotation in unpatterned cells is significantly larger than that in patterned cells	54
2-10 Nesprin-1 knock-down affects nuclear rotation.....	55
3-1 Schematic of how collective trajectories of nuclear translation were generated.	66
3-2 Nuclear movement upon local introduction of blebbistatin. 67	
3-3 Micromanipulation reveals that the nucleus is under tension between the leading edge and trailing edge.....	68
3-4 Nuclear movement in motile fibroblasts does not required detachment of the trailing edge.	69
3-5 Directional nuclear translation upon Rac-1 photo-activation.....	70
3-6 Kymograph of photo activation experiments.....	72
3-7 Nuclear retraction due to lamellipodia release.....	73
3-8 Effect of KASH on trailing edge detachment.	74
4-1 A comparison of centrosome centering (simulation) with the autocorrelation function of fluctuations in centrosome position (experiment).	94

4-2	Deploymerization rates of microtubules severed by laser ablation.	95
4-3	Minus end microtubules underneath the nucleus increase in bending after laser severing.	96
4-4	Minus-end microtubules at the cell periphery increase in bending after laser severing.	98
4-5	Change in curvature after severing is not correlated with the initial curvature, nor with the spatial location of the cut.	98
4-6	Inhibition of dynein causes dispersion of the Golgi complex.	99
4-7	Microtubules radiate from the centrosome in dynein inhibited cells.	99
4-8	Simulations predict dynein-induced buckling of microtubules.	100
4-9	Dynein forces are sufficient to center the centrosome.	101
4-10	Microtubules undergo three distinct behaviors upon reaching the periphery	102
4-11	Simulations of centrosome centering.	103
4-12	Minus-end microtubules underneath the nucleus does not traighten after laser severing.	104
5-1	Hypothetical effect of photobleaching due to imaging capture on a whole cell imaging experiment.	122
5-2	Solutions to Equation 5-6 showing how photobleaching during image capture can give the erroneous impression of an 'immobile' fraction.	123
5-3	Solutions to Equation 5-10A and 10B that account for the presence of an actual immobile fraction.	124
5-4	Example of the application of Equation 5-10A and 10B for fitting a GFP-VASP FRAP experiment.	125
5-5	Typical fitting for a GFP-VASP FRAP experiment.	127
5-6	Illustration of typical fitting failed to estimate k_{OFF} in experiments with different time interval τ	127
6-1	Image of intermediate filament in living cells.	137
6-2	Cartoon of a dynein motor indicating how the minus-directed motor bound to the cytomatrix exerts a force towards the microtubule plus end.	138

6-3 Formation of acto-myosin retrograde flow and stress fiber remodeling upon photo activation of Rac-1..... 139

LIST OF ABBREVIATIONS

AAA	ATPase associated with various cellular activities
ATP	Adenosine Triphosphate Nucleotide
BCE	Bovine Capillary Endothelial
CCD	Charge-Coupled Device
DBS	Donor Bovine Serum
DMEM	Dulbecco's Modified Eagle Medium
EGFP	Enhanced Green Fluorescent Protein
FRAP	Fluorescence Recovery After Photobleaching
GTP	Guanosine-5'-triphosphate
IF	Intermediate Filaments
INM	Inner Nuclear Membrane
KASH	Klarsicht ANC-1 Syne Homology
LINC	Linker of Nucleoskeleton to Cytoskeleton
LOV	Light-Oxygen-Voltage
MT	Microtubule
MTOC	Microtubule Organizing Center
NA	Numerical Aperture
ONM	Outer Nuclear Membrane
PCM	PeriCentriolar Material
PDMS	Polydimethylsiloxane
Rac1	Ras-related C3 botulinum toxin substrate 1
Rho	Ras homolog gene family
SF	Stress Fiber
SUN	Sad1p, UNC-84

TAN	Transmembrane Actin-associated Nuclear
VASP	Vasodilator-Stimulated Phosphoprotein
YFP	Yellow Fluorescent Protein

Abstract of Dissertation Presented to the Graduate School
of the University of Florida in Partial Fulfillment of the
Requirements for the Degree of Doctor of Philosophy

MOTOR FORCES AND NUCLEAR POSITIONING IN LIVING CELLS

By

Jun Wu

May 2012

Chair: Tanmay Lele
Cochair: Richard Dickinson
Major: Chemical Engineering

The nucleus is the largest and heaviest organelle in a cell and its proper positioning is crucial for basic cell functions, such as cell migration, division, fertilization and establishment of polarity. Irregularities in nuclear movement (or nuclear positioning) are associated with various serious diseases.

Nuclear movement in the cell is a complex process that involves interactions with all three cytoskeletal systems - actin, intermediate filaments and microtubules. The interactions occur through nuclear-embedded molecular tethers that link to the cytoskeleton. The molecular linkage between the nucleus and the cytoskeleton can be also established through molecular motors, proteins that convert chemical energy to mechanical forces. How molecular motors drive nuclear movement remains poorly understood.

Nuclear rotation and nuclear translation are the two types of nuclear motions commonly observed in the cell. We investigated the physical mechanism for nuclear rotation in the cell. We found that the nuclear rotation angle is directionally persistent on a time scale of tens of minutes, but rotationally diffusive on longer time scales, and rotation required the activity of the microtubule motor dynein. Based on these results, a

mechanical model for torque generation on the nucleus was proposed. To investigate nuclear translation, we designed experiments utilizing two different techniques- protein photo activation and cell micromanipulation. The results from these experiments point to a tug of war between forward pulling and rearward pulling forces on the nuclear surface generated by actomyosin contraction. Net nuclear motion occurs when the forward pulling force increases during lamellipodial formation.

We also investigated the mechanisms of positioning of the centrosome, which is in physical proximity with the nucleus. The positioning of centrosome is very important in cell migration and cell division. Whether the centrosome is positioned by pulling forces or pushing forces originating in dynamic microtubules remains a controversy. By severing a single microtubule with femtosecond laser ablation, we found that microtubules are under tension generated by dynein. We also show that dynein-mediated pulling forces are sufficient to center the centrosome.

CHAPTER 1 INTRODUCTION

Nuclear Positioning is an Important Cell Function

Cell and developmental processes like fertilization, cell migration and division, and establishment of polarity require specific positioning of the nucleus within the cell(1-5). Recent studies suggested that nuclear migration is a critical process for neuronal development, including interkinetic nuclear migration and nuclear translocation during retinogenesis(6). During mitosis in *S. cerevisiae*, the nucleus needs to be moved into the bud neck for proper cell division(7).

Defects in the nuclear force-generating system are related to disorders of the nervous system(8) and the musculo-skeletal system(1), such as cardiac and skeletal myopathies, partial lipodystrophy, peripheral neuropathy(9). Recently, it has also been linked to premature aging diseases like Hutchison Gilford progeria syndrome (HGPS), atypical Werner's syndrome and mandibulocaral dysplasia (MAD)(10).

Despite the importance of nuclear positioning as a critical cellular function and its relevance to disease, our understanding of how forces are generated on the nuclear surface in living cells is surprisingly limited. At the molecular level, nuclear movement in the cell is a complex process that involves interactions with all three cytoskeletal systems - actin, intermediate filaments and microtubules(2). On the cytoplasmic side, these interactions are mediated by molecular tethers such as nesprin family proteins that link the nuclear surface to the actin and intermediate filament cytoskeleton(11) and molecular motors such as nuclear-bound dynein(12-14).

The force transfer between the nucleus and the cytoskeleton are mediated by the LINC (linker of nucleoskeleton to cytoskeleton)(15, 16) complex which includes two

families of proteins containing KASH (Klarsicht ANC-1 Syne Homology) domains and SUN (Sad1p, UNC-84) domains(17-20). Large nesprin isoforms (members of KASH proteins) located on the outer nuclear membrane can bind to cytoskeletal structures with their amino-terminal cytoplasmic domain. At the same time, these nesprins can interact with SUN proteins on the inner nuclear membrane via their carboxyl-terminal perinuclear domain. SUN proteins in turn bind to lamins in the nuclear lamina, chromatin, and other, yet unknown nuclear envelope proteins, thus completing the link from the cytoskeleton to the nucleus(15, 21-23). Recently, it has been shown that nesprin-1G is involved in recruiting nuclei to, or anchoring nuclei at, the neuromuscular junction(3). Other studies suggest that the mispositioning of the nucleus may be caused by mutations or deficiency of nuclear lamina proteins and related proteins, such as lamin A/C(24, 25)

Molecular motors are biological molecular machines that are the essential agents of movement in living organisms. These motors harness the chemical free energy released by the hydrolysis of ATP in order to perform mechanical work. For example, the motor protein myosin is responsible for muscle contraction(26), and microtubule motors dynein and kinesin are responsible for intracellular transportation(27-30). Dynein has been shown to pull the nuclear surface in NIH 3T3 fibroblasts and cause nuclear rotation(12) and nuclear translation in other cell types(22, 31, 32). Similarly, kinesin-1 also mediates cell polarization(31) and involves in microtubule dependent nuclear migration in *C. elegans* along with dynein(14, 16, 33).

Dynein-Based Torque Generation on the Nucleus

Cytoplasmic dynein was isolated from both *C. elegans* and calf brain white matter in 1987 by Lye et al.(34) and Paschal et al.(35, 36). Dynein is a large protein complex

(1.2 MDa) composed of two identical heavy chains and several associated chains(37). The heavy chain contains six AAA domains arranged in a ring and has the motor machinery that is responsible for transducing chemical energy into directed mechanical force applied to the microtubule surface. The intermediate- and light-chains help specify the intracellular location of the dynein and regulate its motor activity(38). Its MT-binding domain (MTBD) is located at the end of a 15 nm long coiled-coil stalk that emerges from the AAA domains(39). Dynein walks on microtubule toward the minus end (centrosome) in a hand-over-hand-like fashion ((40) and Figure 1-1).

There are some studies which explored how dynein connects to the nucleus. Mosley-Bishop *et al.*(41) have shown that microtubule-based movement of nuclei during eye development in *Drosophila* requires Klarsicht, a prototype KASH domain protein that binds cytoplasmic dynein. Klarsicht is tethered in the ONM via a transluminal interaction with Klaroid in the INM to form a KASH/SUN protein pair, and then Klaroid binds to the lamin(42). Another dynein-binding KASH domain protein, Zyg-12, has also been identified in *C. elegans*(43). It is believed to be related to the mammalian Hook protein family. Nuclear anchoring has been shown to be mediated by the engagement of Zyg-12-associated dynein with noncentrosomal microtubules that were nucleated at the plasma membrane(13).

Nuclear rotation has been observed in many cell types(12, 44-47). One study suggested that the rotation may be due to a transient bond between the centrosome and the nuclear membrane mediated by dynein and Hook/SUN family proteins, such that the nuclear rotation is coupled with the movement of the centrosome itself(48). Levy and Holzbaur(12) showed that the migration of fibroblasts into a newly created

wound triggered nuclear translocation and coupled rotation, and both were decreased in dynein-null fibroblasts; interestingly these authors suggested that the centrosome is not bound to the nucleus. In non-wounded cells, another interesting feature of nuclear rotation is that the rotation angle fluctuates(49), and rotation can occur over several hours of observation(46). The cause of fluctuations and long-time persistence in the rotation angle is currently unknown.

A physical explanation for how torque could arise through interactions between nuclear bound dynein and microtubules emanating from a stationary centrosome to create fluctuating, persistent nuclear rotation is needed. In Chapter 2, we show that in NIH 3T3 fibroblasts, nuclear rotation is a persistent random walk that requires dynein. The centrosome does not rotate with the nucleus. We formulated a model based on microtubules undergoing dynamic instability, with tensional forces between a stationary centrosome and the nuclear surface mediated by dynein. The model predicts that the fluctuations and persistence in nuclear rotation are due to the dynamic instability of microtubules. A key model prediction is that the rotation should decrease with decreasing distance between the nucleus and the centrosome. We experimentally tested this prediction by showing that rotation in patterned cells (where the centrosome overlaps with the nucleus and is close to the nuclear centroid) is considerably reduced compared to unpatterned, stationary cells with larger nuclear-centrosomal distance. Together, these results show that force generation by dynein on microtubules undergoing dynamic instability is sufficient to explain the key features of nuclear rotation.

Actomyosin Forces on the Nucleus

As mentioned before, the cell accomplishes nuclear motion by transferring active cytoskeletal forces onto the nuclear surface through molecular connections between the nuclear lamina and the cytoskeleton established by LINC complex proteins(15, 16). One of the main source of the active forces are non-muscle myosin II (NMMII) based contraction of F-actin filaments(50, 51). Myosin refers to a family of F-actin associated motors. It was first isolated as a complex with actin filaments by Kuhne and coworker (1864)(52), though it was not until the 1940s that the complex was dissociated into the separate proteins, myosin and actin (Straub, 1941-1942: Szent-Gyorgyi, 1941-1942)(52). The protein complex composed of actin and myosin is referred to as "actomyosin". The discovery of the myosin crossbridge by H.E. Huxley in 1957 provided a molecular basis for the contraction of muscle: the bending or rotation of these crossbridges causes the actin-containing thin filaments to slide relative to the myosin-containing thick filaments, and the sliding of these filaments, in turn, leads to the shortening of the muscle(26, 53-55).

There are contrasting views on how the force generated by actomyosin contraction acts on the nucleus. For actomyosin-based nuclear force generation, much of the research has focused on initial polarization mechanisms in a wounded NIH 3T3 fibroblasts monolayer where the nucleus is observed to move away from the leading edge while the centrosome stays in the same position within the first few hours after wounding(5, 56, 57). The polarization was abolished when myosin II activity was inhibited by blebbistatin treatment. Myosin activity was also found to be regulated by Cdc42 in these wounded cells. When dynein was inhibited, the centrosome moved with the nucleus, resulting in failure of polarization. Based on these experimental results,

Gunderson and coworkers proposed that the actomyosin retrograde flow pushes the nucleus possibly through specific linkages between the nucleus and actin filaments such as Syne/ANC-1(5). Recently, Gundersen and co-workers have shown that the rearward nuclear movement in wounded cells is inhibited upon overexpression of KASH domains(57). Depletion of nesprin2G with small interference RNA (siRNA) also blocked rearward nuclear movement and could be rescued by expression of mini-nesprin2G, which confirmed that nuclear movement required nesprin2G(57). Nuclear envelope proteins SUN2, mini-nesprin2G and nesprin2G all colocalized with dorsal actin cables to form linear arrays referred as TAN (transmembrane actin-associated nuclear) lines, which transmit force from retrograde actin flow to the nucleus(57). Furthermore, defects in the TAN line structure due to protein mutations may be associated with striated muscle disease(56). In addition, there is evidence for a squeezing (pushing) force due to actomyosin contraction in the trailing edge(58) which may move the nucleus toward the leading edge.

Other studies have suggested that the nucleus is normally under a state of tension(50, 59-62). Thus the basic question of whether the nucleus is primarily “pushed” into position by compressive cytoskeletal forces (due to retrograde actomyosin flow or pushing forces from the trailing edge), or “pulled” by tensile actomyosin forces, still remains controversial. Both pushing and pulling forces may simultaneously operate on the nucleus, but of interest in this thesis is the net direction of the force balance (i.e. pushing versus pulling) and the dominant cytoskeleton origin of these forces in a single crawling NIH 3T3 fibroblast.

In Chapter 3, we discuss two approaches to perturb the force balance on the nucleus. First, we inhibited myosin activity in the trailing edge locally. The nucleus moved toward the leading edge in a LINC complex dependent fashion. We next detached the trailing edge of motile fibroblasts and recorded nuclear motion and deformation in response to detachment as well as subsequent pulling of the trailing edge. We found that the nucleus underwent elastic deformations on manipulation of the trailing edge in a myosin dependent and LINC complex dependent fashion. Collectively, these experiments suggest the presence of pulling forces on the nucleus from the trailing edge. We next used the Rac1 photoactivation assay to trigger the formation of new lamellipodia(63); the nucleus was observed to move in the direction of newly formed lamellipodia in a myosin and LINC complex dependent but microtubule independent manner. Collectively, our results suggest that the nucleus is pulled on both sides, resulting in a tug-of-war between actomyosin forces. Consistent with this picture, trailing edge detachment is significantly reduced on disruption of nuclear-cytoskeletal linkages, suggesting that the nucleus acts as an integrator of tensile actomyosin forces in a motile cell.

Dynein Force Generation on Microtubules

The centrosome is an organelle that serves as the main microtubule organizing center (MTOC), where microtubules are produced. In animal cells, centrosomes are composed of two perpendicular arranged centrioles surrounded by an amorphous mass of protein termed the pericentriolar material (PCM)(64). During mitosis, these two centrioles duplicate to form two new centrosomes. The two new centrosomes then move to opposite ends of the nucleus and form spindles to separate chromosome into the two daughter cells(65, 66). During interphase, the centrosome normally stays at the

center of a cell and close to the nucleus. The position of the centrosome is very important in that microtubules originating from the centrosome are responsible for the intracellular transportation of different organelles(67). Therefore, if the centrosome is mislocated, it can disrupt intracellular traffic.

Centrosome positioning involves force generation by microtubules, so do many essential eukaryotic cell functions, including migration and mitosis(68-70). Microtubules have a large bending stiffness, with a thermal persistence length of the order of several millimeters. Yet they are nearly always bent or buckled in cells, implying that they are being subjected to substantial lateral forces along their lengths(71, 72) or compressive forces at their tips(73). Compressive forces have been proposed as the means by which the centrosome and spindle bodies are centered(74-76). In this mechanism, microtubules spanning the shorter distance between the centrosome and the cell boundary exert a larger force because the critical buckling force is a strong function of length ($\propto L^{-2}$). Consistent with this view, *in vitro* experiments(77) showed that microtubule organizing centers could be centered by elongating microtubules pushing on the boundaries of a microfabricated chamber. On the other hand, there is increasing evidence that molecular motors play a key role in microtubule-based force generation. Tensile forces generated by cytoplasmic dynein, a molecular motor that walks towards microtubule minus ends while bound to the cortex, have been proposed as the driver for centrosome centering(78-80). A similar dynein-driven mechanism has been proposed for spindle body positioning in yeast cells(81). Dynein has also been implicated in the buckling of microtubules by pushing segments towards the plus end(82).

The apparently contradictory results of previous studies leave basic questions regarding *in vivo* microtubule mechanics unresolved. What is the contribution of dynein to the force balance on individual microtubules? Do microtubules exert tensile or compressive forces on the centrosome? How does a radial array of microtubules cause centrosome centering? In Chapter 4, we discuss our investigation on dynein force generation on microtubules. We first performed experiments in which individual microtubules in BCE cells were severed by laser ablation. The goal was to remove a key element in the overall force balance, which is thought to be a combination of elastic forces from microtubule bending and elastic deformation of the surrounding cytomatrix (73, 83). Surprisingly, our experiments showed that microtubules do not straighten after severing, suggesting a large frictional resistance to lateral motion. Instead, segments near a newly created minus end usually increase in curvature following severing, as if the end of the segment was under a compressive load. By contrast, in dynein-inhibited cells microtubule segments near the cut always straightened and did so much more rapidly than in normal cells. To explain these observations we propose a model for dynein force generation that accounts for stochastic binding and unbinding of dynein motors from the microtubules. An ensemble of these motors develops a steady force in the direction of the tangent to the microtubule and a *frictional* resistance transverse to the microtubule. Numerical simulations of individual microtubules show that the model can explain the concentration of microtubule buckles near the cell periphery (73). Simulations of centrosome centering by a radial array of microtubules are consistent with tensile forces on the centrosome; in the absence of motor forces the centrosome

remains off center, which is consistent with observations in dynein-inhibited cells (5, 78, 80, 84).

Fluorescence Recovery after Photobleaching (FRAP)

Fluorescence recovery after photobleaching (FRAP) is an optical technique to study intracellular protein dynamics and binding kinetics in living cells(85-92). FRAP experiments involve bleaching of fluorescently labeled proteins in a pre-chosen location inside the cell with a high intensity laser pulse. When proteins are transiently bound to structures in the photobleached spot, the fluorescence recovers owing to exchange between fluorescently labeled diffusing molecules in the cytoplasm or membrane with the bound photobleached molecules in the bleached spot. The recovery curve can be fit to models to estimate transport and binding parameters. The accurate modeling of FRAP experiments, issues with parameter estimation and validation of estimated parameters are active areas of interest(87, 93-101).

The approach to fit FRAP experiments to mathematical models involves a suitable normalization of the experimental data(102). For example, if $F(t)$ is the fluorescence in a spot in the cytoplasm, and bleaching occurs at $t = 0$, then one way to normalize the signal is $N(t) = \frac{F(t) - F(0)}{F(t < 0) - F(0)}$. Here, the denominator represents the amount of fluorescence that *should* be theoretically recovered after photobleaching assuming one waits long enough in the experiment (i.e. $F(\infty) = F(t < 0)$), while the numerator represents fluorescence that has recovered at any time. The assumption can be made in most cases that the bleaching pulse at $t = 0$ itself does not alter the total fluorescence significantly. If the experiment is then stopped at time θ (when the

fluorescence appears to visually plateau), in many cases it is found that $N(\theta) < 1$ i.e. complete fluorescence recovery does not occur. If $N(\theta) < 1$, the usual procedure is to calculate the so-called immobile fraction $\beta = 1 - N(\theta)$; the hypothesis is that there is a sub-population of fluorescent molecules in the bleached spot that do not recover to any measurable extent over the time θ . While this approach is widely followed in the literature and may be applicable for many situations, it is obvious that if there was significant bleaching as a result of the image capture process itself, then $F(\theta) < F(t < 0)$ even though there is no real immobile fraction.

Of all the different experimental complications that make FRAP analysis difficult, the undesirable decay of the fluorescence due to the image capture process itself has received little attention. Typically, the decay is 'corrected' by dividing the observed signal by the overall signal in the cell. This procedure can potentially invalidate the fitting of mathematical models to FRAP data owing to the arbitrary correction of experimental data with another time-varying curve. If the effect of bleaching during image capture is significant and no correction to the data is applied, then this can invalidate the fitting because the mathematical models do not include the effect of photobleaching during image capture. Either way, neglecting the effect of photobleaching during image capture has the potential to render serious errors in the estimation of kinetic or transport parameters from the FRAP experiment. In Chapter 5, we take the view that mathematical models for FRAP analysis should *explicitly* account for the effects of bleaching during image capture instead of relying on corrections to data, or on the perfect experiment that does not suffer from the effects of photobleaching. We develop models that should be generally applicable and provide an experimental demonstration

on how to use the models. The analysis discussed here can help bring greater clarity into the interpretation of FRAP experiments.

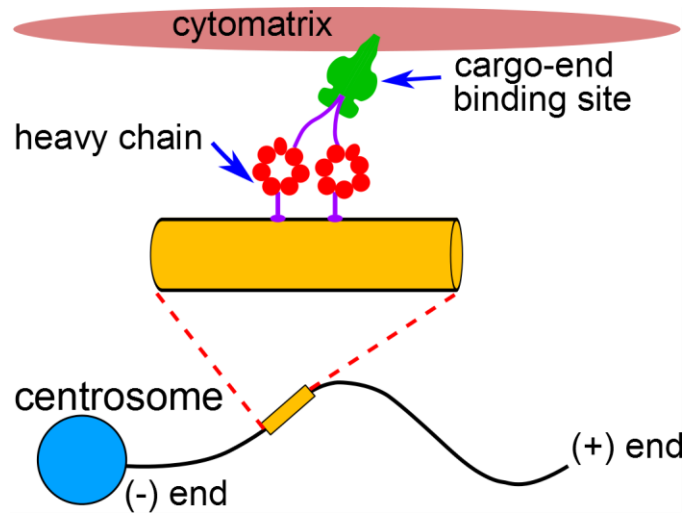


Figure 1-1. Cartoon of dynein structure and walking on the microtubule. Dynein has two heavy chains which contain six AAA domains arranged in a ring (red circles). The two coiled-coil stalks emerging from the AAA ring contain MT-binding domain. The cargo-end binding site bind to dynactin to form a complex which could bind to cargo or cytomatrix. Individual dynein molecules walk towards the microtubule minus end (centrosome).

CHAPTER 2 DYNEIN MOTOR FORCES ON THE NUCLEUS

In living cells, a fluctuating torque is exerted on the nuclear surface but the origin of the torque is unclear. We found that the nuclear rotation angle is directionally persistent on a time scale of tens of minutes, but rotationally diffusive on longer time scales. Rotation required the activity of the microtubule motor dynein. We formulated a model based on microtubules undergoing dynamic instability, with tensional forces between a stationary centrosome and the nuclear surface mediated by dynein. Model simulations suggest that the persistence in rotation angle is due to the transient asymmetric configuration of microtubules exerting a net torque in one direction until the configuration is again randomized by dynamic instability. The model predicts that the rotational magnitude must depend on the distance between the nucleus and the centrosome. To test this prediction, rotation was quantified in patterned cells in which the cell's centrosome was close to the projected nuclear centroid. Consistent with the prediction, the angular displacement was found to decrease in these cells relative to unpatterned cells. This work provides the first mechanistic explanation for how nuclear dynein interactions with discrete microtubules emanating from a stationary centrosome cause rotational torque on the nucleus.

Materials and Methods

Cell Culture, Plasmids and Transfection

NIH 3T3 fibroblasts were cultured in DMEM (Mediatech, Manassas, VA) with 10% donor bovine serum (Gibco, Grand Island, NY) and 1% Penn-Strep (Mediatech). For

This chapter is reproduced from a paper previously published in *Journal of Cellular Physiology* with permission from John Wiley & Sons. Modeling and simulations are attributed to Dr. Richard B. Dickinson in the Department of Chemical Engineering, University of Florida.

microscopy, cells were cultured on glass-bottomed dishes (MatTek Corp, Ashland, TX) coated with 5µg/ml fibronectin at 4°C overnight.

DsRed-CC1 plasmid was kindly provided by Prof. Trina A. Schroer from Johns Hopkins University, pDsRed plasmid was kindly provided by Prof. Scott S. Grieshaber from the University of Florida. YFP-γ-tubulin was prepared from the MBA-91 AfCS Set of Subcellular Localization Markers (ATCC, Manassas, VA). Transient transfection of plasmids into NIH 3T3 fibroblasts was performed with Effectene[®] Transfection Reagent (Qiagen, Valencia, VA).

Time-Lapse Imaging and Analysis

Time-lapse imaging was performed on a Nikon TE2000 inverted fluorescent microscope with a 60X/1.49NA objective and CCD camera (CoolSNAP, HQ², Photometrics, Tucson, AZ). During microscopy, cells were maintained at 37 °C in a temperature, CO₂ and humidity controlled environmental chamber. Images were imported into MATLAB (Mathwork, Natick, MA) and two nucleoli in the nucleus were tracked with time to calculate the rotation angle. The positions of the nucleoli (\vec{r}_{1j} and \vec{r}_{2j}) at time point j were calculated to sub-pixel resolution using previously published image correlation methods(103), and the angle between lines joining nucleoli in successive images was calculated as $\cos(\Delta\theta_j) = \frac{(\vec{r}_{1j} - \vec{r}_{2j}) \cdot (\vec{r}_{1j+1} - \vec{r}_{2j+1})}{|\vec{r}_{1j} - \vec{r}_{2j}| |\vec{r}_{1j+1} - \vec{r}_{2j+1}|}$ where

$$\cos(\Delta\theta_j) = \frac{(\vec{r}_{1j} - \vec{r}_{2j}) \cdot (\vec{r}_{1j+1} - \vec{r}_{2j+1})}{|\vec{r}_{1j} - \vec{r}_{2j}| |\vec{r}_{1j+1} - \vec{r}_{2j+1}|} \text{ where}$$

$\Delta\theta_j = \theta_{j+1} - \theta_j$ is the angular displacement between time point j and $j+1$. The

autocorrelation function was calculated as $G_i = \frac{\sum_{j=1}^{N-i} (\Delta\theta_j)(\Delta\theta_{j+i})}{N-i}$. The mean-squared

angular displacement was calculated as $MSD_j = \frac{\sum_{j=1}^{N-i} (\theta_{j+i} - \theta_j)^2}{N-i}$.

Immunofluorescence

Immunostaining studies were carried out as previously described(104) with mouse monoclonal anti-human γ -tubulin (Sigma-Aldrich, St. Louis, MO) and polyclonal rabbit anti-human α -tubulin (Abcam, Cambridge, MA) antibodies, and Hoechst 33342 in 4% paraformaldehyde fixed cells permeabilized with 0.1% Triton X-100 in PBS. Goat anti-mouse and goat anti-rabbit antibodies conjugated with Alexa Fluor 488 and Alexa Fluor 594 fluorescent dyes (Invitrogen, Carlsbad, CA) were used as secondary antibodies.

Cell Shape Patterning

Cell shape patterning was done by using the micro-contact printing technique described in (105). Molds for the stamps were produced with the UV lithography technique by illuminating a positive photoresist through a chrome photomask on which micropatterns were designed (Photo Sciences, Inc., Torrance, CA). PDMS (Sylgard 184 kit, Dow Corning, Midland, MI) was cast on the resist mold using a 10:1 ratio (w/w) of elastomer to hardener and cured at 60°C for 2 hr and postcured at 100°C for 1hr. For micropatterning, the PDMS stamp was treated with 50 μ g/ml human fibronectin solution (BD Biocoat™, Franklin Lakes, NJ). The stamp was then dried and placed onto the substrate onto which the cells were plated. Ibidi dishes (Ibidi, Verona, WI) were chosen as the substrate. After 5 min, the stamp was removed and the remaining area was blocked with PLL-g-Poly-ethylene glycol (SuSoS AG, Dübendorf, Switzerland),

preventing protein adsorption and cell attachment. After treatment the surface was washed and cells were plated.

Results

Nuclear Rotation is a Persistent Random Walk

Nuclear rotation has been typically studied by time-lapse microscopy; however, a quantitative analysis of fluctuating nuclear rotation has not been previously reported. We measured nuclear rotation angle with high accuracy using image correlation methods. The nucleus (and its contents) is known to rotate as a solid object(106), therefore tracking fiduciary markers on the nucleus (nucleoli) allowed us to calculate the angular displacement between successive images. By tracking the non-moving nucleus in cells fixed with paraformaldehyde which cross-links the cellular contents and ensures zero rotation, we calculated the error in the image correlation as being less than 1%. As shown by the trajectories in Figure 2-1, the net angle through which the nucleus rotates exhibited short-time fluctuations and typically long-time persistence in the direction of rotation. Most trajectories displayed a significant angle of rotation in around two hours, while some fluctuated in position without achieving much net displacement.

To quantitatively characterize the angular trajectories, the average mean-squared angular displacement (MSD) was estimated (see methods for how MSD was calculated) from data pooled from several cells (Figure 2-1C). The MSD showed characteristics of a persistent random walk, with a parabolic shape at short time approaching linearity at long time (Figure 2-1C). To further characterize the directional persistence, we estimated the autocorrelation function of angular displacements (Figure 2-1C inset). This autocorrelation function resembled a double exponential, reflecting the relaxation

of short-time fluctuations in directional rotation and longer-time relaxation of persistent directional rotation.

Cytoplasmic Dynein is Required for Nuclear Rotation in Stationary Fibroblasts

To determine the role of dynein in nuclear rotation in stationary fibroblasts, we transfected cells with DsRed-CC1, which inhibits dynein by competitive binding(107, 108). pDsRed plasmid transfected cells were used as the control. Transfection with DsRed-CC1 significantly decreased nuclear rotation compared with cells expressed the control pDsRed plasmid (Figure 2-2). We also found that rotation was abolished upon depolymerizing microtubules (Figure 2-3). Also, the centrosome was observed not to rotate with the nucleus, but rather occupied a relatively fixed position in space even as the nucleus rotated through a significant angle (Figure 2-4). These results are consistent with recent observations by Levy et al(12) in wounded fibroblasts, and Gerashchenko et al(49) in non-wounded murine cells.

Model Formulation

We developed a mechanistic model for dynein forces on the nucleus. The purpose of this model is to demonstrate that retrograde MT-associated motors pulling on the nucleus are sufficient to explain nuclear rotation with observed statistical characteristics. Individual dynein molecules on MT's within a range σ of the nucleus are assumed to transiently bind and pull the nucleus toward the microtubule (-)-ends (Figure 2-5). As is typically assumed for molecular motors, the motor speed v_m depends on the pulling force \mathbf{f} (a vector) that the dynein molecule exerts on the nucleus. For simplicity, the force-speed relation for dynein motors is assumed approximately linear(109), similar to other recent studies on dynein-mediated nuclear translation(81)

$$v_m/v_{\max} = 1 + \mathbf{n} \cdot \mathbf{f} / f_{\max} \quad (2-1)$$

where \mathbf{n} is a unit vector directed toward the (+)-end of the MT. Here, v_{\max} represents the speed at zero load and f_{\max} represents the stall force required of the motor, such that the motor stalls when the component of the pulling force in the (-)-end direction is equal to f_{\max} .

MT-nucleus linkages are assumed to have a finite lifetime, such that the force accumulated by translation of the nuclear surface at velocity \mathbf{v} relative to the MT (assumed stationary), or by the motor walking along the MT, is relieved upon dissociation of the linkage. The accumulation of the force depends on the stiffness of the linkage, and it is simplest to assume that the linkages behave as linear springs with stiffness κ . Thus, accounting for the changing load, the force on the nuclear surface changes with time t , as

$$d\mathbf{f} / dt = -\kappa(\mathbf{v} + v_m\mathbf{n}) \quad (2-2)$$

Upon substitution of Equation 2-1 for v_m and integration, this become

$$\mathbf{f}(t) = -f_{\max} \left(1 + \frac{\mathbf{n} \cdot \mathbf{v}}{v_{\max}} \right) \left\{ 1 - \exp \left[-\frac{\kappa v_{\max}}{f_{\max}} t \right] \right\} \mathbf{n} - \kappa(\mathbf{v} - (\mathbf{n} \cdot \mathbf{v})\mathbf{n})t \quad (2-3)$$

Linkages are assumed to dissociate with a first-order rate constant k_{off} (s^{-1}) such that the probability of a linkage existing at time t is $P_b(t) = e^{-k_{\text{off}}t}$. The mean force over the bond lifetime η is thus

$$\langle \mathbf{f} \rangle = -\int_0^{\infty} \mathbf{f}(\eta) dP_b(\eta) = -f_0 \left(1 + \frac{\mathbf{n} \cdot \mathbf{v}}{v_{\max}} \right) \mathbf{n} - \frac{\kappa}{k_{\text{off}}} (\mathbf{I} - \mathbf{nn})\mathbf{v} \quad (2-4)$$

where $f_0 \equiv \frac{f_{\max}}{\frac{f_{\max} k_{off}}{\kappa v_{\max}} + 1}$ is the average force per dynein molecule on a stationary nucleus.

For dynein density (number/length) ρ , the net mean force per unit length, \mathbf{K} , is then

$$\mathbf{K} = -F_0 \left(1 + \frac{\mathbf{n} \cdot \mathbf{v}}{v_{\max}} \right) \mathbf{n} - \gamma (\mathbf{I} - \mathbf{nn}) \mathbf{v} \quad (2-5)$$

where $F_0 \equiv \rho f_0$ is the mean longitudinal force/MT length for a stationary nucleus, and

$\gamma \equiv \rho \kappa / k_{off}$ is the friction coefficient ((force/speed)/MT length) to lateral motion.

Mechanics and kinematics of the nucleus. The net force and torque exerted on the nucleus by an MT depends on the length span of the MT that is close enough to interact with the nucleus. Let \mathbf{n}_s be the position vector on the MT parameterized by contour length s , between the centrosome position ($s=0$) and the (+)-end ($s = s_{end}$). Further, let s_1 and s_2 represent the beginning and end of the interaction range with the nucleus in which the distance between the MT and nuclear surface is within σ . Based on the geometry of a line passing near a sphere, MT will interact with the nucleus provided $(R + \sigma)^2 > (\mathbf{r}_0^2 - (\mathbf{n} \cdot \mathbf{r}_0)^2)$ where \mathbf{r}_0 is the center of rotation of the nucleus. The endpoints of the interacting span of the MT are then

$$s_1 = \max \left\{ 0, \mathbf{n} \cdot \mathbf{r}_0 - \sqrt{(R + \sigma)^2 - (\mathbf{r}_0^2 - (\mathbf{n} \cdot \mathbf{r}_0)^2)} \right\} \quad (2-6)$$

$$s_2 = \min \left\{ s_{end}, \mathbf{n} \cdot \mathbf{r}_0 + \sqrt{(R + \sigma)^2 - (\mathbf{r}_0^2 - (\mathbf{n} \cdot \mathbf{r}_0)^2)} \right\} \quad (2-7)$$

where s_{end} is the contour position of the (+)-end. The net MT force and torque are thus

$$\mathbf{F} = \int_{s_1}^{s_2} \mathbf{K} ds = -\rho \int_{s_1}^{s_2} \left\{ f_0 \left(1 - \frac{\kappa}{k_{off} f_{\max}} \mathbf{n} \cdot \mathbf{v}(s) \right) \mathbf{n} - \frac{\kappa}{k_{off}} \mathbf{v}(s) \right\} ds \quad (2-8)$$

$$\boldsymbol{\tau} = \int_{s_1}^{s_2} (\mathbf{n}\mathbf{s} - \mathbf{r}_0) \times \mathbf{K} ds = -\rho \int_{s_1}^{s_2} \left\{ f_0 \left(1 - \frac{\kappa}{k_{off} f_{max}} \mathbf{n} \cdot \mathbf{v}(s) \right) (\mathbf{n} \times \mathbf{r}_0) - \frac{\kappa}{k_{off}} (\mathbf{n}\mathbf{s} - \mathbf{r}_0) \times \mathbf{v}(s) \right\} ds \quad (2-9)$$

where the local velocity \mathbf{v} generally depends on translation and rotation as

$$\mathbf{v}(s) = \mathbf{V}_{nuc} + \boldsymbol{\omega}_{nuc} \times (\mathbf{n}\mathbf{s} - \mathbf{r}_0) \quad (2-10)$$

Neglecting other cytoskeletal (frictional) contributions to force and torque on the nucleus and neglecting inertia, the net force and torque balances are

$$\sum_i \mathbf{F}_i = 0 \quad (2-10)$$

$$\sum_i \boldsymbol{\tau}_i = 0 \quad (2-11)$$

which yield six equations for the six unknown components of vectors \mathbf{v} and $\boldsymbol{\omega}$.

The model can be simplified substantially by neglecting translation (assuming that the distance between the centrosome and the nucleus does not change during rotation; see Figure 2-4) and allowing rotation only about the vertical z-axis, consistent with experimental observations. A possible explanation for rotation about only the z-axis is that the nucleus is compressed into an oblate spheroid by cell spreading(104, 110), thus rotation in other directions is resisted as it requires substantially more deformation of the cytoskeleton. Hence, rather than six degrees of freedom, we need only consider the component of the rotational velocity normal to the image plane ($\omega_{nuc,z}$) determined by

solving $\sum_i \tau_{z,i} = 0$ such that

$$\omega_z = \frac{-\frac{f_0 k_{off}}{\kappa} \sum_i \rho_i (r_{0,x} n_{y,i} - r_{0,y} n_{x,i}) (s_{2,i} - s_{1,i})}{\sum_i \rho_i \left\{ \frac{f_0}{f_{max}} (r_{0,x} n_{y,i} - r_{0,y} n_{x,i}) (s_{2,i} - s_{1,i}) + \frac{1}{3} (n_{x,i}^2 + n_{y,i}^2) (s_{2,i}^3 - s_{1,i}^3) - (n_{x,i} r_{0,x} + n_{y,i} r_{0,y}) (s_{2,i}^2 - s_{1,i}^2) + (r_{0,x}^2 + r_{0,y}^2) (s_{2,i} - s_{1,i}) \right\}} \quad (2-12)$$

Lastly, although dynein may uniformly coat the nuclear surface, we speculate that linkages are most readily formed when MT's run parallel to the nuclear surface and are inhibited when MTs impinge normal to the surface. To account for this, we assume that the effective local linkage density $\rho_i = \rho \sin \phi_i$ varies with angle of incidence ϕ_i of the MT with the surface as $\rho_i = \rho \sin \phi_i$. Upon canceling ρ from numerator and denominator, Equation 2-12 becomes

$$\omega_z = \frac{-\frac{f_0 k_{off}}{\kappa} \sum_i \sin \phi_i (r_{0,x} n_{y,i} - r_{0,y} n_{x,i})(s_{2,i} - s_{1,i})}{\sum_i \sin \phi_i \left\{ \frac{f_0}{f_{max}} (r_{0,x} n_{y,i} - r_{0,y} n_{x,i})(s_{2,i} - s_{1,i}) + \frac{1}{2} (n_{x,i}^2 + n_{y,i}^2)(s_{2,i}^3 - s_{1,i}^3) - (n_{x,i} r_{0,x} + n_{y,i} r_{0,y})(s_{2,i}^2 - s_{1,i}^2) + (r_{0,x}^2 + r_{0,y}^2)(s_{2,i} - s_{1,i}) \right\}} \quad (2-13)$$

Simulations of dynamic instability and nuclear rotation. The rotational velocity obtained from Equation 2-13 depends on the current configuration of microtubules. In the simulations, MTs are assumed to elongate at constant speed V_{pol} from the centrosome until catastrophe occurs. When catastrophe occurs, MTs begin to shrink at a constant speed V_{depol} until recovery. On recovery, they begin to grow again. Catastrophe and recovery have constant probabilities per unit time k_{cat} and k_{rec} respectively. The parameters are shown in Table 2-1. If an MT shrinks completely to the centrosome, a new MT immediately nucleates in another random direction on the unit sphere thereby maintaining a constant number N of MT's. Any MT which impinges on the cell or nuclear boundaries is assumed to stop growing and remain a constant length until catastrophe. MT's are assumed straight and rigid in this treatment. Although actual MT's are not straight in vivo, MT's typically do not change much in direction over the distance from the centrosome to the nucleus; therefore treating them as straight is a reasonable simplification. Another complication is that some MT's may wrap-trace along

the nuclear surface, thereby increasing the effective interaction length of the MT. However, increasing the span of interaction is similar to changing the dynein density, which has no effect on the predicted long-time dynamics. This is because changing the interaction span changes both the pulling force and opposing friction force by equal proportions (see Equation 2-13 which shows that the rotational velocity does not depend on ρ , the density of dynein).

Model Results

We hypothesized that the rotation was due to an imbalance of torque from MT-associated dynein pulling forces on the nucleus. In this model, an instantaneous imbalance in the net dynein pulling force would arise when, as the MT configuration evolves due to dynamic instability, more microtubules contact one side of the nucleus than the other. Angular trajectories simulated based on this model reproduced motions that were qualitatively similar to those observed experimentally (Figure 2-6A and B). Like the experimental data, the autocorrelation function of the simulated trajectories exhibited short-time fluctuations due to stochastic contacts between the MTs and the nucleus, and a long-time directional persistence in rotation that relaxed as the MT network relaxed due to dynamic instability (Figure 2-6C), as evident by the long-time non-zero tail of the autocorrelation plot. The time scale of the fluctuations, which is evident in the autocorrelation function of ten-minute displacements, depends primarily on the parameter group κ/k_{off} of which a value of 56 pN-s/ μm yielded good quantitative agreement to the experimental data. This value also yielded excellent agreement for the mean-squared displacement (Figure 2-6D). Based on recent FRAP measurements of

cytoplasmic dynein(111), a rough estimate of $k_{off} \sim 1/60 = 0.02s^{-1}$. Then $\kappa \sim 1\text{pN}/\mu\text{m}$, which is not unreasonable for proteins(76).

A testable prediction of this model is that the amount of rotation caused by an anisotropic configuration of MT's should decrease when the centrosome directly underlies the nucleus. As shown in Figure 2-6E, the mean-squared rotation angle measured from the simulations decreased as the centrosome was placed at positions closer to the nuclear centroid. This prediction can be explained by the fact that the dynein-generated torque is smaller when the lever arm length (i.e., the distance from the nuclear centroid to the MT-nucleus contact position) is smaller (Figure 2-5B). We tested this model prediction by patterning cells into symmetrical shapes as discussed below.

Nuclear Rotation Depends on Nuclear-Centrosomal Distance

In stationary, unpatterned cells, the centrosome is typically observed in two dimensional images at one side of the nucleus (Figure 2-7A), and below the mid-plane of the nucleus. It is known that the centrosome is positioned at the cell centroid due to centering by dynamic microtubules interacting with the cell periphery(78). We reasoned that in patterned cells of square shape, the centrosome should be located at the geometrical center of the square; this was indeed found to be the case (Figure 2-7A). The nucleus was also observed close to the center of the square, such that the centrosome overlapped with the nucleus in two-dimensional images (Figure 2-7A). Confocal imaging showed that the centrosome was underneath the nucleus in patterned cells (Figure 2-8). This arrangement was rarely observed in unpatterned cells; the

projected distance between the centrosome and the nuclear centroid was significantly higher in unpatterned cells (Figure 2-7B and C).

Our model predicts that a decrease in nuclear-centrosomal distance should result in decreased torque on the nucleus for a given MT configuration. To test this prediction, we tracked rotation of the nucleus in square cells. The nucleus in square cells was observed to rotate significantly less than unpatterned cells (Figure 2-9), confirming a key prediction of the model. Indeed, as indicated by the solid lines in Figure 2-9, the MSD generated by simulations performed with the centrosome located at the experimentally measured average position in patterned cells agreed quantitatively with experimental measurements.

Discussion

In this study, we quantified the persistent directional rotation of cell nuclei in fibroblasts and used the data to propose a mechanistic model that can predict nuclear motion based on tensional forces on perinuclear microtubules generated by the minus ended motor dynein. In this model, the mean force per dynein molecule depends on the local velocity of the nucleus relative to the microtubule, and the net force and torque on the nucleus depends on the instantaneous configuration of perinuclear microtubules. The model qualitatively captures the dynamic behavior of nuclear rotation, and agrees quantitatively upon fixing one unknown parameter group (κ/k_{off}). We experimentally tested a key prediction of the model that the rotation should depend on the nuclear-centrosomal distance. Together, this work provides the first mechanistic explanation for how nuclear dynein interactions with discrete microtubules emanating from a stationary centrosome can cause nuclear rotation.

The finding that the centrosome is close to the nuclear centroid in patterned cells can be explained by the nearly-isotropic inward flow of actomyosin from the cell periphery(112). As rearward flow continuously occurs from the corners of the squares of the patterned cells(113), 'equal' forces are exerted by rearward flow of actin which causes the nucleus to be centered (although not perfectly depending on the local shape of the lamellipodial protrusions). Because the centrosome is centered at the cell centroid due to microtubule-cortical actin interactions mediated by dynein(78), this forces the nucleus and the centrosome to overlap. In unpatterned cells, the centrosome is always observed on one side of the nucleus, probably due to asymmetrical positioning of the nucleus by rearward actin flow only from the leading edge of the (polarized) cell.

The decrease in nuclear rotation in patterned cells can be interpreted in the light of the model shown in Figure 2-5. When the centrosome is under the nucleus, then torque is generated primarily by microtubules oriented parallel to the lower nuclear surface. When the centrosome is not underneath the nucleus but rather to the side, then the net torque generated is expected to be higher when the MT configuration evolves by dynamic instability to become spontaneously asymmetric. Mathematically, the z-component of the torque decreases to zero when the centrosome is positioned at the nuclear centroid because the radial position vector drawn from the centroid to the point of dynein forces becomes parallel to the microtubule(and mean dynein-force) direction (Figure 2-5B). Also, the lever arm (the distance from the nuclear centroid to the MT-nucleus contact position) is smaller (Figure 2-5B).

That the centrosome is essentially stationary during rotation is consistent with similar findings reported in two other studies(12, 49). Consistent with these findings, the model does not require the centrosome to rotate for the nucleus to rotate - rather, the origin of the torque is due to the asymmetric spatial distribution of nuclear associated microtubules. Thus, the centrosome is actually relevant to the rotation process because its position controls the degree of spatial asymmetry thereby influencing the rate of rotation.

The model qualitatively reproduces our experimental finding that nuclear rotation is a random walk with directional persistence. The fluctuations are a natural consequence of the fact that the microtubule configuration fluctuates due to dynamic instability. The time over which the nuclear rotation persists on average in a given direction is the time it takes for an initial asymmetry in the microtubule configuration to be reversed by dynamic instability. Thus, the model nicely explains a number of features of nuclear rotation that have been observed by us and other researchers.

The model assumes a linear force-speed relationship for dynein, similar to another recent paper on dynein mediated nuclear movement(81). Given the level of coarse graining in the model, small deviations from linearity would not alter the main conclusions of the paper. Although Equation 2-1 allows a load on the motor in the (-)-end direction ($\mathbf{n} \cdot \mathbf{f} > 0$) to enhance the motor speed above v_{\max} , because tangential speeds ($\sim 0.001 \mu\text{m/s}$) are much less than v_{\max} , this situation is rarely encountered in the application of the model. Therefore, any non-linearity in the “force-assisted” region of the force-velocity relation for dynein that is not accounted for in the model should not impact the model predictions.

Dynein pulling has been proposed previously as a mechanism for pulling of microtubule organizing centers(78). A recent model for oscillatory spindle pole body translation in *S. pombe* assumed that directional translation arises from breakage of dynein linkages by the "winning" side in a tug-o-war of competing pulling microtubules(81). In that model, the spindle body translates at nearly constant maximum motor speed until it reaches one end of the cell, consistent with the experimental observations in that system. In contrast, nucleus rotational speeds are stochastic, fluctuating in magnitude and direction, but with values much smaller than the dynein motor speed v_{\max} , suggesting no winning side of the dynein tug-o-war. We also note that there is no direct experimental evidence of dynein-force-induced breakage of dynein linkages in vivo, and our model can explain the relevant observations without invoking this untested assumption. In fact, for observed maximum tangential speed of $s = 0.001 \mu\text{m/s}$, the force over the bond lifetime (given by $s \kappa/k_{\text{off}}$) is significantly smaller than 1 pN for our estimates of κ/k_{off} (see model results). This force is much smaller than forces required for bond breakage that are typically several pN(114).

There is evidence that nuclear rotation can be influenced by other molecules. For example, Lammerding and co-workers(46) showed that over-expression of nesprin-1, a protein that binds the nucleus to the F-actin cytoskeleton, reduces the extent of rotation. This suggests that rotation may at least in part be influenced by frictional drag due to connections with other members of the cytoskeleton. However, we did not observe an increase in the rotation in NIH3T3 fibroblasts on nesprin-1 depletion (Figure 2-10). Similarly, myosin inhibition may increase rotation(12), which again suggests a role for actomyosin in opposing the rotation. Drag in our model is due to dynein motors bound

to those microtubules that oppose the rotation. We cannot rule out drag due to frictional connections with actin or intermediate filaments. While including this effect would add a term similar to the drag due to dynein, it is not expected to change the main conclusions of the model.

Summary of Findings

In this chapter, a mechanical model describing torque generation on the nucleus was proposed. A key prediction of the model is that the magnitude of nuclear rotation depends on the distance between the centrosome and nuclear centroid, which was confirmed by nuclear rotation experiments in patterned cells. Our model provides new insight into how nuclear dynein interactions with discrete microtubules emanating from a stationary centrosome cause rotational torque on the nucleus, which may further help us understand the biological function of nuclear rotation in the near future.

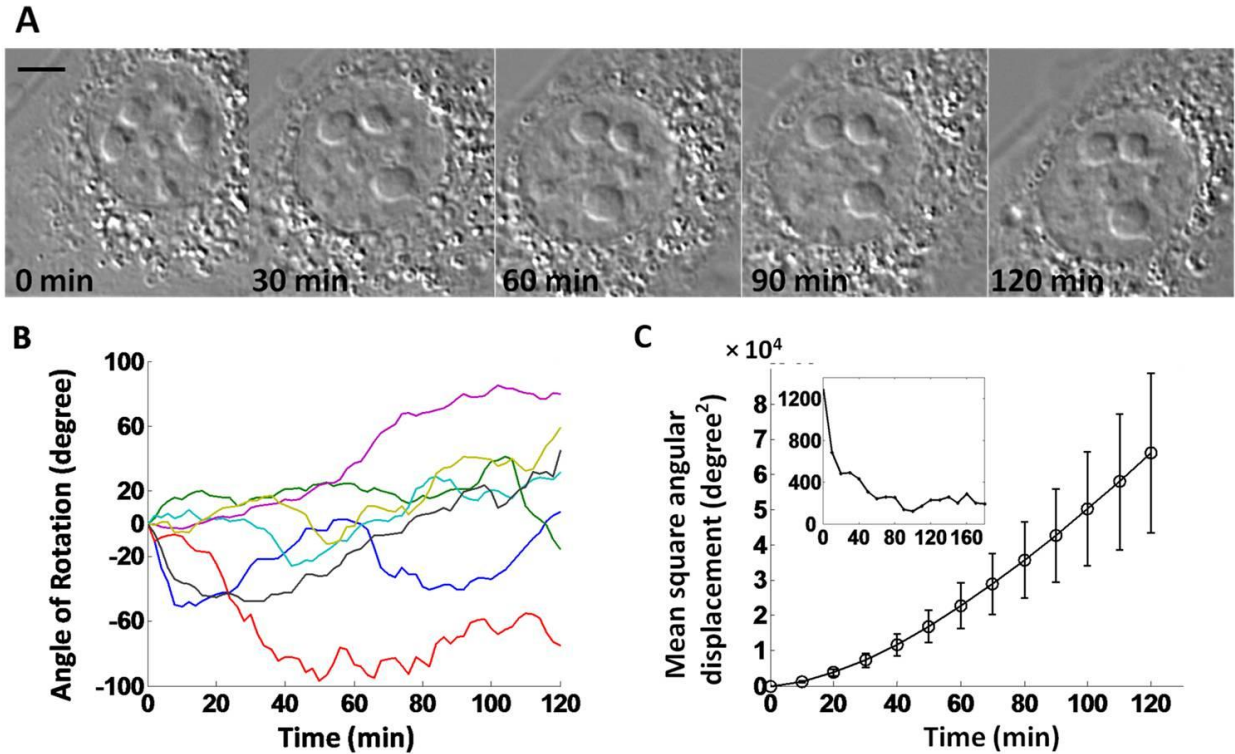


Figure 2-1. Nuclear rotation is a biased random walk in NIH 3T3 fibroblasts. (A) Captured images of a rotating nucleus. Scale bar is 5 μm . (B) Time-dependence of the rotation angle; time between successive data points is two minutes. The angle fluctuates randomly. (C) Time-dependence of the pooled angular mean-squared displacement ($n=25$ cells). The MSD shows a parabolic shape at short times followed by a linear dependence at longer times which indicates a persistent random walk. Inset shows the averaged autocorrelation of angular displacements over 10-min intervals ($\text{degree}^2/\text{min}^2$) indicating a fast decay followed by long time decay, again consistent with the conclusion that the rotation is a persistent random walk. Error bars indicate standard error (SE).

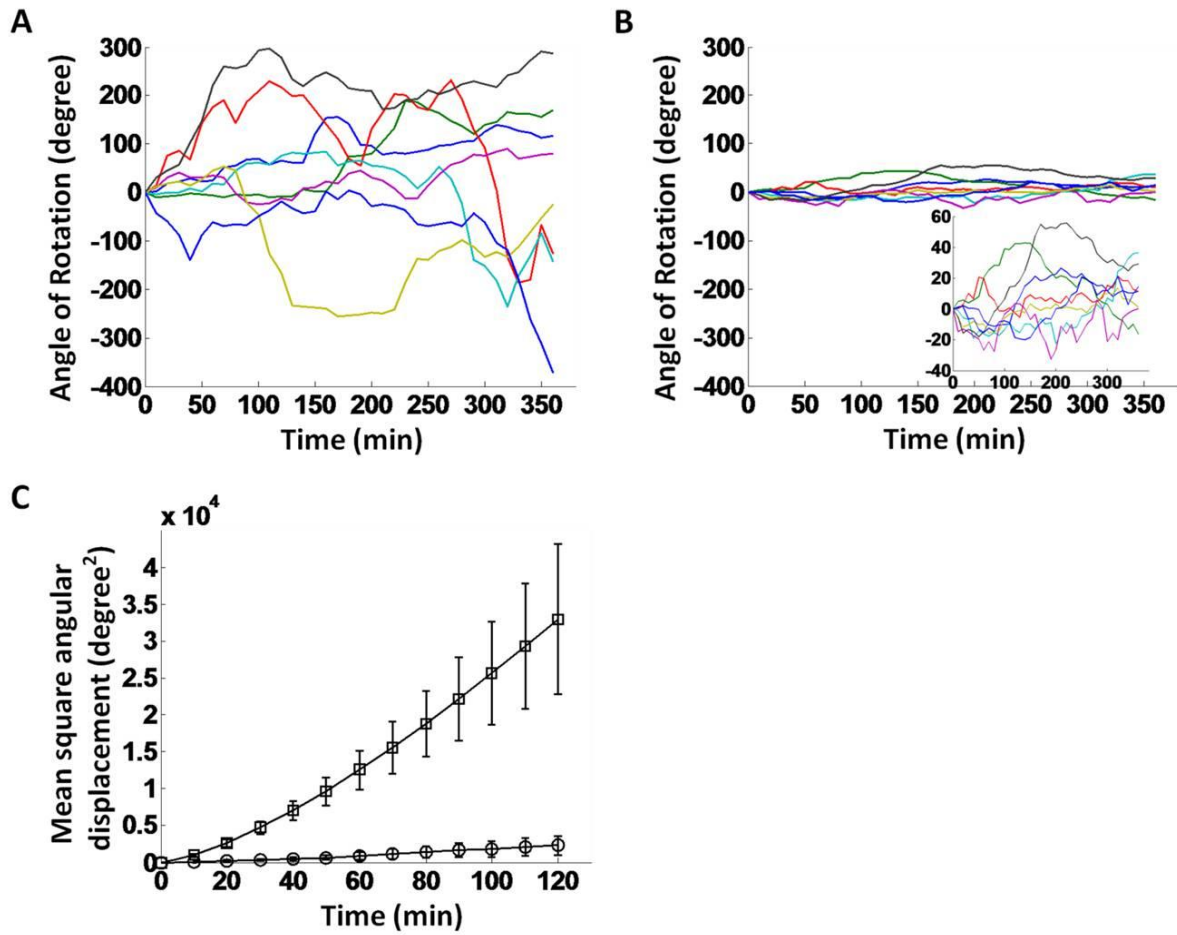


Figure 2-2. Dynein inhibition significantly reduces nuclear rotation. NIH 3T3 fibroblasts were transfected with pDsRed as mock control (A), and pDsRed-CC1 for dynein inhibition (B; inset is re-scaled plot). A clear decrease in the rotation is observed in dynein-inhibited cells. This is confirmed from the MSD plots (C), with MSD in control cells (squares, $n=14$ cells) found to be significantly larger than that in dynein inhibited cells (circles, $n=11$ cells). Error bars indicate SE.

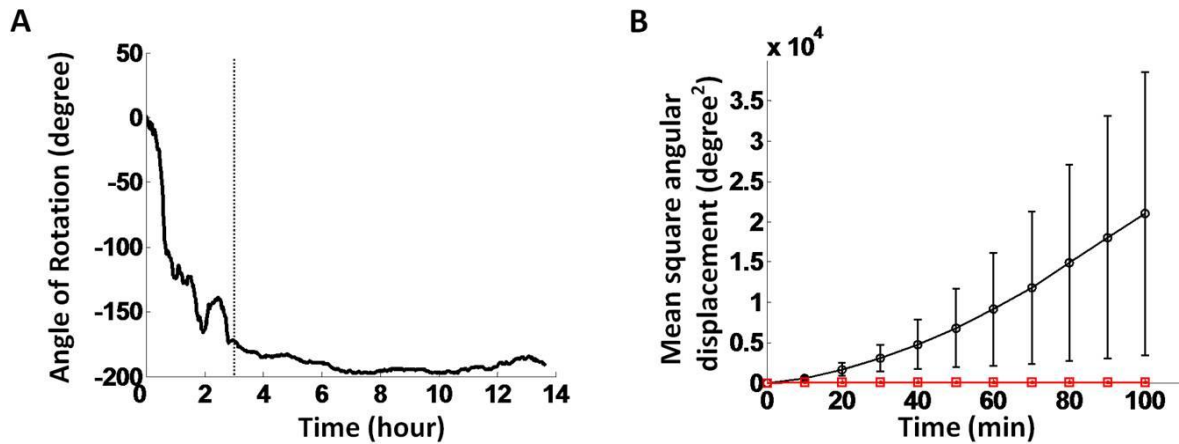


Figure 2-3. Microtubules drive nuclear rotation. (A) Nuclear rotation in NIH 3T3 was tracked for three hours, followed by treatment with nocodazole, and then tracking of nuclear rotation for about 10 hours post treatment. The dash line shows the time when the microtubule polymerization inhibitor, nocodazole, was added (10 μ M). The nucleus did not rotate significantly after the addition of nocodazole. (B) Time-dependence of the pooled angular mean-squared displacement (black, control; red, nocodazole treated, N>5). Error bars indicate SE.

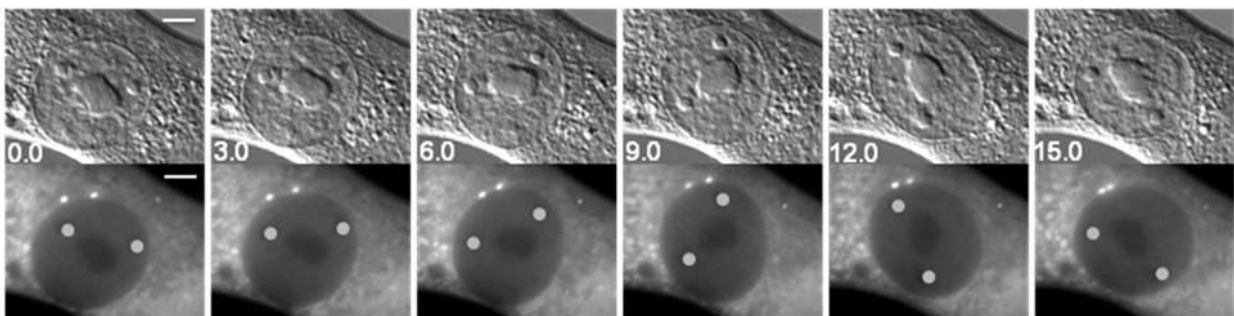


Figure 2-4. The centrosome does not rotate with the nucleus. The top panel is captured DIC images of nuclear rotation in NIH 3T3 fibroblast from movie 1. The time unit is minute. The bottom panel is YFP- γ -tubulin labeled centrosomes. Circles in the fluorescence image mark nucleoli to aid visualization. Scale bars, 5 μ m.

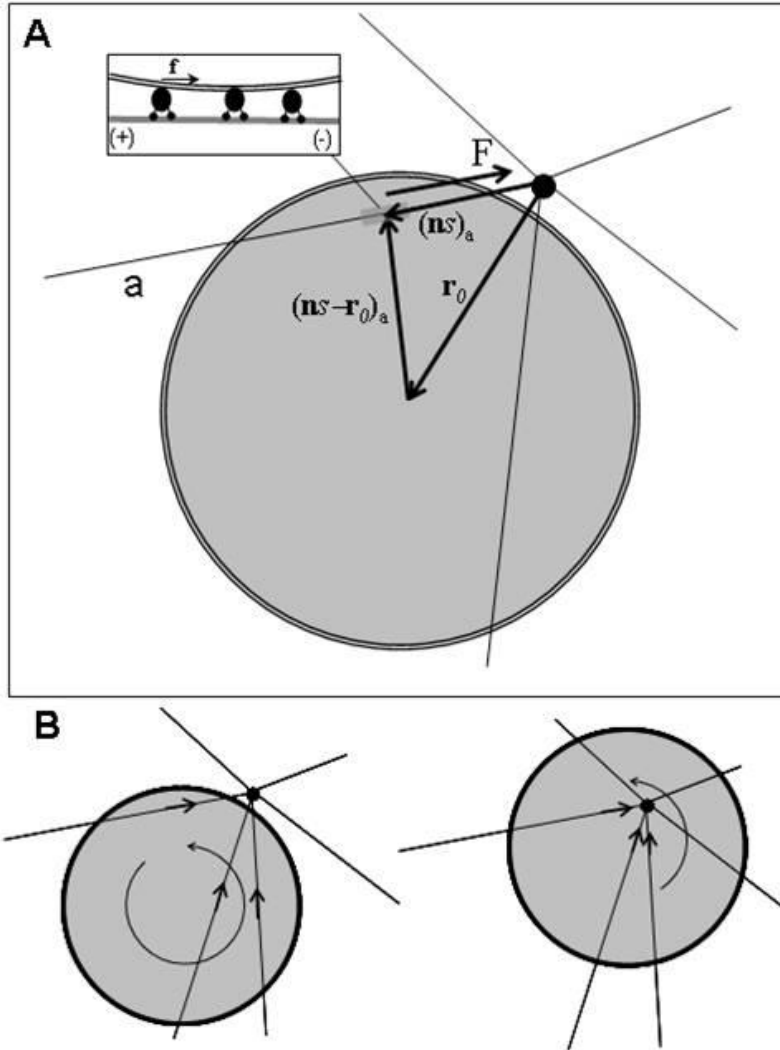


Figure 2-5. Schematic of the nuclear rotation model. (A) Dynein molecules walking on microtubules (straight lines) generate forces (\mathbf{f}) on the nuclear surface directed toward the centrosome (intersection of straight lines). The resulting mean net force \mathbf{F} from the microtubule and the lever arm (vector $\mathbf{n}s - \mathbf{r}_0$ where s is the position on the contour, \mathbf{n} is a unit vector directed towards the MT plus-end, and \mathbf{r}_0 is a unit vector directed from the centrosome to the center of the nucleus) create a torque on the nucleus. (B) The magnitude of the torque depends on the centrosome position, because the lever arm length is smaller when the centrosome is closer to the nucleus centroid.

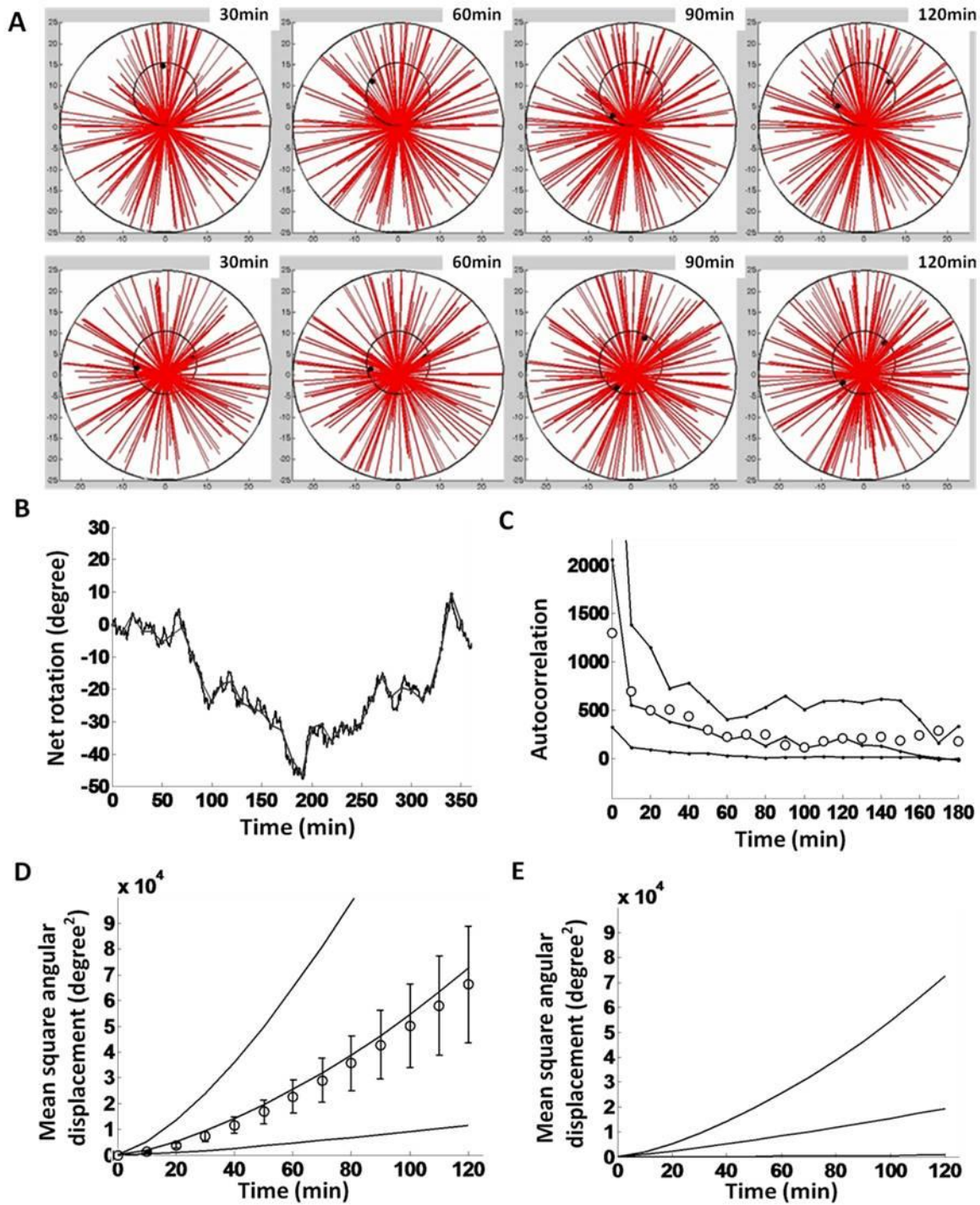


Figure 2-6. Simulations of nuclear rotation in a circular cell. (A) Simulation snapshots of microtubule configuration and nucleus orientation at 30-min intervals, for two different centrosome positions: a distance of eight microns from the nucleus center (upper sequence), and a distance of three microns from nucleus center (lower sequence). Diameter of the cell is 50 microns. (B) Example simulation trajectory of nuclear rotation (default parameters are shown in Table 2-1),

exhibiting short term fluctuations and long-time directional persistence. The same trajectory sampled at 10-min intervals (red, as done in the experiments) is also shown. (C) The autocorrelation function of rotational displacements is plotted versus time increment (solid lines), as calculated by the same method used for Figure 1C (inset), for three values of κ/k_{off} (from upper to lower:

$\kappa/k_{off} = 20 \text{ pN-s}/\mu\text{m}$, $55 \text{ pN-s}/\mu\text{m}$, and $200 \text{ pN-s}/\mu\text{m}$, respectively. Red circles indicate the calculated average autocorrelation function from experimental trajectories. (D) Model predictions of mean-squared angular displacement versus time for the same parameters in (C) (solid lines, from upper to lower: $\kappa/k_{off} = 20 \text{ pN-s}/\mu\text{m}$, $55 \text{ pN-s}/\mu\text{m}$, and $200 \text{ pN-s}/\mu\text{m}$, respectively; red circles are experimental data points). (E) Model predictions of mean-squared angular displacement versus time for three distances between the centrosome position and the nuclear centroid (solid lines, from upper to lower: black, $8 \mu\text{m}$, blue, $3 \mu\text{m}$, and red, $0.5 \mu\text{m}$, respectively).

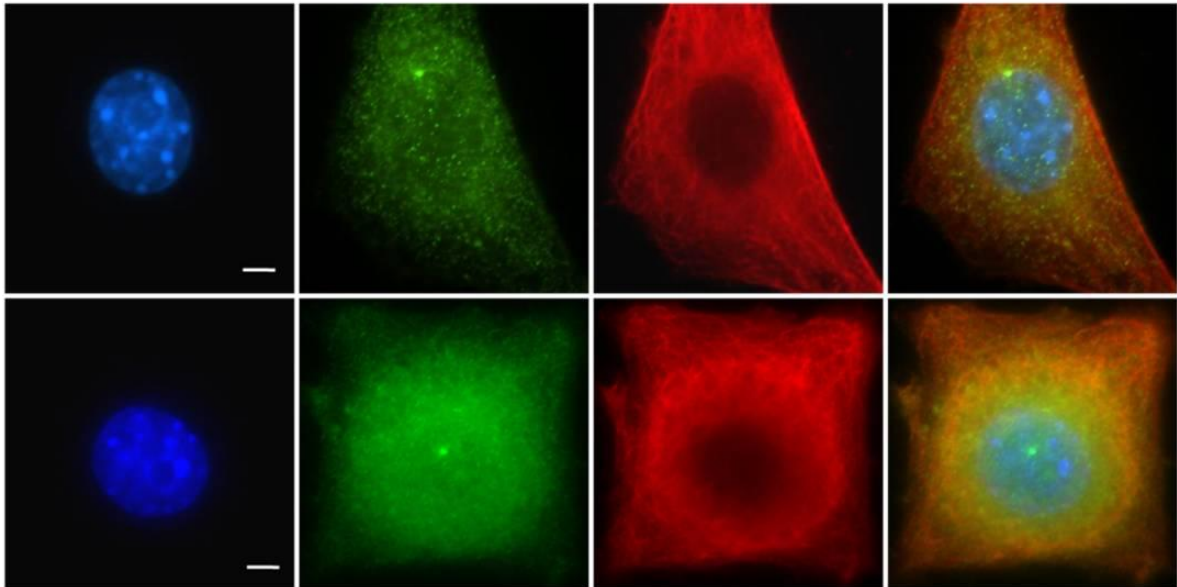
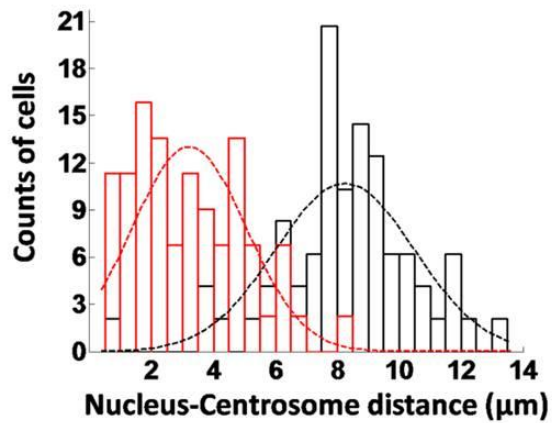
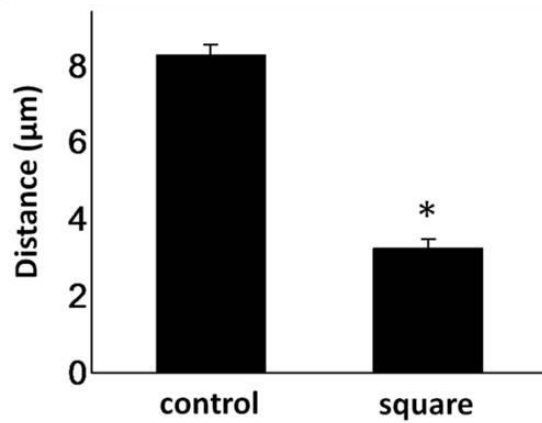
A**B****C**

Figure 2-7. Distance between the centrosome and the nucleus decreased in patterned square NIH 3T3 cells. (A) Positions of the centrosome (green) in unpatterned (top panel) and patterned cells (bottom panel). Nucleus is stained blue and microtubules in red. The last two pictures on the right are overlay images. All scale bars are 5 μm . (B) Distributions of nuclear-centrosomal distance in unpatterned (black) and patterned cells (red). (C) Nuclear-centrosomal distance in patterned square cells is significantly smaller than that in unpatterned cells. Error bars indicate SE; * $p < 0.01$.

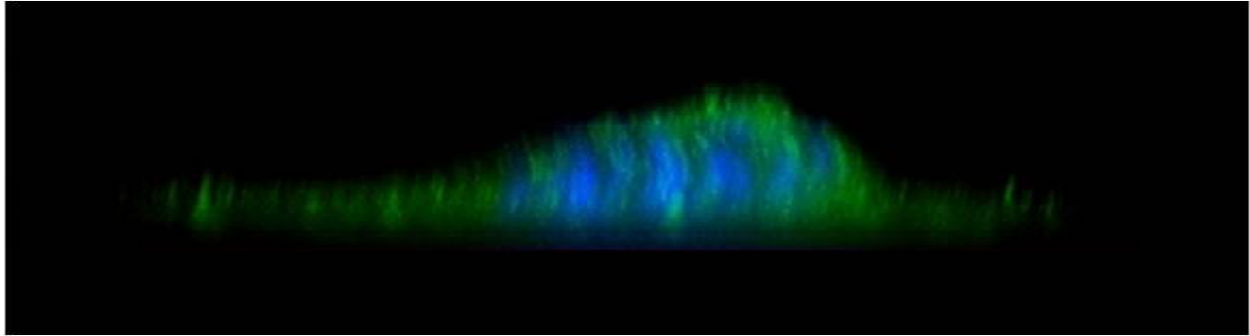


Figure 2-8. The centrosome (arrow, green dot) is underneath the nucleus (blue). Cross section view of centrosome position in square cells acquired with confocal imaging. NIH 3T3 fibroblasts were patterned into square shapes and stained with γ -tubulin antibody and Hoechst 33342. Scale bar, 5 μm

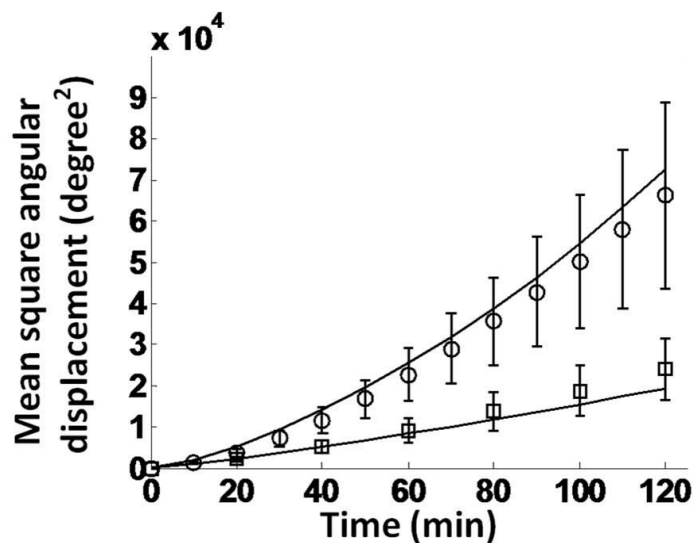


Figure 2-9. Nuclear rotation in unpatterned cells (circles, $n=25$) is significantly larger than that in patterned cells (squares, $n=24$), which agrees with the MSD generated by simulation using experimentally measured average centrosome-nucleus distances of 8 μm and 3 μm , respectively (solid lines). Error bars indicate SE.

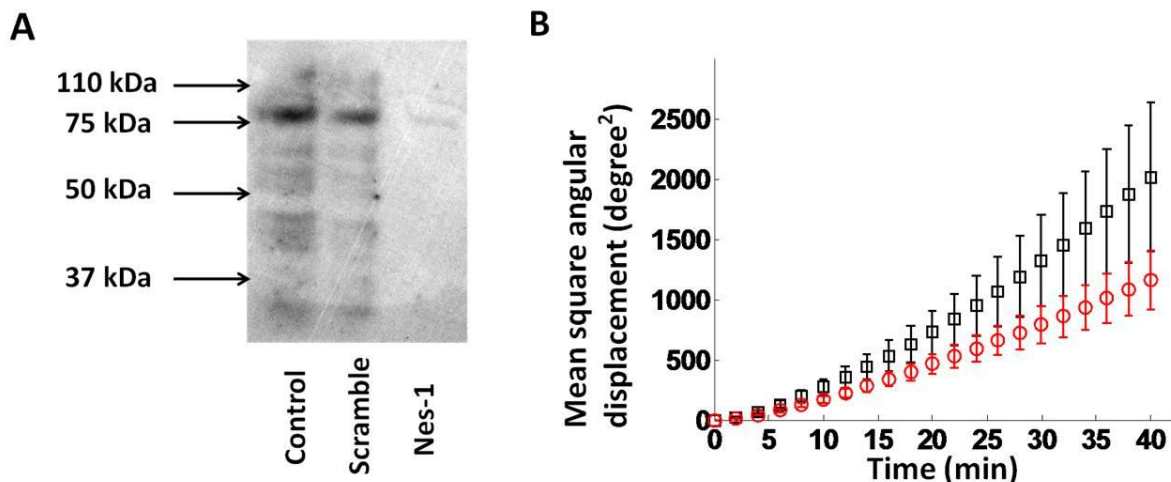


Figure 2-10. Nesprin-1 knock-down affects nuclear rotation. Cells were transfected with 100 nM of SMARTpool siRNAs (Dharmacon, Lafayette, CO) against human nesprin-1 using siLentFect lipid transfection reagent (BioRad, Hercules, CA). The siRNA oligonucleotide target sequences used were as follows: GAAAUUGUCCCUAUUGAUU, GCAAAGCCCUGGAUGAUAG, GAAGAGACGUGGCGAUUGU and CCAAACGGCUGGUGUGAUU. Nontargeting SMARTpool siRNAs served as controls. (A) Western blot analysis of nesprin-1 expression in NIH 3T3 fibroblasts. NIH 3T3 fibroblasts transfected with siRNA targeting nesprin-1 (Nes-1) show a significant reduction in nesprin-1 expression as compared to nontransfected cells (Control) and cells transfected with control siRNA (Scramble). (B) Nuclear rotation in control NIH 3T3 fibroblasts (black square, n=27) is not increased in nesprin-1 knock-down cells (red circles, n=35). Interestingly, a slight decrease is observed in nesprin-1 depleted cells; the p value for the difference at 40 minutes is p=0.08; so this is not statistically significant. MSD was calculated using overlapping time intervals. Error bars indicate SE.

Table 2-1. Nuclear Rotation Model Parameters

Symbol	Parameter	Range	Source	Value Used
f_{\max}	Maximum dynein force	5-8 pN	(115)	7 pN
v_0	Speed of unstressed dynein	0.8 $\mu\text{m/s}$	(109)	0.7 $\mu\text{m/s}$
κ	Dynein spring constant	No measured value		$\kappa/k_{\text{off}} = 56 \text{ pN-s}/\mu\text{m}$
k_{off}	Dynein-nucleus off-rate	No measured value		
ρ	Dynein density (number/length)	No measured value		Not needed
N	Number of microtubules	200-500	(116)	250
V_{pol}	MT polymerization speed	5-10 $\mu\text{m/min}$	(116, 117)	7 $\mu\text{m/min}$
V_{depol}	MT depolymerization speed	15-20 $\mu\text{m/min}$	(116, 117)	17 $\mu\text{m/min}$
k_{cat}	MT catastrophe rate constant	0.01-0.06 s^{-1}	(116, 117)	0.05 s^{-1}
k_{rec}	MT recovery rate constant	0.04-0.2 s^{-1}	(116, 117)	0.19 s^{-1}
σ	MT-Nucleus Interaction Distance		Based on length of cytoplasmic dynein	60 nm

CHAPTER 3 THE NUCLEUS IS IN A TUG-OF-WAR BETWEEN ACTOMYOSIN PULLING FORCES IN A CRAWLING CELL

On cellular length scales, the nucleus is massive (~10-15 microns in diameter) and stiff relative to the cytoplasm. Motion of such a large object in the crowded intracellular space requires a significant expenditure of energy and hence represents a significant task for the motile cell. We found that the nucleus in a single, polarized crawling fibroblast was pulled forward toward the leading edge. The pulling forces originate from actomyosin contraction between the leading edge and the nuclear surface; these forces are opposed by actomyosin pulling in the trailing edge. Microtubules serve to damp fluctuations in nuclear position, but are not required for directional nuclear motion. Our results indicate that the nucleus is under net tension in a crawling cell due to a competition between actomyosin pulling from the front and back of the crawling cell.

Materials and Methods

Cell Culture, Plasmids and Transfection, Drug Treatment

NIH 3T3 fibroblasts were cultured in DMEM (Mediatech, Manassas, VA) with 10% donor bovine serum (Gibco, Grand Island, NY). For microscopy, cells were cultured on glass-bottomed dishes (WPI, Sarasota, FL) coated with 5µg/ml fibronectin (BD Biocoat™, Franklin Lakes, NJ) at 4°C overnight. For photoactivation experiments, cells were serum-starved for two days in DMEM with 1% BSA (Sigma-Aldrich, St. Louis, MO).

Micromanipulation experiments and related figures are attributed to T.J. Chancellor and Agnes Mendonca in the Department of Chemical Engineering, University of Florida. Some of the experiments regarding nuclear movement in migrating cell were done by Nandini Shekhar in the Department of Chemical Engineering, University of Florida.

YFP- γ -tubulin was prepared from the MBA-91 AfCS Set of Subcellular Localization Markers (ATCC, Manassas, VA). GFP-actin was provided by Dr. Donald E. Ingber in Harvard University. EGFP-KASH4 was previously described in (31). mCherry-PA-Rac1 (Addgene plasmid 22027). DsRed-CC1 was kindly provided by Prof. Trina A. Schroer from Johns Hopkins University. Transient transfection of plasmids into NIH 3T3 fibroblasts was performed with LipofactamineTM 2000 transfection reagent (Life Technologies, Invitrogen, Carlsbad, CA).

For microtubule disruption experiment, cells were treated with nocodazole (Sigma-Aldrich, St. Louis, MO) at the final concentration of 1.6 μ M for over one hour prior to the experiment. For myosin inhibition, cells were treated with blebbistatin (EMD, Gibbstown, NJ) at the final concentration of 50 μ M for over one hour prior to the experiment.

Time-Lapse Imaging and Analysis

Time-lapse imaging was performed on a Nikon TE2000 inverted fluorescent microscope with a 40X/1.45NA oil immersion objective and CCD camera (CoolSNAP, HQ², Photometrics, Tucson, AZ). During microscopy, cells were maintained at 37 °C in a temperature, CO₂ and humidity controlled environmental chamber.

Confocal Microscopy and Protein Photo Activation

Protein photo activation is a novel technique developed in the last decade for studying spatio-temporal dynamics of enzyme activity in living cells. This technique is based on biosensors called light-oxygen-voltage (LOV) domains. The idea is that a light-switch biosensor in its closed form was fused to the target protein to block the target protein from binding to any effectors. Then when light with certain wavelength shines on the biosensor, it changes the conformation and releases the inhibition of the target protein. Therefore the target protein would be activated(118).

Recent NMR studies revealed the mechanism of a protein light switch in *Avena sativa* phototropin1: a flavin-binding LOV2 domain interacts with a carboxy-terminal helical extension (J α) in the dark. Photon absorption leads to formation of a covalent bond between Cys 450 and the flavin chromophore, causing conformational changes that result in dissociation and unwinding of the J α helix(118, 119). Hahn and coworkers(63) used LOV2-J α sequence (404–547) as the light switch of the amino terminus of a constitutively active Rac1. They showed that locally photo activation of Rac was sufficient to generate polarized cell movement. Another study by Wang et al.(120) showed similar role of Rac in collective guidance of cell movement using the same method. Machacek et al.(121) applied photo activation of Rho GTPase to study the spatio-temporal coordination of Rho GTPase during cell protrusion.

In our experiment, the samples were imaged on a Leica SP5 DM6000 confocal microscope equipped with a 63X oil immersion objective. For photoactivation, a region in between the nucleus and the edge of a cell, which is approximately the size of the nucleus, was chosen using the ROI (region of interests) function. 488 Argon laser was applied at 1% power to activate Rac1. Images were taken every 10 seconds at 1024X1024 resolution. During microscopy, cells were maintained at 37 °C in a temperature, CO₂ and humidity controlled environmental chamber.

Image Analysis

Image series from cell migration experiments were processed in ImageJ (NIH). Then they were imported into Matlab (MathWorks, Natick, MA). Programs were developed to track the nuclear centroid and the contour of cells.

Image series from the photoactivation experiment were imported into Matlab (MathWorks, Natick, MA), and a program was developed for nuclear position tracking.

After the positions of nuclei in different experiments were obtained, the coordinates were rotated as shown in Figure 3-1. The vector pointing from nuclear centroid at time=0 to the activation center was used as the $\theta=0$ axis in the polar coordinate. All the trajectories were rotated following this rule. The directional movements then were calculated as the projecting distance of the trajectories on the $\theta=0$ axis.

Micromanipulation by Microinjector

Eppendorf Femtojet[®] microinjection system (Eppendorf North America, Hauppauge, NY) was used. The microneedle was inserted underneath the trailing edge of the cell, and then the trailing tail was lifted up. The same method was applied to the leading edge lamellipodia.

Results

Myosin Inhibition In the Trailing Edge Causes Nuclear Motion Toward the Leading Edge without Change in Cell Shape.

To locally inhibit myosin activity, we used a micropipette to introduce a flow of blebbistatin containing solution at high concentrations (500 μM) over the trailing edge. In less than five minutes of local introduction of blebbistatin, the nucleus moved toward the leading edge and away from the trailing edge (Figure 3-2A). This occurred without any appreciable change in trailing edge shape, and without any forward motion of the cell body. We found that nuclear movement toward the leading edge on myosin inhibition in the trailing edge was eliminated when KASH domains were over expressed in fibroblasts (GFP-KASH4 expression competitively inhibits nuclear-cytoskeletal linkages, Figure 3-2A and B, (31)).

Solid-Like Coupling Between the Nucleus and the Trailing Edge.

We next performed micromanipulation experiments in which the trailing edge was detached by introducing the micropipette tip under the trailing edge and snapping it. Trailing edge detachment resulted in movement of the nucleus toward the leading edge (Figure 3-3A). The forward motion of the nucleus on detachment of the trailing edge could be interpreted as due to either pushing forces generated by forward motion of the trailing edge contents, or due to a disruption of the tensile forces on the trailing surface of the nucleus, resulting in a net forward force on the nucleus in a manner as suggested by the myosin inhibition experiment. Forward nuclear motion on trailing edge detachment was eliminated in GFP-KASH expressing cells suggesting a requirement for nuclear-cytoskeletal linkages for the effect (Figure 3-3A, B and C). A closer examination of the dynamics of nuclear shape changes on trailing edge detachment revealed that in control cells, the nucleus underwent considerable deformation while its shape was unaltered in KASH expressing cells (Figure 3-3D). When the trailing edge was detached, the nucleus changed shape from an elliptical, elongated cross-section to a circular cross-section. This shape change again could occur either due to pushing forces as the trailing edge retracts or a dissipation of pulling forces. More interestingly, when a detached trailing edge was again pulled on and extended, the nucleus was observed to almost instantaneously elongate again to nearly its original shape in a myosin dependent manner (Figure 3-3E). This experiment suggests that the nucleus is hardwired with actomyosin tensile structures, because while pushing forces can move the nucleus forward on detachment, elongation of the nucleus due to trailing edge extension cannot be explained by pushing forces in the reverse direction.

The forward motion of the nucleus on local myosin inhibition, and the myosin-dependent solid-like coupling between the nucleus and the trailing edge suggest strongly that the nucleus is pulled toward the trailing edge by actomyosin forces. The transfer of the pulling forces to the nuclear surface occurs through molecular linkages with the cytoskeleton as suggested by the lack of nuclear motion or deformation in GFP-KASH4 expressing cells.

Forward Nuclear Movement does not Require Trailing Edge Detachment

As the trailing edge is mechanically coupled with the nucleus, we next examined the correlation between nuclear motion and trailing edge motion. Forward motion of the nucleus toward the leading edge did not necessarily require the detachment of the trailing edge (Figure 3-4A and B). The forward motion of the nucleus correlated with forward motion of the cell centroid, but not with the trailing edge (Figure 3-4C, D and E). This is not to suggest that nuclear motion does not occur when the trailing edge detached; but significant forward motion can occur of the nucleus without large changes in the shape of the trailing edge.

Forward Motion of the Nucleus Occurs due to Actomyosin Contraction Between the Leading Edge and the Nucleus

If the nucleus is pulled on from the trailing edge, then what causes its motion forward in the absence of significant trailing edge detachment? One hypothesis (originally proposed by Lauffenburger and Horwitz (122)) is that the nucleus is pulled forward by actomyosin contraction occurring in the leading edge. Owing to its large area, myosin inhibition locally and/or detachment of the lamellipodium appeared to present experimental difficulties. To circumvent these problems, we instead adapted the Rac1 photoactivation assay recently introduced by Hahn and coworkers (63, 120, 121).

The idea is to cause local polymerization of F-actin; this newly created F-actin is expected to combine with myosin and result in increased local contraction.

On the creation of local lamellipodium with Rac1 photoactivation, the nucleus was observed to move toward the direction of the lamellipodium (Figure 3-5A and B). The motion of the nucleus was similar to the motion observed in motile cells above. We first examined the role of microtubules in the motion. The trajectories of the nucleus did correlate with centrosomal trajectories (both moved in the general direction of the newly created lamellipodium, Figure 3-5C). However, depolymerization of microtubules with nocodazole did not eliminate the directional motion of the nucleus; on the contrary, nuclear movement increased in the direction of motion and the fluctuations in nuclear position also increased (Figure 3-5D through G, also see Figure 3-1 and Figure 3-6). These results suggest that fluctuations in motion of the nucleus are damped because the nucleus is bound to microtubules (through nuclear envelope-embedded motors such as dynein and/or kinesin). But the directional motion of the nucleus on the formation of new lamellipodia does not depend on microtubule motor activity. Consistent with this picture, we found that the nucleus can move without requiring trailing edge detachment in dynein inhibited cells; the motion is similar to that in control cells because the nucleus tracks the cell centroid (Figure 3-5H, I and J).

On inhibition of myosin activity through blebbistatin treatment, the nucleus did not move directionally in the photoactivation experiment; nor did it move when KASH4 was overexpressed in the cells (Figure 3-5D through G, also see Figure 3-6). Taken together with the microtubule disruption experiments, the results point to actomyosin contraction as the dominant pulling force on the nucleus which moves it forward during motility of

NIH 3T3 fibroblasts. Consistent with this picture, when the lamella was severed with a micropipette, the nucleus was observed to move back; this motion was reduced significantly on over-expression of GFP-KASH in the cell (Figure 3-7).

Discussion

Our results suggest that there is a tug of war between forward pulling and rearward pulling forces on the nuclear surface. The dominant contribution to these pulling forces is from actomyosin contraction. Given that F-actin continuously polymerizes at the leading edge, there is a continuous source of newly polymerizing actin that can contract to pull on the nucleus. The trailing edge is relatively stable in shape (until it detaches), and hence it is reasonable to surmise that the tensile pulling forces in the trailing edge are relatively constant in magnitude. Net forward motion of the nucleus would be predicted to occur when pulling forces at the front exceed those at the back. An actomyosin tug-of-war is thus a simple positioning mechanism for the nucleus in a crawling cell.

This mechanism suggests an intriguing possibility- that contractile forces transmitted through the nucleus to the trailing edge cause detachment of the trailing edge. To test this, we measured the trailing edge detachment frequency in control versus KASH overexpressing cells. There was a significant reduction in the trailing edge detachment frequency in KASH expressing cells (Figure 3-8A, B and C). KASH expressing cells move forward through a sliding of the trailing edge rather than detachment (Figure 3-8D, E and F). As expected, KASH expressing cells migrate poorly (due to a lack of trailing edge detachment)(123). Thus, the nucleus acts as a long transmitter of forces between the front and the back of the cell. While nuclear positioning is clearly important for motion of the nucleus in the direction of the motile

cell, our results also suggest that the positioning mechanism is crucial for normal cell motility.

Summary of Findings

In summary, using two different methods, we were able to show that in single crawling fibroblasts, the nuclear movement is the integrative result of actomyosin pulling forces originating in the leading edge and the trailing edge.

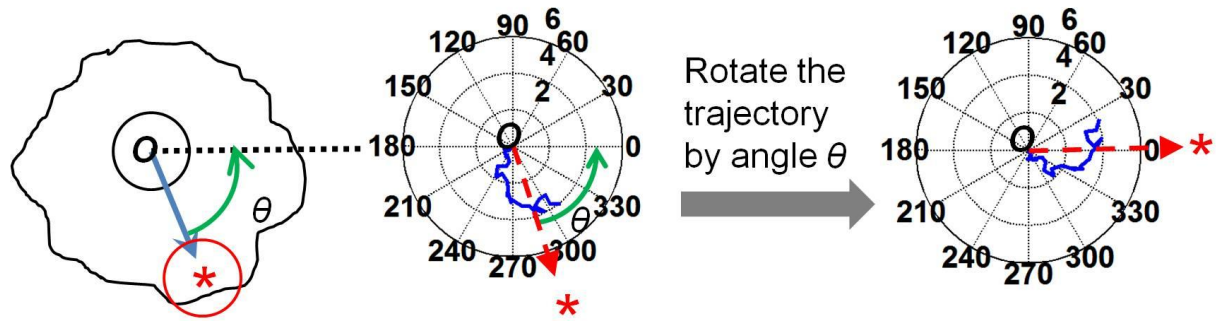


Figure 3-1. Schematic of how collective trajectories of nuclear translation were generated. Red circle represents the activation site. (*) is the center of the activation site. "O" is the centroid of the nucleus. The vector pointing from nuclear centroid to the center of activation site is used as the zero degree in the polar coordinates.

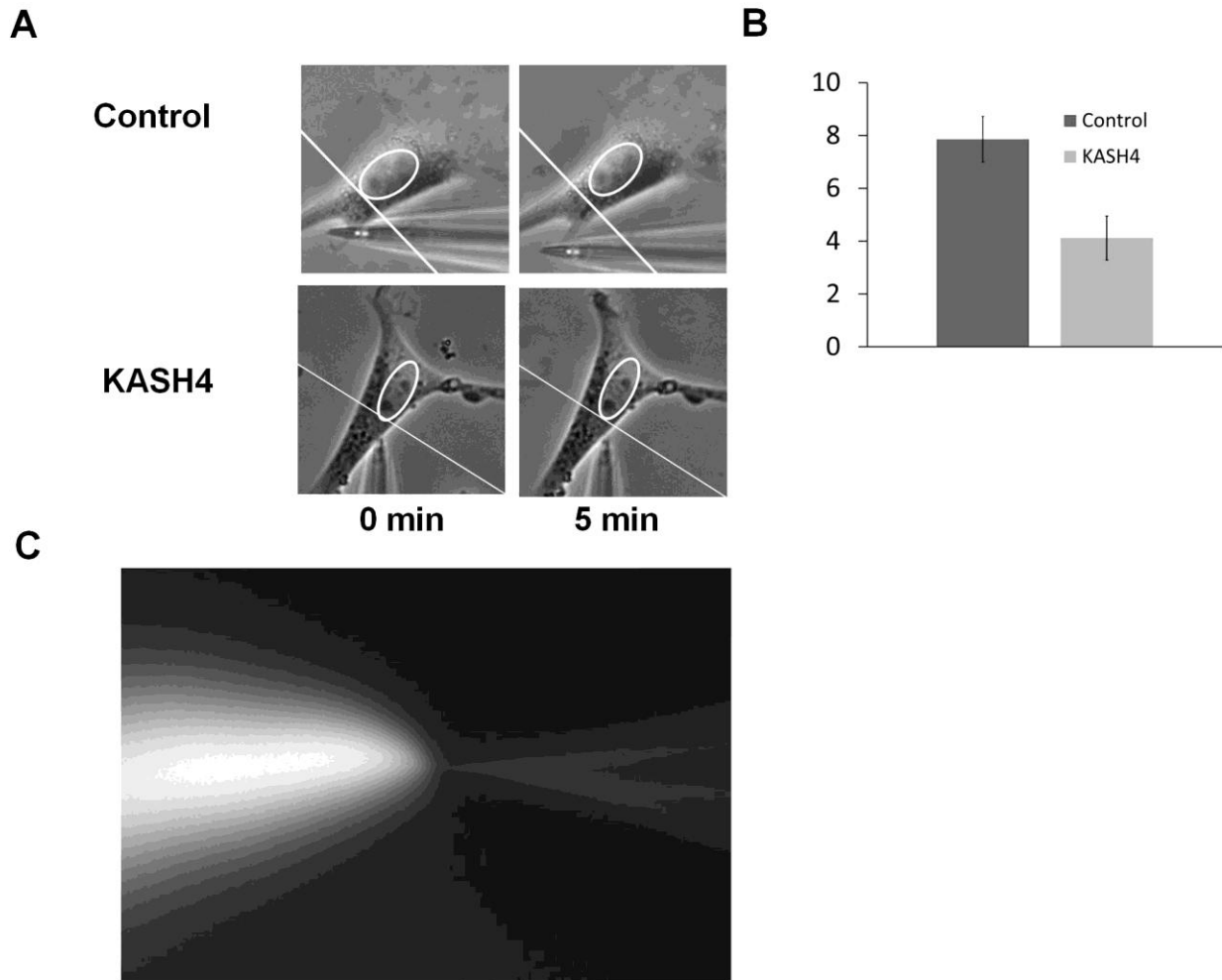


Figure 3-2. Nuclear movement upon local introduction of blebbistatin. (A) Blebbistatin was introduced by micropipette at the trailing edge of the cell. The nucleus moved towards the leading edge, this motion was abolished in cells over-expressing GFP-KASH. (B) Average movement of nuclei upon local introduction of blebbistatin (control, N=10; KASH, N=10, $p < 0.01$). (C) Epi-fluorescent image of blebbistatin spray with 4 kDa FITC Dextran. The micropipette tip was used to localize blebbistatin to the tail region of the cell.

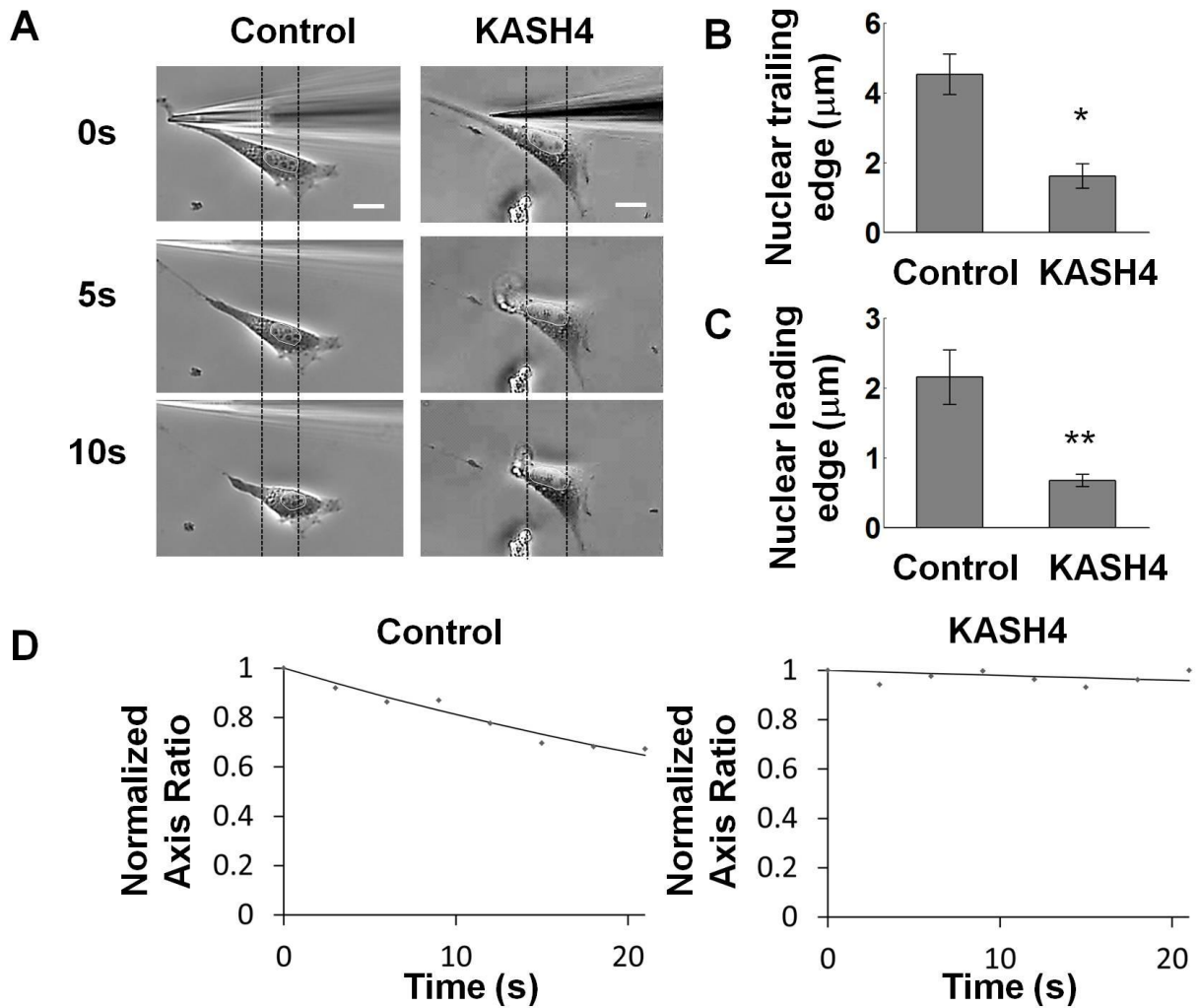


Figure 3-3. Micromanipulation reveals that the nucleus is under tension between the leading edge and trailing edge. (A) Removal of cell trailing edge results in forward nuclear movement in control cells. The forward movement is inhibited in cells transfected with GFP-KASH4. Quantification of the forward movement reveals that both the trailing (B) and leading (C) edges of the nucleus traveled further in control cells than in KASH4 cells. Scale Bar (10 μm). Error bars indicate SEM, *, ** $P < 0.01$. (D) Nuclear Deformation in response to tail release. The nucleus deformed in control cells (N=8), while remained the same shape in KASH4 transfected cells (N=8).

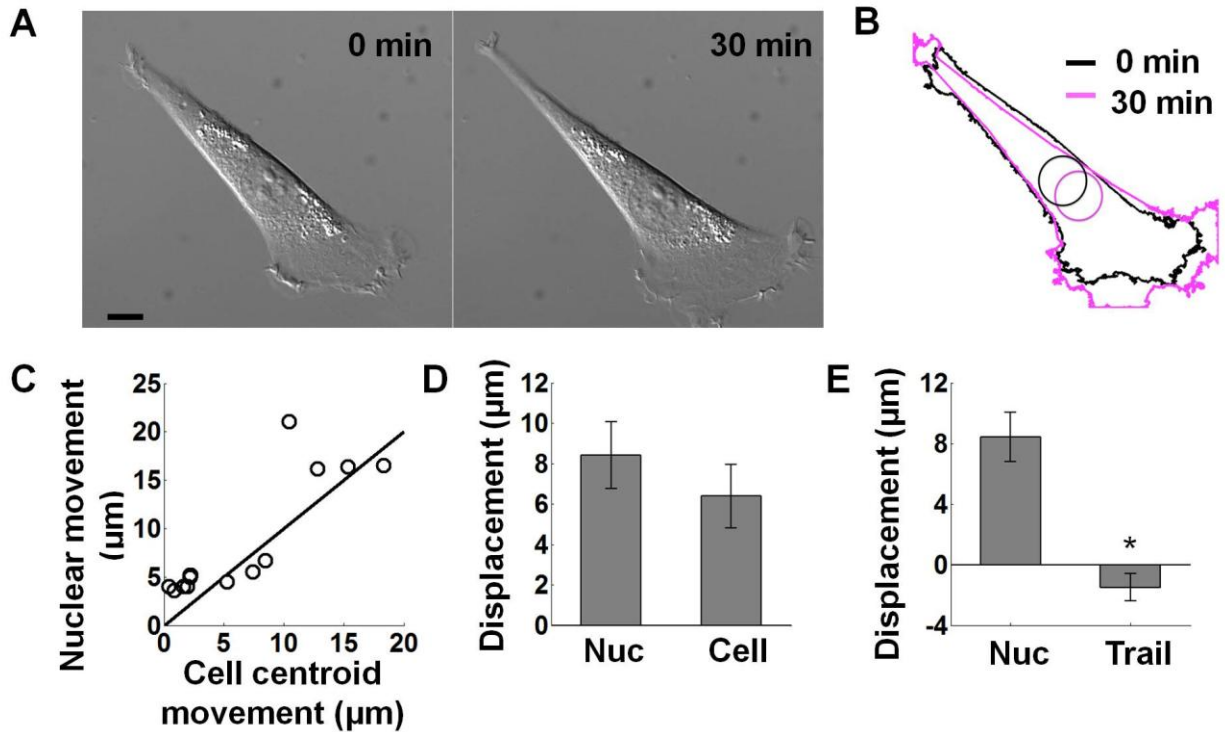


Figure 3-4. Nuclear movement in motile fibroblasts does not required detachment of the trailing edge. (A) Nucleus moved towards leading edge as the lamellipodia formed.(B) The trailing edge retraction is not necessary for moving the nucleus. Superposition of cell outline at zero minute (black) and 30 minute (pink). The nucleus moved forward upon the formation of lamellipodia, while the trailing edge did not retract. (C) The nucleus moved more than the cell centroid did in control (n=13) cells. The red line is $y=x$ line. (D) Comparison of mean movement of the nucleus and cell centroid in 30 minutes shows that they move similar distances. (E) Average displacement of the nucleus and trailing edge in control cells (n=13) in 30 minutes, the trailing edge did not move appreciably, yet the nucleus moves several microns. Error bars indicate standard error of the mean (SEM), ‘*’, $p < 0.01$.

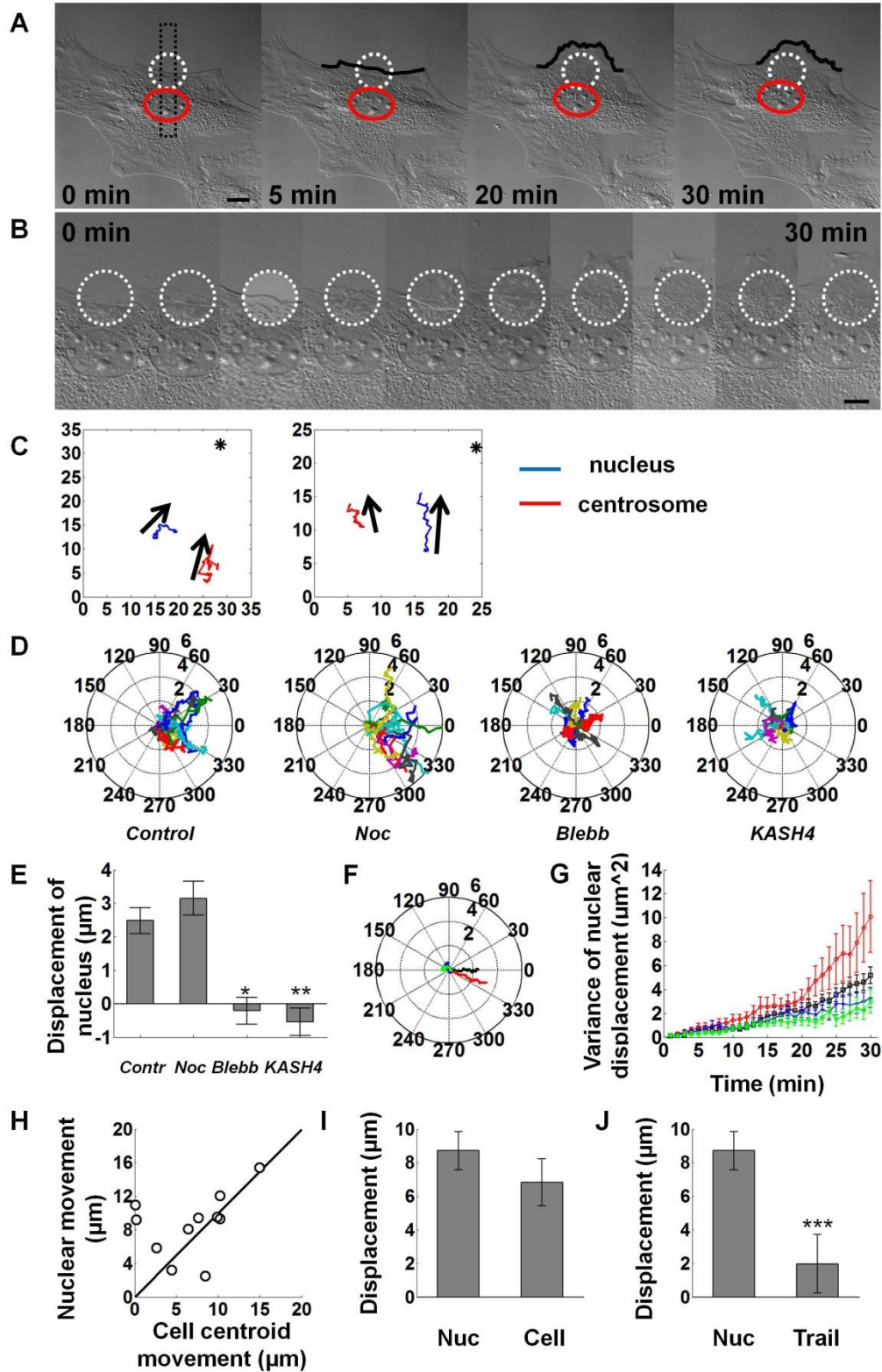


Figure 3-5. Directional nuclear translation upon Rac-1 photo-activation. (A) Frames of a time-lapse recording of a nucleus (red eclipse) moving towards the photo-activation site. Scale bar, 10 μm . (B) Kymograph of images corresponding to

the box in (A). Scale bar, 5 μm . (C) Examples of trajectories of the nucleus (blue) and the centrosome (red) in photoactivation experiments. (D) Trajectories of nuclear movement were overlaid with a common starting point. The zero degree is the direction of activation. The nucleus moved towards the activation site in control and nocodazole treated cells while it did not move much or moved away from the activation sites in blebbistatin treated or KASH4 transfected cells. The unit is micron. (E) Average directional displacement of the nucleus towards the activation site. Positive value means the nucleus moved towards the activation site. (F) Average trajectories of the nucleus and (G) variance of the nuclear displacement in control photoactivation (black, $n=11$), nocodazole treated cells (red, $n=11$), blebbistatin treated cells (blue, $n=10$) and KASH4 transfected cells (green, $n=10$) show that there is larger fluctuation in nocodazole treated cells. (H) Cells are transfected with DsRed - CC1 to inhibit dynein. The nucleus appeared to move more than the cell centroid does upon the inhibition of dynein ($n=11$) in most cells. Red line is $y=x$ line. (I) Average movement of the nucleus and cell centroid in dynein inhibited cells in 30 minutes. Unlike in control cells, the nucleus moved slightly more than the cell centroid. (J) Average movement of the nucleus and trailing edge in control cells ($n=11$) in 30 minutes, the trailing edge did not move significantly. Error bars indicate standard error of the mean (SEM), ‘*’, ‘**’, ‘***’, $p < 0.01$.

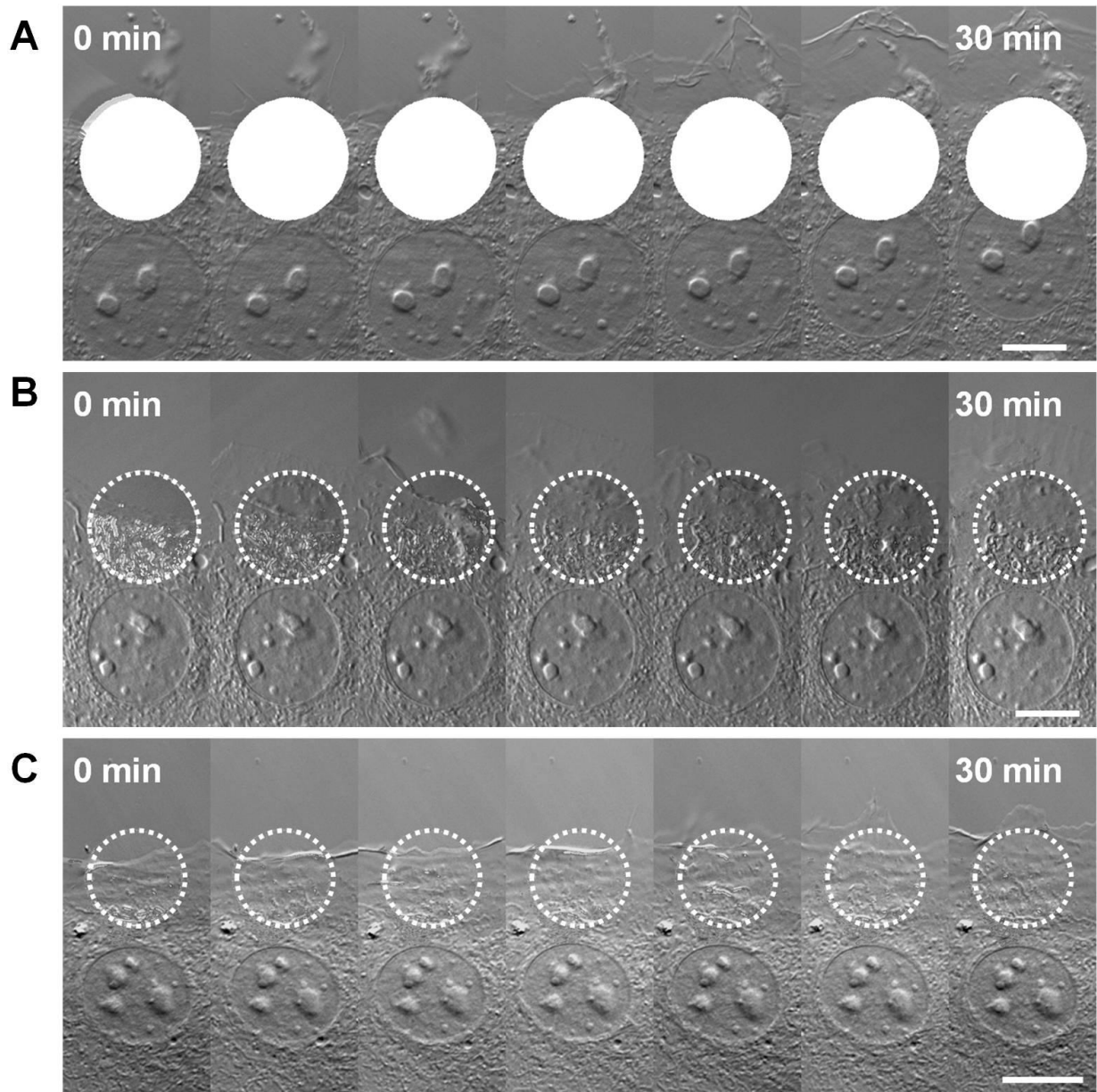


Figure 3-6. Kymograph of photo activation experiments. (A) Nocodazole treated cells. (B) Blebbistatin treated cells. (C) GFP-KASH4 transfected cells. Scale bars, 10 μ m.

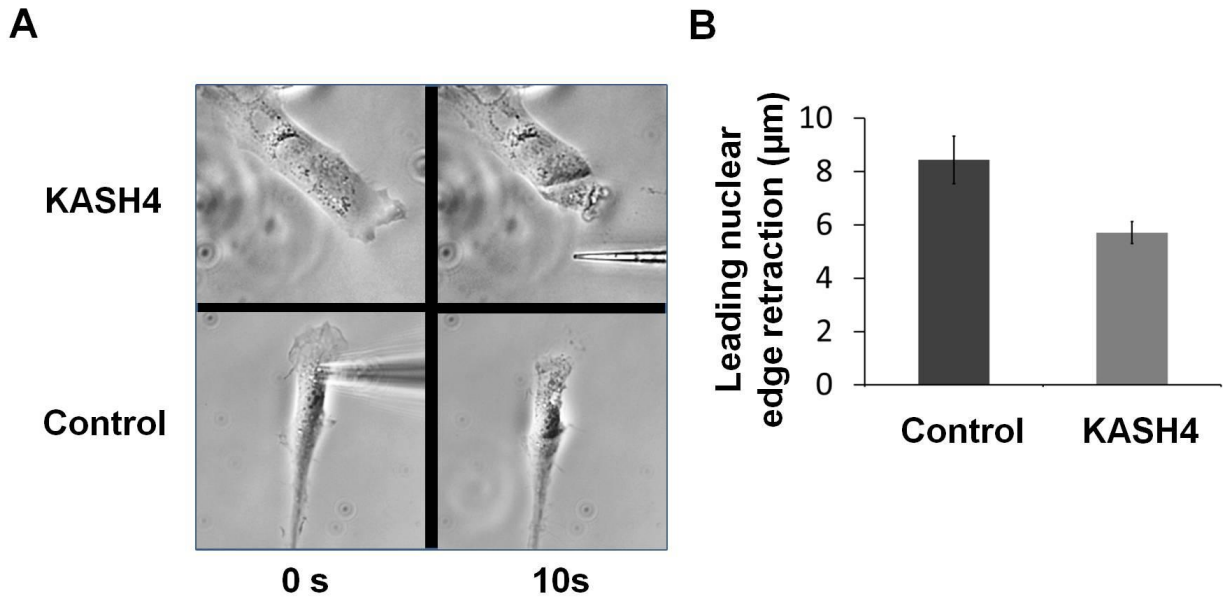


Figure 3-7. Nuclear retraction due to lamellipodia release. (A) Captured images of cells before and after the release of leading edge lamellipodia. (B) The leading edge of the nucleus retracted more in control cells than that in KASH4 transfected cells upon the release of cell leading edge lamellipodia.

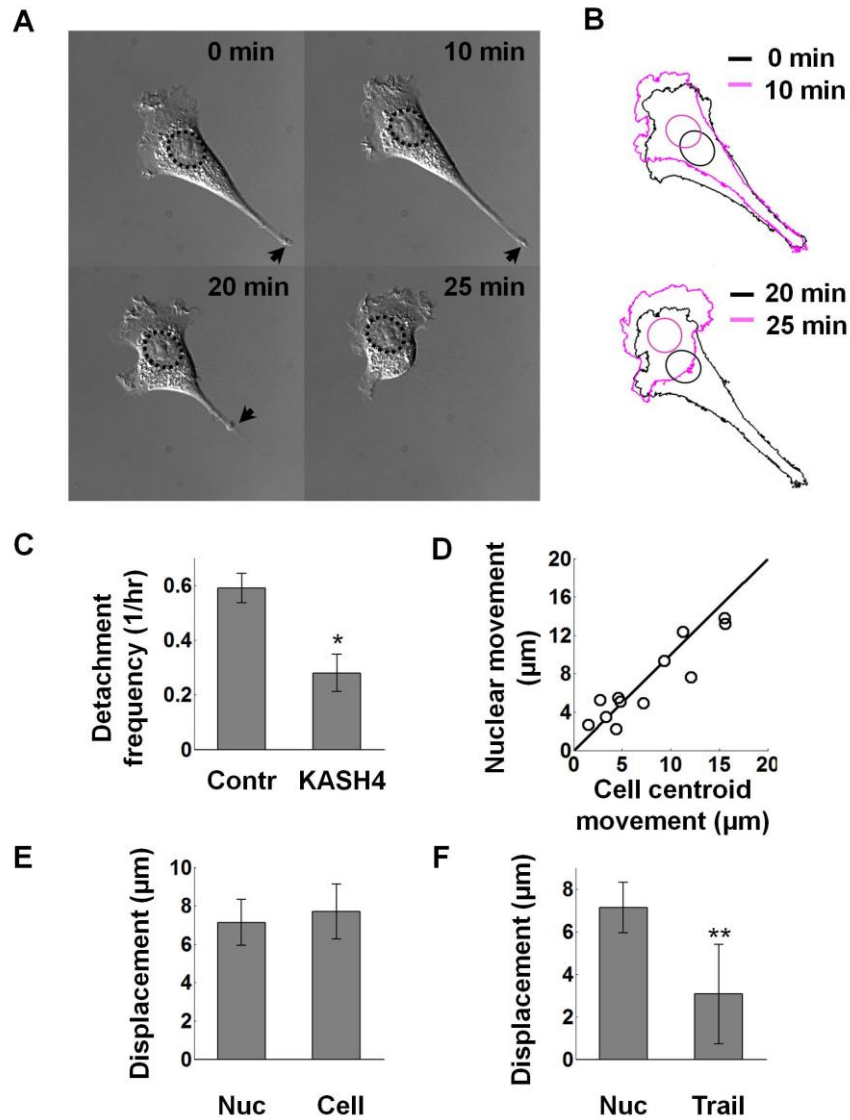


Figure 3-8. Effect of KASH on trailing edge detachment. (A) Captured images of the trailing edge detachment during forward protrusion of an NIH 3T3 fibroblast. (B) Superposition of cell outline at different time points. The nucleus kept moving towards the leading edge. (C) Trailing edge detachment frequency is much higher in control (n=24) cells than in KASH4 transfected cells (n=20). (D) Nuclear movement is highly correlated with cell centroid movement in KASH4 (n=11) transfected cells. Most nuclei moved similar distance as or less than the cell centroid did. Red line is $y=x$ line. (E) Average movement of the nucleus and cell centroid in KASH4 (D, n=11) transfected cells in 30 minutes also show that they moved similar distances. (G) Average movement of the nucleus and trailing edge in KASH4 transfected cells (n=11) in 30 minutes, the trailing move forward, while it was much less than the nucleus did. Error bars indicate standard error of the mean (SEM), ‘*’, ‘**’, $p < 0.01$.

CHAPTER 4 EFFECTS OF DYNEIN MOTOR ON MICROTUBULE MECHANICS AND CENTROSOME CENTERING

In order to determine forces on intracellular microtubules, we measured shape changes of individual microtubules following laser severing in bovine capillary endothelial (BCE) cells. Surprisingly, regions near newly created minus ends increased in curvature following severing, while regions near new microtubule plus ends depolymerized without any observable change in shape. With dynein inhibited, regions near severed minus ends straightened rapidly following severing. These observations suggest that dynein exerts a pulling force on the microtubule which buckles the newly created minus end. Moreover, the lack of any observable straightening suggests that dynein prevents lateral motion of microtubules. To explain these results, we developed a model for intracellular microtubule mechanics which predicts the enhanced buckling at the minus end of a severed microtubule. Our results show that microtubule shapes reflect a *dynamic* force balance, in which dynein motor and friction forces dominate elastic forces arising from bending moments. A centrosomal array of microtubules subjected to dynein pulling forces and resisted by dynein friction is predicted to center on the experimentally observed timescale, with or without the pushing forces derived from microtubule buckling at the cell periphery.

This is reproduced from a paper previously published on Molecular Biology of the Cell with permission from the American Society for Cell Biology. Modeling and simulations are attributed to Dr. Richard B. Dickinson, Dr. Anthony J.C. Ladd and Dr. Gaurav Misra in the Department of Chemical Engineering, University of Florida.

Materials and Methods

Cell Culture, Plasmids and Transfection

Bovine capillary endothelial (BCE) cells were cultured in DMEM (Mediatech, Manassas, VA) with 10% donor bovine serum (Gibco, Grand Island, NY), 1% HEPES (Mediatech), 1% GPS (L-Glutamine–penicillin–streptomycin solution, SIGMA-ALDRICH,) and bFGF (2 ng/ml, Sigma, St. Louis, MO). For microscopy, cells were cultured on glass-bottomed dishes (MatTek Corp, Ashland, TX). These are stationary interphase cells. They are non-confluent and un-synchronized. Adenoviral EGFP- α -tubulin was provided by Prof. Donald Ingber. DsRed-CC1 plasmid was provided by Prof. Trina Schroer. YFP- γ -tubulin was prepared from the MBA-91 AfCS Set of Subcellular Localization Markers (ATCC, Manassas, VA). Transient transfection of plasmids into BCEs was done with Effectene[®] Transfection Reagent (Qiagen, Valencia, VA).

Time-Lapse Imaging and Analysis

Time-lapse imaging was performed on a Nikon TE2000 inverted fluorescent microscope with a 60X/1.49NA objective and CCD camera (CoolSNAP, HQ², Photometrics, Tucson, AZ). During microscopy, cells were maintained at 37 °C in a temperature, CO₂, and humidity controlled environmental chamber. Images of the centrosome were taken every two minutes and imported into MATLAB (Mathwork, Natick, MA). The positions of the centrosome were calculated to sub-pixel resolution using previously published image correlation methods (103). The autocorrelation function (Figure 4-1) was calculated from the x and y position fluctuations in seven cells tracked for 1-2 hours.

Cell Shape Patterning

Cell shape patterning was done by using the micro-contact printing technique described in (105). Molds for the stamps were produced with the UV lithography technique by illuminating a positive photoresist through a chrome photomask on which micropatterns were designed (Photo Sciences, Inc., Torrance, CA). PDMS (Sylgard 184 kit, Dow Corning, Midland, MI) was cast on the resist mold and cured. For micropatterning, the PDMS stamp was treated with 50 μ g/ml human fibronectin solution (BD Biocoat™, Franklin Lakes, NJ). The stamp was then dried and placed onto the substrate onto which the cells were plated. Ibidi dishes (Ibidi, Verona, WI) were chosen to be the substrate. After 5 min, the stamp was removed and the remaining area was blocked with PLL-g-Poly-ethylene glycol (SuSoS AG, Dübendorf, Switzerland), preventing protein adsorption and cell attachment. After treatment the surface was washed and cells were plated.

Laser Ablation

Laser ablation, first used on living cells in the 1960's(124), has been recently shown to be a powerful tool for testing mechanical models of force generation in the cytoskeleton(103, 125-127) . The method focuses ultrashort pulses of a laser beam on a living microtubule or actomyosin stress fiber(128, 129). A large amount of energy is generated in the focused spot resulting in vaporization of material and severing of the cytoskeleton. The short duration of the pulses (picoseconds or femtoseconds) ensures that the amount of power (energy/time) is high but the total energy delivered is low, which minimizes damage to the cell due to energy dissipation outside the ablated spot. When the energy is focused through a high-resolution objective, a single microtubule or a single actomyosin bundle can be severed(130, 131). Severing cytoskeletal filaments

instantaneously perturbs the cytoskeletal mechanical force balance, and imaging the subsequent dynamic changes in cytoskeletal configuration provides *in vivo* quantitative experimental data for testing mechanical models of force generation in the intact cytoskeleton.

A number of recent studies have used laser ablation to measure these properties in living cells(103, 125-127, 132). Severing a single stress fiber causes a retraction of the severed edges. This retraction is due to instantaneous dissipation of all tension in the fiber. Inhibiting myosin eliminates the retraction of the severed edges(103, 125). The first observations of this phenomenon indicated that the retraction followed an exponential form such that the rate of translation of the severed edge was high immediately after severing but slowed down and eventually became zero at steady state(125). Using a Kelvin-Voight mechanical model for viscoelasticity consisting of a spring and dashpot in parallel, Kumar *et al.*(125) modeled the exponential translation of the severed edge. This work was significant because it demonstrated the use of laser ablation for testing mechanical properties of the cytoskeleton *in vivo*. Kumar *et al.*(125) also showed that that stresses of nearly 700 Pa could be dissipated by severing a single actomyosin fiber in endothelial cells. Thus, the stress fiber is in mechanical continuum with the underlying adhesive substrate.

To understand the origin of the exponential retraction of the severed stress fiber ends, Russell *et al.*(103) carried out laser ablation of cells expressing labeled alpha-actinin which marks dense bodies and allows the quantification of stress fiber sarcomere lengths. Based on these results, they proposed a simple mechanical model for the stress fiber sarcomere. Tanner *et al.*(127) found that peripheral SFs have

different viscoelastic properties from interior fibers; the two sub-populations also play distinct mechanical roles.

In addition to testing mechanical models of cytoskeletal force generation, laser ablation has been a useful tool for determining the effect of force on intracellular protein dynamics. Lele *et al.*(133) used laser ablation to sever stress fibers, and then performed fluorescence recovery after photobleaching (FRAP) experiments to measure protein exchange dynamics in the associated focal adhesion. Using this method, the authors demonstrated that dissipating stress fiber tension resulted in an increase in the dissociation rate constant of zyxin, but not vinculin, in focal adhesions of endothelial cells. The advantage of using laser ablation in these experiments was that severing a stress fiber instantaneously dissipates tension at the focal adhesion, and FRAP experiments before and after ablation allow reliable comparison of protein exchange dynamics. Another study showed that severing of individual stress fibers caused a loss of zyxin from both SFs and focal adhesions. This study also demonstrated that retraction of the severed stress fiber can actually nucleate new adhesion sites along the retracting fiber(132).

To investigate forces acting at the junctional network of disc epithelial cells, Farhadifar *et al.*(134) perturbed cell monolayers by ablating cell-cell junctions with a UV laser beam. Measuring the contracting area and distance of the network after laser ablation gave a good estimation of parameters in their model which explained the packing geometry of epithelial cells in monolayers. Tinevez *et al.* (135) performed local laser ablation of the cell cortex in L929 fibroblasts to test whether bleb formation is pressure-driven. Indeed, a bleb grew from the site of ablation immediately, which

confirmed the hypothesis that bleb growth was a direct consequence of cytoplasmic pressure. They further investigated the relationship between cortical tension and bleb formation and expansion. In another study by Mayer *et al.*(136), they ablated the actomyosin meshwork in polarizing *C. elegans* zygote at different positions (regions with or without cortical flow) and in different directions (orthogonal or parallel to the cortical flow). The results showed how cortical flow was associated with anisotropies in cortical tension, and further answered the question how actomyosin contractility and cortical tension interact to generate large-scale flow.

Laser ablation studies are increasingly being used in creative ways to answer fundamental questions related to microtubule function. For example, one study used laser ablation to disrupt microtubule interactions with the bud neck in budding yeast(137). This caused mitotic exit suggesting that cytoplasmic microtubules enable the monitoring of the spindle location and mitotic exit in the dividing cell in the event of positioning errors. Another study showed that ablating the centrosome does not inhibit axon extension and growth, revealing a role for acentrosomal nucleation of microtubules in early neuronal development(138). Laser ablation has also been used to study microtubule dynamics. Colombelli *et al.*(139) developed a new protocol to measure shrinkage rate, growth rate and rescue frequency simultaneously with high temporal and spatial specificity in live cells. Wakida *et al.*(140) used laser ablation to show that the microtubule depolymerization rate in living PTK2 cells was location dependent.

In our experiments, we used laser ablation to cut a single microtubule. An inverted (Zeiss Axiovert 200M) laser scanning confocal microscope (LSM 510 NLO) was used in laser ablation experiments with a 63X, 1.4-NA Plan-Approchromatic oil immersion lens

(Zeiss). A Ti:Sapphire laser (Chameleon XR, Coherent) was used to sever the microtubules as described previously (103, 125, 133). The Ti:Sapphire laser was focused through the objective and scanned over a thin, $\sim 0.14 \mu\text{m}$, rectangle orthogonally crossing the width of the microtubule for 1 iteration. A wavelength of 790 nm was used with a laser-head power of 2W, pulse duration of 140 fs and repetition rate of 90 MHz. After ablation confocal scans were collected using Zeiss LSM 510 4.2 software at 2-5 s per frame. The root-mean-square curvature was estimated from microtubule traces by fitting a one dimensional Gaussian approximately orthogonally across the microtubule (82, 141, 142). Coordinates were smoothed to eliminate short wavelength measurement error and preserve long wavelength microtubule buckles.

Severing produced two microtubule ends with a nearly three folds difference in their rates of depolymerization (Figure 4-2). From experiments where the plus end was clearly visible, we found that the newly created minus end always depolymerized much slower than the newly created plus end, consistent with previous studies(139, 140, 143). The large difference in depolymerization rates allowed us to clearly identify the severed ends as plus and minus ends.

Results

Dynamics of Severed Microtubules

A large fraction of the microtubules in living cells are bent, with stored elastic energy apparently arising either from cytoplasmic motion (144) or from microtubules buckling under continual polymerization against the cell periphery (73, 76). It has been suggested that the bending stresses in the microtubule are balanced by compressive forces propagating from the microtubule tip, reinforced by lateral forces arising from elastic deformation of the surrounding cytomatrix (73). We directly tested this

assumption by severing bent microtubules in BCE cells to remove the longitudinal force at a point along the microtubule length. The two freed ends near the cut behaved differently after severing. Freed plus ends rapidly depolymerized along the original contour of the microtubule (the plus and minus ends were identified as explained in Materials and Methods). On the other hand the more slowly depolymerizing segments near freed minus ends consistently increased in curvature after severing (Figure 4-3A and Figure 4-4), although the increase varied from microtubule to microtubule (Figure 4-5). We found no correlation between the initial curvature of the microtubule and the extent to which curvature increased on severing (Figure 4-5A), nor was there any correlation between the increase in curvature after severing and the distance of the cut from the cell periphery (Figure 4-5B).

Previous work has implicated dynein in anterograde transport of microtubule buckles (82). We therefore investigated the role of cytoplasmic dynein in the bending and pinning of severed microtubules. Cells were transfected with a plasmid encoding DsRed-CC1 which competitively binds to dynein (107). Dynein inhibition was confirmed by dispersion of the Golgi complex (27), as shown in Figure 4-6; microtubules remained anchored to the centrosome (Figure 4-7) consistent with previous reports (84). In dynein-inhibited cells, segments near a free minus end did not show any increase in curvature following severing; instead, the microtubules straightened rapidly, on timescales of the order of a few seconds (Figure 4-3B). An increase in curvature in normal cells and a decrease in curvature in dynein-inhibited cells was consistently observed for severed minus-end microtubules (bar graph in Figure 4-3B).

The dynein-dependent increase in curvature of severed minus ends suggests that motor forces, directed toward the plus end, pull along the length of the microtubule. Because the increase in curvature after severing was consistently observed (Figure 4-5A) and found to be independent of the distance from the periphery (Figure 4-5B), we surmise that microtubules are under tension along most of their length (although tips near the cell periphery are likely to be under compression due to polymerization forces (73). How might dynein generate pulling forces along a microtubule? We hypothesize that dynein molecules linking the cytomatrix to the microtubules along their lengths pull on microtubules as they walk toward the minus end.

The experimental observations also show that dynein contributes a significant frictional resistance to the motion of microtubules, because in normal cells we see no evidence of straightening, whereas in dynein-inhibited cells microtubules straighten on timescales of a few seconds. This observation could be explained by the transient nature of the cytomatrix-dynein-microtubule linkage leading to protein friction opposing microtubule motion.

Model for Dynein-Generated Microtubule Forces

We next formulated a model for dynein force generation which considers the average behavior of an ensemble of motors, transiently linking microtubules to the cytomatrix. Once a cytomatrix-linked motor binds to the microtubule, it exerts a force along the local tangent to the microtubule as it walks towards the minus end (see schematic in Figure 4-8A); the motor also exerts a force in response to motion of the attachment point. Assuming dynein-cytomatrix linkages dissociate with first-order kinetics, the ensemble-averaged force density (force per unit length) along the microtubule is then given by

$$\mathbf{K} = \rho f_0 \left(1 - \frac{\mathbf{t} \cdot \mathbf{v}}{v_0}\right) \mathbf{t} - \rho \gamma (\mathbf{1} - \mathbf{t} \mathbf{t}) \cdot \mathbf{v} \quad (4-1)$$

where $\rho = 2 \mu\text{m}^{-1}$ is the density of dynein-cytomatrix linkages (number of linkages per unit length), f_0 is the average force per linkage on a stationary microtubule ($\sim 8\text{pN}$) and v_0 is the speed of the force-free motor ($0.8 \mu\text{m s}^{-1}$; Table 4-1 – Model parameters). On average, a motor linked to the cytomatrix drives the microtubule in the direction of the local tangent, \mathbf{t} , to compensate for the displacement of the motor towards the minus end. Motion in the transverse direction is limited by the frictional resistance $\rho \gamma (\mathbf{1} - \mathbf{t} \mathbf{t}) \cdot \mathbf{v}$, where the motor friction $\gamma = \kappa / k_{off}$ is the quotient of the stiffness of the dynein linkage, κ , and the dynein dissociation rate, k_{off} .

The dynein friction coefficient was chosen by matching the times scales for individual microtubule motion found in simulations (see next section) with experimental data (e.g. Figure 4-3A and Figure 4-4). Further details of the determination of the motor friction are given in Appendix E – Simulations of microtubule buckling. The value of γ that best matches the experimental time scales ($\gamma = 10^3 \text{pN } \mu\text{m}^{-1} \text{s}$) can be obtained by taking the stiffness of the dynein linkage in the range $\kappa \sim 0.1\text{--}1\text{pN nm}^{-1}$ (52), and the dissociation rate $k_{off} \sim 0.1\text{--}1\text{s}^{-1}$. Our estimate of the dynein dissociation rate is consistent with observations of long-lived binding between dynein and microtubules (115) and with measurements of dynein exchange rates by photobleaching (145). The timescales for microtubule motion are insensitive to the choice of dynein density, since individual motors contribute equally to the force and the friction.

Simulations of Microtubule Buckling Dynamics

We next investigated whether dynein-mediated forces can explain the buckling of severed microtubules. Approximating the microtubule as an elastic slender body, the force and torque balances on the microtubule (146) are

$$\frac{d\mathbf{F}}{ds} + \mathbf{K} = 0, \quad \frac{d\mathbf{M}}{ds} + \mathbf{t} \times \mathbf{F} = 0 \quad (4-2)$$

where $\mathbf{F}(s)$ and $\mathbf{M}(s)$ are the force and bending moment at contour position s . The motor force is given by Equation 4-1 and the bending moment by $\mathbf{M} = B\mathbf{t} \times d\mathbf{t}/ds$, where B is the flexural rigidity. Representing the microtubule as discrete segments (Appendix E – Simulation methods) and solving for the velocity at each point along the contour length we can track the motion of a motor-driven microtubule of a constant length. Our model for dynein force generation envisages a number of motors distributed uniformly along the microtubule. For clarity and simplicity we have replaced a number of individual motors with a uniform (tangential) force and friction along the microtubule, which follows from a time (or ensemble) average over the positions of the individual motors.

Simulations based on this model explain how dynein can increase the curvature of a newly created minus end. As illustrated in the example in Figure 4-8B, following severing, small initial bends in the microtubule are predicted to be amplified due to the pulling forces generated by the dynein motors along the microtubule length. In addition, this buckling of the newly created minus-ended segment is predicted to occur on time scales comparable to the experimental observations (Figure 4-3A and Figure 4-1).

Centrosome Centering by Motor-Driven Microtubules

The experimental and theoretical evidence presented here is consistent with the hypothesis that microtubules in living cells are pulled by dynein motors distributed along their length (80, 82, 147). We experimentally determined whether dynein-dependent forces are essential for centering the centrosome in endothelial cells. To do this, cells were patterned into square shapes using microcontact printing, and the position of the centrosome was determined by imaging EGFP- α -tubulin expressing cells. The centrosome was observed to be at or close to the center in normal cells, while it was substantially off-center in dynein-inhibited cells (Figure 4-9A). Data from 22 different cells consistently show that the centrosome is off center in dynein-inhibited cells (Figure 4-9B). These results support the hypothesis that dynein is necessary for centrosome centering and are therefore consistent with a pulling mechanism (78, 80, 82, 147).

Simulations of centrosome centering allowed us to compare the dynamics of an array of microtubules with and without dynein forces. Microtubules were randomly nucleated at the centrosome and allowed to grow and disassemble by dynamic instability. We account for growth and shrinkage under dynamic instability (148) using the experimentally measured parameters for the polymerization velocity, $v_{pol} = 0.1 \mu\text{m s}^{-1}$, and depolymerization velocity $v_{depol} = 0.3 \mu\text{m s}^{-1}$, as well as the rates for switching to catastrophe, $k_{cat} = 0.05\text{s}^{-1}$, and rescue, $k_{rec} = 0.2\text{s}^{-1}$ (116, 117). More details of the simulation methods are available in Appendix E – Simulation methods.

One important experimental observation is that although microtubules in living cells are frequently observed to pin and buckle at the cell periphery, they sometimes continue to grow by sliding along the cell boundary (Figure 4-10). We incorporated both

possibilities into a stochastic model of contact between the tip of a microtubule and the cell boundary, which was able to capture the main features of the pinning and sliding (Appendix E – Simulation methods).

Figure 4-9C shows configurations of motor-driven microtubules in a 40 μm square cell. Some of the microtubules near the periphery buckle into small wavelength (see Figure 4-9C, $t = 1\text{min}$), consistent with experimental observations (73). The short wavelength buckles may not be immediately obvious in (Figure 4-9C) because the eye is naturally drawn to the longer wavelengths in the body of the cell. Nevertheless an examination of the border regions, particularly near the corners, shows that the motor-driven microtubules have short wavelength (2-3 μm) buckles (Figure 4-9C) whereas without motors there are only long-wavelength ($> 10 \mu\text{m}$) buckles (Figure 4-9D).

Motor-driven microtubules are predicted to drive an off-center centrosome towards the center with a time constant of the order of 10 min (Figure 4-11), similar to the time constant measured in living cells (Appendix E – Simulations of centrosome centering). Simulations also show that in the absence of motors (Figure 4-9D) the centrosome remains essentially fixed in place for at least 100 minutes (the duration of the simulation). This is consistent with experimental observations in dynein-inhibited cells (Figure 4-9B) where the centrosome remains off center.

To determine which forces are most important for centrosome centering, we formulated a simplified model assuming that the microtubules are rigid (Appendix E – Centrosome relaxation time). The predicted time scale for centering ($\sim 24\text{ min}$) remains comparable to experimental observations. Because the model only includes dynein tension and friction, the time scale is predicted to be independent of the number of

microtubules and the density of active dynein motors along the microtubules. Therefore, a balance of tensile and frictional forces from the dynein motors is sufficient to explain centrosome centering on timescales comparable to experimental observations.

Pushing forces have been observed to cause centering *in vitro* (77), but not under physiological conditions. In particular, the viscosity of the buffer solution in these experiments was much smaller than the effective viscosity of the cellular fluid, as inferred from the cutting experiments described earlier (Figure 4-3). In addition the fabricated cells were smaller (12 μm) than the endothelial cells used in our *in vivo* experiments (~ 40 μm). To see if we could resolve these apparent contradictions, we simulated the conditions described in (77); a square cell of length (12 μm), a low viscosity background fluid (water), and microtubules that were allowed to slip along the cell surface to mimic the smoothness of the glass walls. In addition, we adjusted the polymerization kinetics to allow for different steady-state lengths of microtubules. Our simulations showed the same behavior as the experiments; with short microtubules, an initially off-center centrosome moved towards the cell center. In the small chamber, shorter microtubules generate a larger buckling force than the longer microtubules in the living cells (roughly 10-fold, since buckling forces scale with L^2). This, combined with the lower viscous drag of the fluid, is sufficient for the centrosome to center. However if the polymerization kinetics were adjusted to create longer microtubules, then the centrosome drifts off center, as observed experimentally (77). Thus our simulations explain a number of apparently contradictory experimental observations in terms of the relative magnitudes of compressive, tensile and frictional forces. A CENTROSOME can be centered by pushing forces under conditions where microtubules are short and the

viscosity of the fluid is similar to water, but not in animal cells where the microtubules are longer and the friction is orders of magnitude larger. However, tensile motor forces can center the centrosome in capillary endothelial cells on the experimentally observed timescale. Further details can be found in Appendix E – Simulation of centrosome centering.

Discussion

The results of our investigation give new insight into the role of dynein in the force balance on microtubules. If individual microtubules were under compressive stress along their length, severing would result in a straightening of the microtubule, but we observed that the curvature generally increased near a newly-created minus end. Conversely, when dynein activity was inhibited, microtubules straightened after severing. Severed plus-end segments in normal cells are observed to depolymerize along the original contour. Simulations suggest that microtubules pinned at their minus end do eventually straighten, but the timescale for the motors to push buckles towards the free plus end (~ 10 s) is significantly longer than the depolymerization time. These observations are consistent with dynein motor forces pulling the microtubule segments towards the cell periphery. The fact that severed microtubules in normal cells are never observed to straighten indicates that dynein contributes a large frictional resistance to lateral motion in addition to its directional force; this is confirmed by the rapid straightening of severed microtubules in dynein-inhibited cells.

We have developed a model for dynein force generation to explain the directional and frictional forces suggested by the experimental observations summarized in the previous paragraph. In this model, frictional forces arise from the binding and dissociation of dynein motors linking microtubules to the cytomatrix, while the tangential

forces come from the motor activity of cytomatrix-bound dynein. The model makes several qualitative and quantitative predictions about the nature of the force balance on the microtubule. If a microtubule is pinned at its minus end at the centrosome, pulling forces from the dynein motors lead to a tensile stress along its length, with the maximum tension at the minus end (centrosome). If the microtubule has not reached the cell periphery, the stress at the free plus end must vanish. However when its tip impinges on the cell periphery, a compressive force develops to accommodate the excess length of the polymerizing microtubule. The microtubule is then in a state of compression near the tip but in tension near the centrosome; the balance of forces is taken up by cytoskeletal-bound dynein. The model predicts that the dynein pulling force balances the tip compressive force at a distance $d = F_p / \rho f_0$ (neglecting bending forces relative to dynein forces) from the tip, where F_p is the compressive force at the tip, and $\rho f_0 \sim 16$ pN/ μm is the dynein force per unit length. The polymerization force is unknown *in vivo* but *in vitro* it has been estimated to be ~ 10 pN, (149), for which $d = 0.6$ μm using our estimate of ρf_0 . Even for larger polymerization forces of tens of pN, the compressive force can be balanced by only a few motors near the microtubule tip and the transition from tension to compression is predicted to occur within just a few microns. Therefore a key prediction of the model is that most of the microtubule is under tension despite large compressive forces at the tip. This would explain the experimentally observed increase in curvature of the minus end upon severing indicating tension independent of distance from the periphery

The model also helps explain what happens upon severing. Once the tension is released at the cut point, the small longitudinal extension quickly relaxes, and the force

generated from dynein motors along the segment near the newly created minus end quickly becomes compressive. This compressive force causes this segment to increase in curvature (i.e. buckle). The model predicts an increase in curvature for minus-ended segments even when the plus-end is not impinging on the cell boundary. This is due to the large translational resistance from protein friction, which effectively immobilizes the microtubule segments far from the cut point.

Simulations predict that dynein motors pulling on a radial array of microtubules can center the centrosome *in vivo*, consistent with our observation that the centrosome is off-center in dynein inhibited cells. Moreover, the time scale for centrosome centering, calculated with the same motor parameters as in the buckling simulations, is consistent with experimental measurements. Our model predicts that the centering time is insensitive to microtubule number and dynein density. Our simulations also explain why centering by microtubule pushing can occur *in vitro* without dynein (77), but only under conditions (low friction and short microtubules) where buckling does not occur. Fission yeast, for example, appears to present conditions that favor pulling during meiotic prophase but pushing during interphase, by varying the cortical localization of dynein (149-154). However, under conditions found in animal cells, with longer microtubules and much higher frictional resistance, both simulations and experiments suggest that compressive buckling forces are insufficient to center the centrosome. In consistence with the results discussed above, the same laser ablation experiment done with microtubules in U2OS (human osteosarcoma) also showed the same phenomenon (Figure 4-12). Thus, our model for dynein motor forces quantitatively ties the mechanics and dynamics of individual microtubules to the centering mechanism of the centrosome.

Although our results show that dynein is the dominant contributor to the lateral friction and that dynein forces are sufficient to buckle freed minus ends, we do not exclude the possibility of other motors playing a role in microtubule force generation. For example, it is possible that plus-end directed kinesin motors are simultaneously pulling in a direction opposite to the dynein forces. If this force is significant relative to dynein pulling, then the density of dynein linkages would be larger than our current estimate, but the qualitative predictions of the model would be unchanged.

Our findings have several important implications for the role of microtubules in cell mechanics. A microtubule in a living cell cannot be described by a static force balance, because of the significant contribution of frictional forces from moving segments. The tangential and frictional forces generated by dynein motors dominate the elastic stresses from microtubule bending and cytomatrix deformation. Although numerical results indicate that a typical microtubule is under tension along most of its length, we do not rule out a compressive force at a microtubule tip impinging on the cell periphery. Dynein motors may in fact confine the compressive stresses to the region near the tip, consistent with a picture in which microtubule compressive forces at the periphery are transmitted to the actin cytoskeleton (83), but through transient dynein-cytomatrix linkages rather than by elastic deformation (73). Our model for dynein force generation provides a unifying explanation for the shapes of individual microtubules in the cell and how these shapes are consistent with tension-driven centering of the centrosome by a radial array of microtubules.

Summary of Findings

By using femtosecond laser ablation, we severed bent single microtubules in living cells. The behavior of buckled microtubule after severing gave us a direct readout of

forces on microtubules. Dynein was found to pull microtubules towards the plus end. A model for dynein force generation was proposed, and simulations of centrosome centering were conducted using the model. Our model for dynein force generation provides a unifying explanation for the shapes of individual microtubules in the cell and how these shapes are consistent with tension-driven centering of the centrosome by a radial array of microtubules.

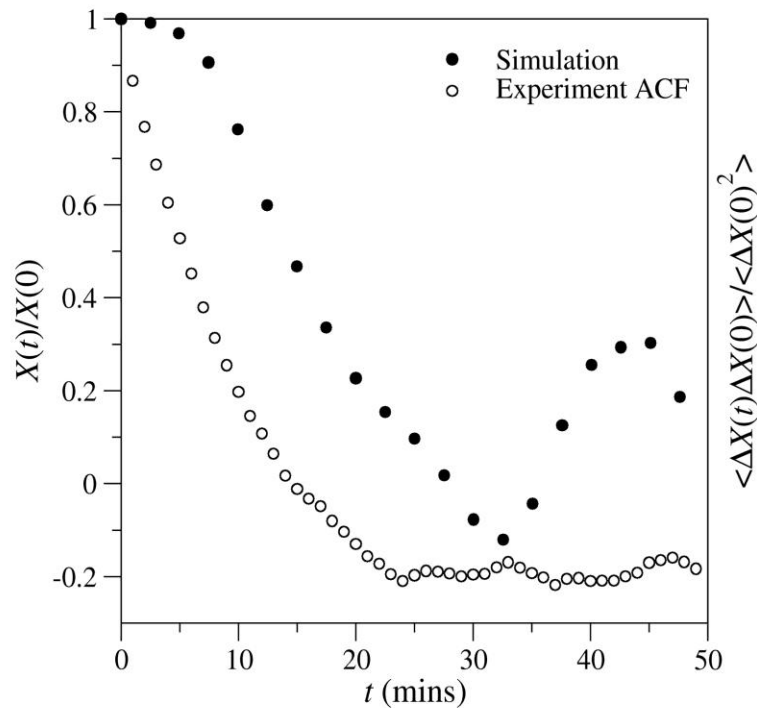


Figure 4-1. A comparison of centrosome centering (simulation) with the autocorrelation function of fluctuations in centrosome position (experiment). The microtubule network develops during the first 5 min of the simulation; subsequently the centrosome centers with a relaxation time of 12 min. Experimental measurements of the autocorrelation function of the centrosome position decay in about 8 min. The negative region in the autocorrelation function reflects insufficient data to obtain an accurate measurement of the mean position in each cell.

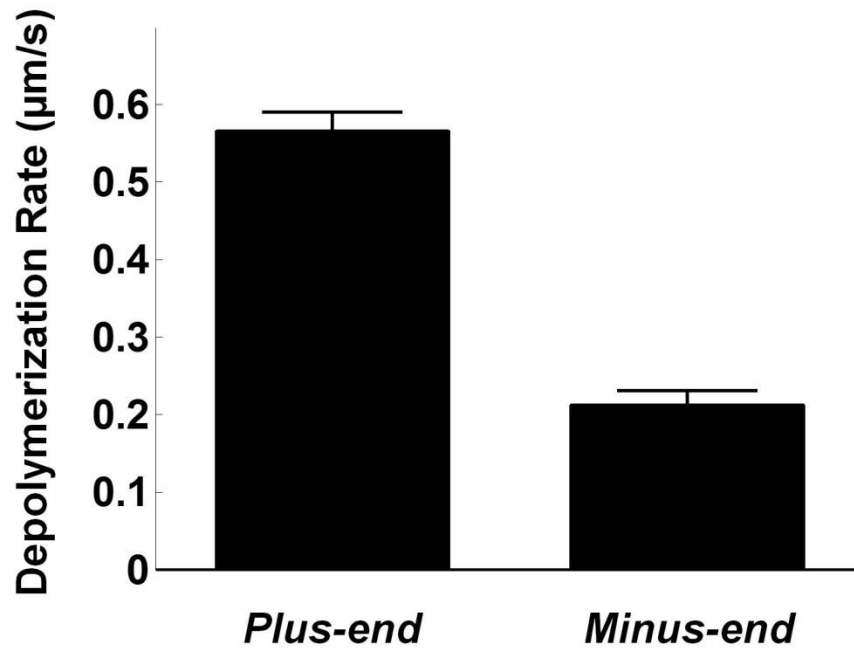


Figure 4-2. Depolymerization rates of microtubules severed by laser ablation. The bar graphs show that depolymerization rate of the plus-end is consistently larger than that of the minus-end.

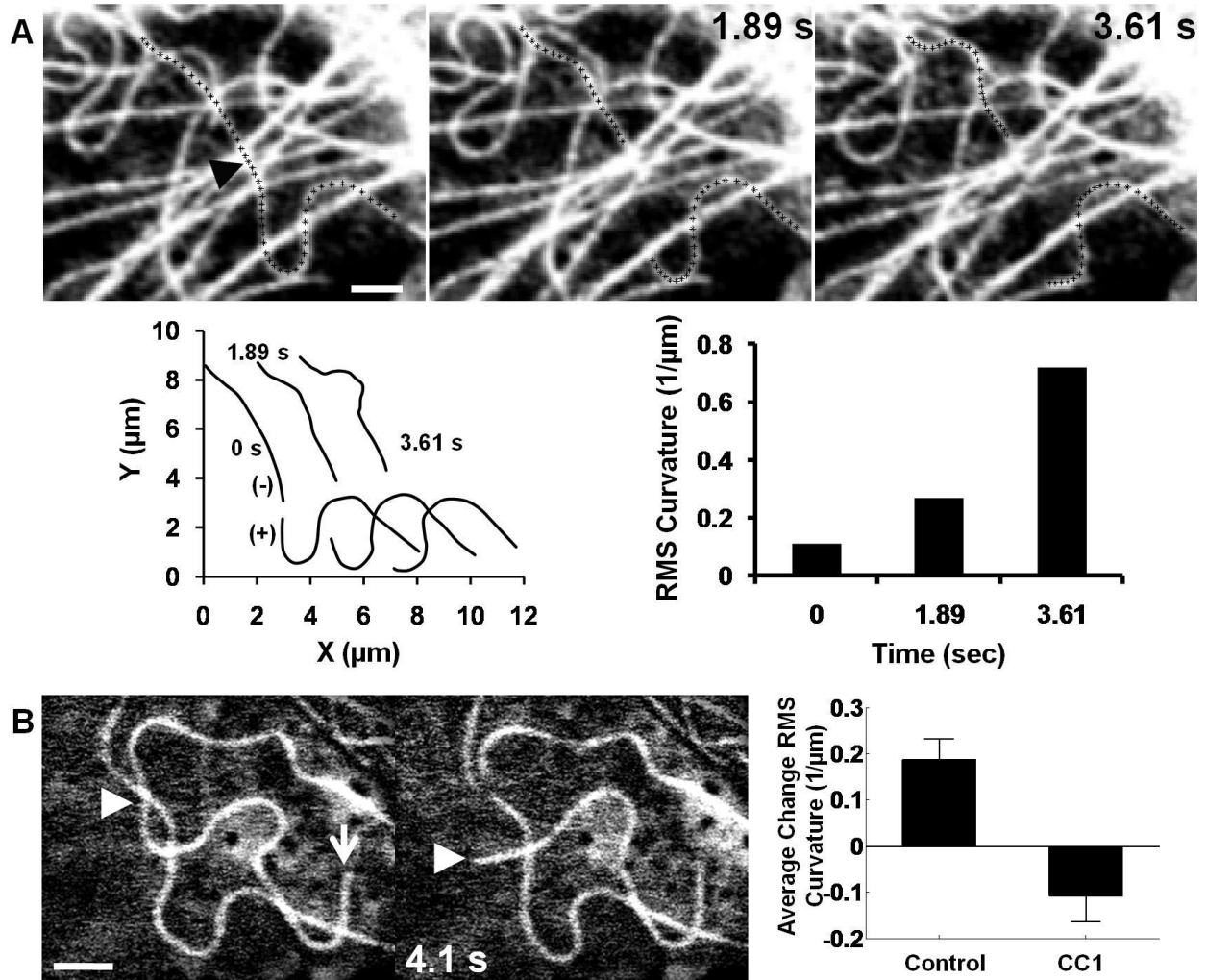


Figure 4-3. Minus end microtubules underneath the nucleus increase in bending after laser severing. Representative images highlighting changes in shape after severing a single microtubule in living cells. (A) Increased bending of minus ended microtubules after severing near the nucleus. The black arrowhead indicates the position of the cut and the severed microtubule is highlighted by small crosses. Microtubule shapes in the images were measured in MATLAB (see plots of severed microtubule shapes; the newly created plus and minus ends are indicated) and the root mean square (RMS) curvature was calculated. The minus-end microtubule (recognized as minus ended from the lack of significant depolymerization compared to the newly exposed plus end) showed a 7-fold increase in mean curvature over the visible segment length. However, the plus-end segment depolymerized but showed no measurable change in curvature. These observations are consistent with the hypothesis of minus-end directed motors pulling on the microtubule. (B) Straightening of a bent microtubule in a dynein-inhibited cell. The white arrow indicates the plus end of the microtubule, and the arrowhead tracks the severed end. The microtubule straightens significantly on timescales of a few seconds,

supporting the hypothesis that there is an additional frictional force contributed by dynein. The plot compares the change in RMS curvature near severed minus ends in control and dynein-inhibited cells. Data is from at least 10 cells for each condition; the statistical significance is at $p < 0.01$. Error bars indicate standard error of the mean (SEM). The pooled data strongly supports the hypothesis that dynein promotes bending of microtubules in living cells, and that in the absence of dynein, microtubules straighten upon severing. Scale bars are 2 μm .

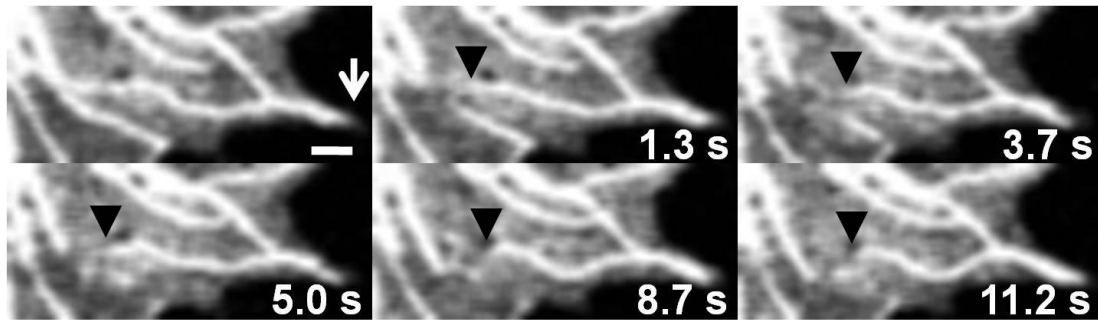


Figure 4-4. Minus-end microtubules at the cell periphery increase in bending after laser severing. A representative example of experiments where a single microtubule, near the cell periphery (white arrow), was severed. Images show increased bending of minus-ended microtubules after severing (cut at black arrow). The plus-end depolymerized at a rate of $0.607 \mu\text{m/s}$, while the minus-end depolymerized at a rate of $0.164 \mu\text{m/s}$. Note that the plus end depolymerizes but does not show a change in curvature. Scale bar is $1 \mu\text{m}$.

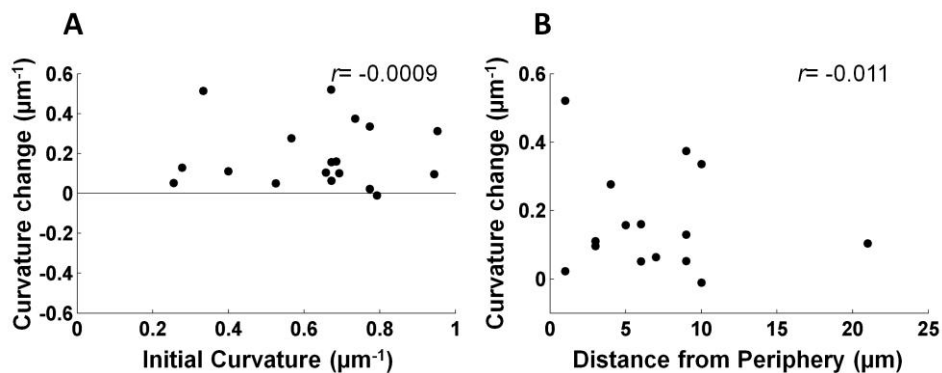


Figure 4-5. Change in curvature after severing is not correlated with the initial curvature, nor with the spatial location of the cut. (A) The maximum change in RMS curvature for 18 experiments is plotted against the initial curvature. In all experiments that were analyzed, the change in curvature was positive and no correlation with initial curvature was found. (B) The maximum change in RMS curvature is plotted against the shortest distance from the cut to the cell periphery. No significant correlation was observed suggesting that the increase in curvature is not location dependent. In three cells the cuts were positioned under the nucleus and the distance to the periphery could not be determined. r is correlation coefficient.

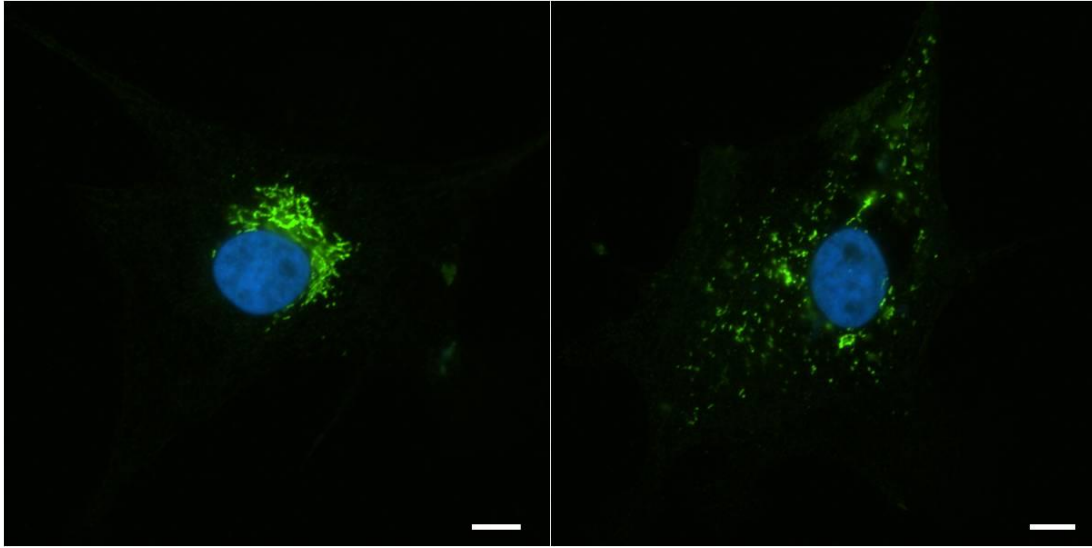


Figure 4-6. Inhibition of dynein causes dispersion of the Golgi complex. BCE cells were transfected with DsRed-CC1 to inhibit dynein. The cells were then fixed and immunostained with mouse monoclonal Golgi marker (Abcam) and Hoechst 33342. Control cells (left) show a compact Golgi complex (green) near the nucleus (blue), while DsRed-CC1 transfected cells (right) show a dispersed Golgi complex. Scale bars are 10µm.

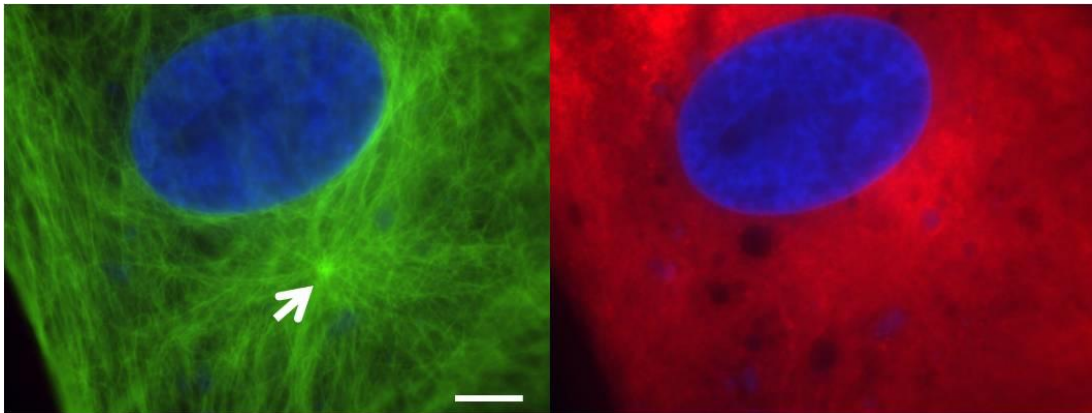


Figure 4-7. Microtubules radiate from the centrosome in dynein inhibited cells. BCE cells were transfected with DsRed-CC1 and infected with adenoviral GFP-tubulin, and fixed and immunostained with Hoechst 33342 (blue, nucleus). Clear microtubules emanate from the centrosome. Scale bar is 10µm.

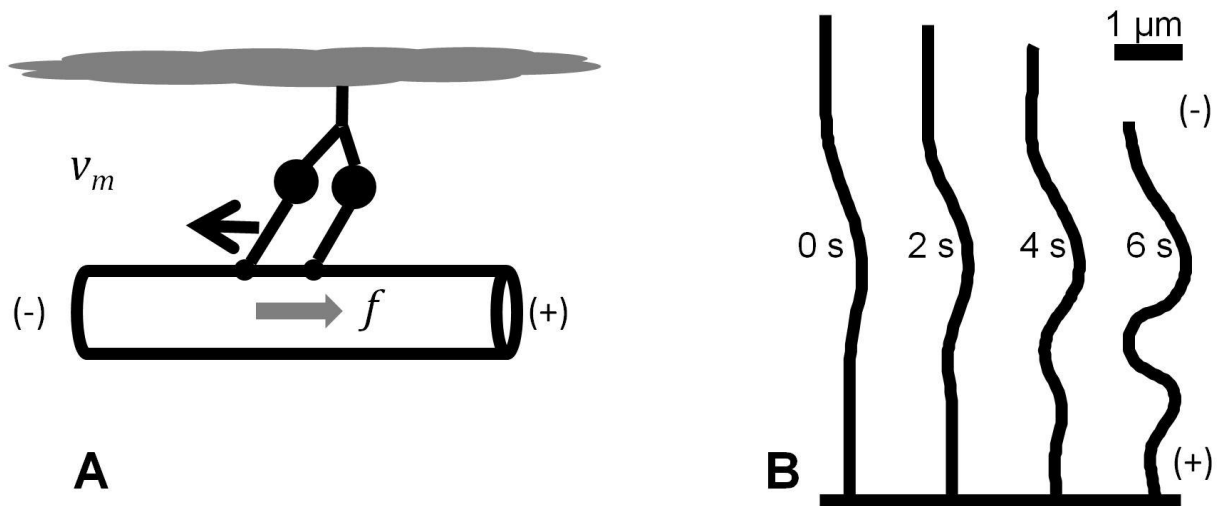


Figure 4-8. Simulations predict dynein-induced buckling of microtubules. (A) Cartoon of a dynein motor indicating how the minus-directed motor bound to the cytomatrix exerts a force towards the microtubule plus end. (B) Simulations of an elastic filament based on the force balance in Equation 4-1 and 4-2 predict dynein-induced buckling near the minus end of a severed microtubule. The timescale can be compared with the experimental data in Figure 4-3A.

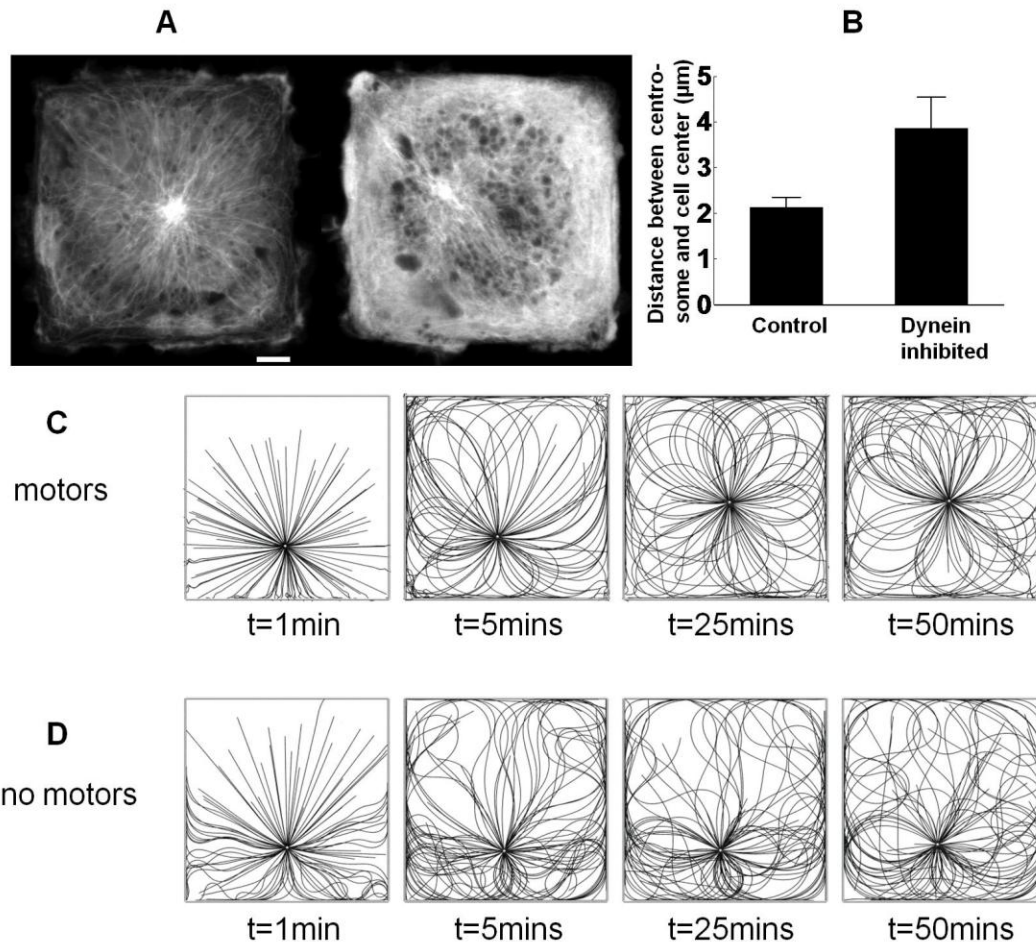


Figure 4-9. Dynein forces are sufficient to center the centrosome. (A) Representative images showing the centrosome in EGFP- α -tubulin expressing square endothelial cells; control cell (left) and dynein-inhibited cell transfected with DsRed-CC1 (right). Scale bar is 5 μm . (B) Mean centrosome position in 42 control cells and 22 dynein inhibited cells; the statistical significance $p < 0.01$. Error bars indicate SEM. The centrosome is consistently observed to be at or close to the center of the square in control cells, while it is substantially off-center in dynein-inhibited cells. Simulations of centrosome centering in square cells with (C) and without (D) dynein motor activity. The motor-driven microtubules (C) show considerable buckling near the cell periphery (clearly visible at $t = 1$ min) whereas without motor activity (D) the buckling is of Euler type. Only the motor-driven microtubules are observed to center an initially off-center centrosome.

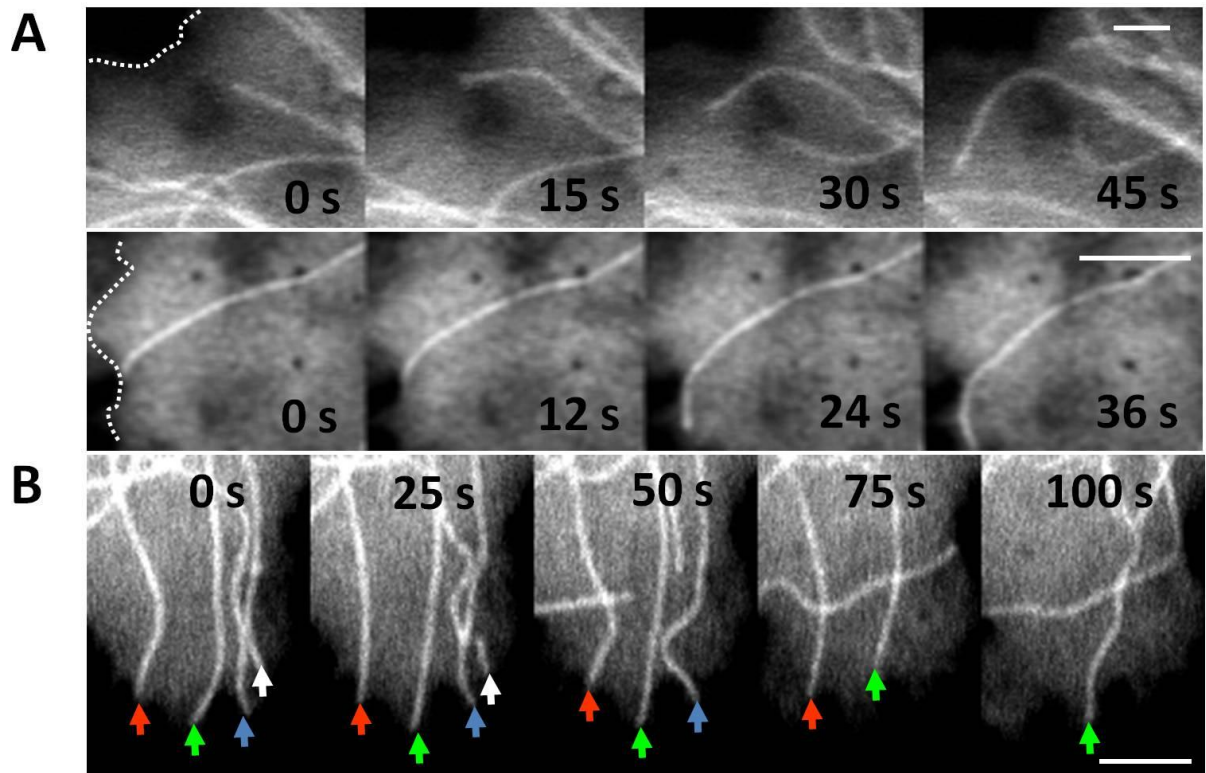


Figure 4-10. Microtubules undergo three distinct behaviors upon reaching the periphery: (1) buckling with the tip immobilized; (2) sliding along the cell periphery; (3) no growth, eventually depolymerizing. (A) Two examples of microtubules that slide along the cell periphery (dotted white line). (B) Four microtubules (colored arrows) that have reached the cell periphery and remain until they depolymerize. One microtubule (green) does not buckle significantly, suggesting that it has stopped growing. Scale bars are 2.5 μm .

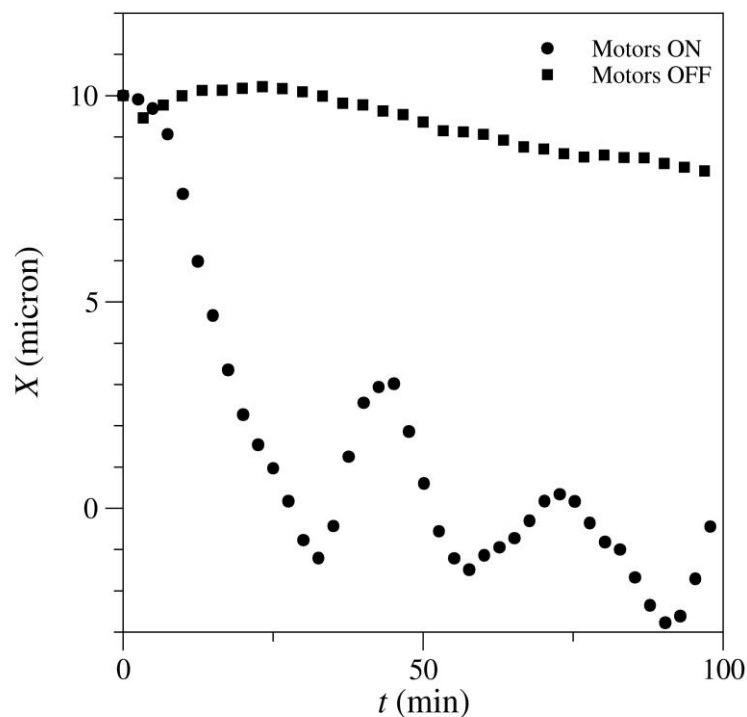


Figure 4-11. Simulations of centrosome centering. The circles show simulated displacements of the centrosome, $X(t)$, which centers on a time scale of the order of 10 mins and thereafter oscillates about the central position. The squares show the same initial condition but with the motor forces and friction turned off. Here the microtubules experience a much reduced (100 fold) drag force from the cellular cytoplasm (as inferred from the laser severing experiments in dynein inhibited cells) but the polymerization forces are unable to push the centrosome towards the center on experimentally relevant timescales.

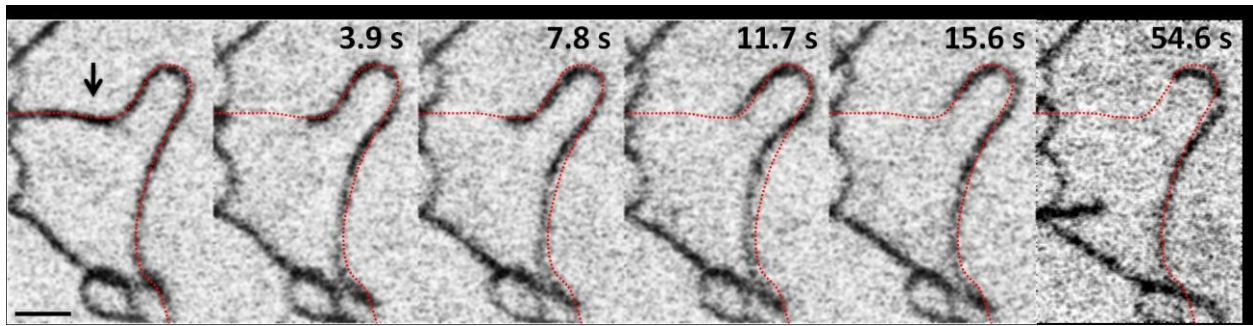


Figure 4-12. Minus-end microtubules underneath the nucleus does not straighten after laser severing. U2OS cells expressing RFP-tubulin was used. A representative example of experiments where a single microtubule underneath the nucleus was severed. Images show no straightening as the minus-ended microtubules after severing slowly depolymerized (cut at black arrow). Scale bar is 2 μm

Table 4-1. Microtubule Mechanics and Centrosome Centering Model Parameters

Symbol	Parameter	Range	Source	Value Used
f_{max}	Maximum dynein force	5-8 pN	(115)	8 pN
v_0	Dynein speed (no force)	$0.8 \mu\text{m s}^{-1}$	(109)	$0.8 \mu\text{m s}^{-1}$
κ	Dynein spring constant	$0.1\text{-}1 \text{ pN nm}^{-1}$	(52, 155)	1 pN nm^{-1}
k_{off}	Dynein-nucleus off-rate	No value	Filament buckling	1 s^{-1}
ρ	Dynein density (#/length)	No value	Filament buckling	$2 \mu\text{m}^{-1}$
N	Number of microtubules	200-500	(116)	100
v_{pol}	MT polymerization speed	$0.1\text{-}0.2 \mu\text{m s}^{-1}$	(116, 117)	$0.1 \mu\text{m s}^{-1}$
v_{depol}	Depolymerization speed	$0.2\text{-}0.3 \mu\text{m s}^{-1}$	(116, 117)	$0.3 \mu\text{m s}^{-1}$
k_{cat}	Catastrophe rate constant	$0.01\text{-}0.06 \text{ s}^{-1}$	(116, 117)	0.05 s^{-1}
k_{rec}	Recovery rate constant	$0.04\text{-}0.2 \text{ s}^{-1}$	(116, 117)	0.2 s^{-1}
ξ	Effective friction		Filament relaxation	10 Pa s

CHAPTER 5 MODELING OF FLUORESCENCE RECOVERY AFTER PHOTBLEACHING

The analysis of Fluorescence Recovery After Photobleaching (FRAP) experiments requires mathematical modeling of the fluorescence recovery process. An important issue of FRAP experiments that tends to be ignored in the modeling is that there can be a significant loss of fluorescence due to bleaching during image capture. In this chapter, we explicitly include the effects of bleaching during image capture in the model for the recovery process, instead of correcting for the effects of bleaching using reference measurements. Using experimental examples, we demonstrate the usefulness of such an approach in FRAP analysis. The models discussed here can help bring great clarity into the interpretation of FRAP experiments.

Materials and Methods

Cell Culture, Plasmids and Transfection

NIH 3T3 fibroblasts were cultured in DMEM (Mediatech, Manassas, VA) with 10% donor bovine serum (Gibco, Grand Island, NY). For microscopy, cells were cultured on glass-bottomed dishes (WPI, Sarasota, FL) coated with 5 μ g/ml fibronectin (BD BiocoatTM, Franklin Lakes, NJ) at 4°C overnight.

EGFP-VASP was used in transfect cells. Transient transfection of plasmids into NIH 3T3 fibroblasts was performed with LipofactamineTM 2000 transfection reagent (Life Technologies, Invitrogen, Carlsbad, CA).

Confocal Microscopy and FRAP

Cells expressing EGFP-VASP was imaged on a Leica SP5 DM6000 confocal microscope equipped with a 63X oil immersion objective. FRAP analysis was carried out by selecting the focal adhesion using the ROI (region of interests) function. A 488

nm Argon laser was applied at 50% power to bleach the focal adhesion for five times. All images were taken at 512X512 resolution with approximately four times zoom in. For calculating immobile fraction, three images were taken after the bleaching using 4% laser power, the time interval was 40 seconds (80 seconds total). For FRAP without free protein bleaching effects, images were taken every 1.3 seconds (minimum intervals) for 60 frames using 4% laser power. For FRAP with free protein bleaching effects, images were taken every 1.3 seconds using 20% laser power. During microscopy, cells were maintained at 37 °C in a temperature, CO₂ and humidity controlled environmental chamber.

Results

Modeling Bleaching During Image Capture.

We first consider the situation where fluorescence imaging is performed on a live cell. If an image is captured for an exposure time ω , then the fluorescence concentration in the cell will decrease from an initial value of $C(t = 0) = C_0$ in this time according to the kinetic expression(156, 157)

$$\frac{dC}{dt} = -\lambda C \quad (5-1)$$

where λ is the photobleaching rate constant (s^{-1}). The precise value of λ will depend on imaging conditions (i.e. laser power, magnification, exposure time etc). At the end of the exposure time ω , the concentration is $C(\omega) = C_0 e^{-\lambda\omega}$. Consider an experiment involving imaging of the entire cell over n frames with a time interval between frames of τ . The i^{th} image capture is assumed to occur in the time interval $(i\tau - \omega, i\tau)$. Then applying

Equation 5-1 for imaging at each frame, the formula for the concentration at the end of the i^{th} time interval is

$$C_i = C_0(e^{-\lambda\omega})^i = C_0g^i \quad (5-2)$$

where $g \equiv g(\omega, \lambda) = e^{-\lambda\omega}$.

The time evolution of the concentration predicted by equation (2) for a hypothetical experiment is shown in Figure 5-1A. Because the imaging occurs over a time interval ω , the measured fluorescence in the i^{th} image is proportional not to C_i but rather to the average concentration over ω given by $C_i f$, where $f \equiv f(\omega, \lambda) = \frac{e^{\lambda\omega} - 1}{\lambda\omega}$ (the measured fluorescence). However, as is common practice, the fluorescence in subsequent images is normalized to the fluorescence in the first image ($i = 1$) and so the factor f cancels, making the *normalized* fluorescence proportional to the ratio of concentrations $\frac{C_i}{C_1}$.

Figure 5-1B illustrates how normalization scales the hypothetical data from Figure 5-1A. Noting this requirement for normalization, the normalized fluorescence in a whole-cell imaging experiment obeys the equation

$$\ln \frac{C_i}{C_1} = -(i-1)\lambda\omega, \quad i = 2, 3, \dots, n \quad (5-3)$$

Equation 5-3 allows the straightforward estimation of λ (assuming ω is known). Alternatively one could capture one frame for a long enough ω causing significant bleaching due to image capture; this suffers from potential heating artifacts though and may not be as reliable as the procedure suggested by Equation 5-3.

FRAP Model to Account for Photobleaching due to Image Capture

When the FRAP experiment involves the selective photobleaching of bound molecules (such as molecules bound to a microtubule tip(158), or in a focal adhesion(133, 159, 160), or at a promoter array(91, 161)) the recovery occurs through diffusive transport of free protein molecules (in the cytoplasm, nucleoplasm or membrane) followed by exchange with bound molecules. A commonly encountered situation is where the exchange between bound and free protein is far slower than diffusive transport into the photobleached spot and the concentration of the free protein is unaffected by the exchange process owing to the large pool of free molecules compared to bound molecules(160, 162). In the following discussion, we developed the modeling approach for this situation (the approach is generally applicable as discussed later).

We consider first the situation where bleaching during image capture is not significant. The equation describing the recovery process is (assuming the free concentration is well-mixed and constant, and that diffusion is very fast compared to binding)

$$\frac{d\hat{C}}{dt} = k_{ON}SC - k_{OFF}\hat{C} ; \hat{C}(t=0) = \alpha\hat{C}_0 \quad (5-4)$$

Where k_{ON} is the rate constant for binding, S is the binding site concentration, C is the cytoplasmic (or membranous) diffusing concentration and \hat{C} is the bound concentration in the photobleached spot. The initial condition reflects the fact that the photobleaching pulse reduces bound fluorescence from an initial concentration of \hat{C}_0 to $\alpha\hat{C}_0$ ($\alpha < 1$).

The solution to this equation is

$$\frac{\hat{C}}{\hat{C}_0} = 1 - (1 - \alpha)e^{-tk_{OFF}} \quad (5-5)$$

The typical approach in the literature is to normalize the experimental data as

$$\frac{F(t) - F(0)}{F(t \rightarrow \infty) - F(0)} \text{ and then fit it to } \frac{\hat{C}(t) - \alpha\hat{C}_1}{\hat{C}_\infty - \alpha\hat{C}_1} = 1 - e^{-tk_{OFF}}.$$

The parameter estimated from the data is k_{OFF} .

However, if there is bleaching during the image capture process itself, then as illustrated in Figure 5-1C, the dotted lines are the actual dynamics consisting of (unobserved) recovery interspersed by bleaching during image capture leading to the measured recovery (indicated by the (*)). It is necessary then to model the unobserved dynamics, consisting of recovery between time intervals of image capture and also the bleaching due to the image capture process itself to predict the observed recovery dynamics. Fitting such a model to the data has the advantage of faithfully capturing the recovery process, and eliminating the need for arbitrary corrections to the data (such as correcting the recovery signal by dividing with the total cell intensity which decays due to bleaching during image capture).

We now consider the time-evolution of the fluorescent bound concentration under the effects of bleaching due to image capture. Consider three images: one taken just before the photobleaching pulse corresponding to a final concentration of \hat{C}_1 ('final' refers to the fluorescent bound molecule concentration at the end of the image capture), the second image immediately after the photobleaching pulse corresponding to a final concentration of $\alpha\hat{C}_1$ and the third image whose capture begins at a time interval of $\tau - \omega$ where τ is the time interval between successive images (similar to the logic used

in the whole cell experiment before). The fluorescent bound concentration just before the third image capture begins is $\hat{C}(\tau - \omega)$. Because $\omega \ll \tau$ ($\omega \sim$ milliseconds and $\tau \sim$ second), we can approximate $\tau - \omega \sim \tau$ in Eq. 5 yielding $\hat{C}(\tau - \omega) = \hat{C}_1 - \hat{C}_1(1 - \alpha)e^{-tk_{OFF}}$. When imaging starts, photobleaching occurs due to image capture, and the concentration at $t = \tau$ is $\hat{C}(\tau) = g\hat{C}_1(1 - (1 - \alpha)e^{-tk_{OFF}})$; $g \equiv g(\omega, \lambda) = e^{-\lambda\omega}$ as before. Here we have made the assumption that the recovery itself occurs to a negligible extent in the time interval ω compared to fluorescence decay due to bleaching during image capture. This is reasonable considering that $\omega \ll \tau$, and the recovery time scale is much larger than τ .

The exchange process in the next time interval $(\tau, 2\tau - \omega)$ is still described by the differential equation in Equation. 5 but now with an initial condition $\hat{C}(\tau)$. Extending this logic to the i^{th} frame, it is possible to calculate the concentration \hat{C}_i at the end of the i^{th} image capture as shown below (we note again that $i = 1$ indicates the concentration at the end of image capture just before the photobleaching pulse, $i = 2$ indicates the concentration at the end of image capture just after the photobleaching pulse):

$$\begin{aligned} \frac{\hat{C}_2}{\hat{C}_1} &= \alpha \\ \frac{\hat{C}_i}{\hat{C}_1} &= g \left(1 - \left(1 - \frac{\hat{C}_{i-1}}{\hat{C}_1} \right) e^{-tk_{OFF}} \right) \text{ for } i = 3, 4, \dots, n \end{aligned} \tag{5-6}$$

The concentrations are all normalized to the concentration at the end of the image capture just before the photobleaching pulse. As before, the ratio of the measured fluorescence in the i^{th} image to the fluorescence in the first image is proportional to (and should be fit to) the concentration ratio derived in Equation 6.

An interesting point here is that the model predicts a steady state for the fluorescence recovery despite the fact that image capture results in periodic bleaching. Such a steady state will be reached when the fluorescence lost due to bleaching due to image capture is exactly balanced by recovery in between time frames. This yields the equality (N represents any image collected in the steady state portion of the recovery curve)

$$k_{OFF} = -\frac{1}{\tau} \ln \frac{-\frac{C_N}{C_1} + g}{\left(1 - \frac{C_N}{C_1}\right)g} \quad (5-7)$$

At steady state, if the fluorescence intensity is known, and the bleaching function g determined from experiment, it is possible to calculate k_{OFF} using Equation 5-7. This of course requires prior knowledge of the model that describes protein exchange in the spot (in this case, Equation 5-4).

Accounting for Bleaching of Free Protein

Equation 5-6 describe FRAP recovery when photobleaching during image capture is significant. In deriving these equations, we have assumed that the free protein concentration C is unaltered by the bleaching. This assumption is typically valid if we consider that the bleaching during image capture occurs predominantly at the focal plane (where the laser beam is focused in a confocal microscope) and progressively less outside the bleached spot. As the space where the free molecules diffuse is well mixed on time scales of exchange with bound protein (this is the assumption underlying Equation 5-4), it is reasonable to expect that the free concentration of molecules will decrease much less due to image capture than proteins present in a bound spot enclosed in the thickness of the focal plane (such as a focal adhesion or a receptor

binding to a promoter array in the nucleus; this is discussed more in the APPENDIX E).

The assumption that the free protein is not changing in concentration due to image capture can also be checked by measuring the fluorescence of free molecules as demonstrated in the experimental example later.

When the free molecules are also bleached during image capture, we let g_1 and g_2 be the bleaching functions for bound and free proteins (corresponding to different 'effective' values of λ ; see the APPENDIX E). Then, the free concentration decreases similar to Equation 5-3

$$\ln \frac{\hat{C}_i}{\hat{C}_1} = (i-1) \ln(g_2) \quad (5-8)$$

We continue to make the assumption that the free concentration is well-mixed, and unaffected by the exchange process itself with bound protein because of the large pool of free molecules compared to bound molecules. Using Equation 5-8 with Equation 5-4 for the unobserved concentration between successive frames and accounting for bleaching, the bound concentration is

$$\begin{aligned} \frac{\hat{C}_2}{\hat{C}_1} &= \alpha \\ \frac{\hat{C}_i}{\hat{C}_1} &= \left(g_2^{i-1} - \left(g_2^{i-1} - \frac{\hat{C}_{i-1}}{\hat{C}_1} \right) e^{-k_{OFF}} \right) g_1 \text{ for } i = 3, 4, \dots, n \end{aligned} \quad (5-9)$$

FRAP Model to Account for an Immobile Fraction

As discussed above, assuming that the free protein pool is unaffected by the imaging process, the recovery should reach a steady state. This model, however, assumed that all of the molecules in the bleached spot were able to exchange with the cytoplasmic pool of molecules on a single time scale ($\sim 1/k_{OFF}$). In many experimental

situations, it is observed that the recovery is not complete, suggesting the presence of an ‘immobile’ fraction in the bleached spot. Then the full solution (including bleaching of the free pool) is (here β is the immobile fraction)

$$\frac{\hat{C}_2^M}{\hat{C}_1} = \alpha(1 - \beta) \quad (10A)$$

$$\frac{\hat{C}_i^M}{\hat{C}_1} = (1 - \beta) \left(g_2^{i-1} - \left(g_2^{i-1} - \frac{\hat{C}_{i-1}^M}{\hat{C}_1(1 - \beta)} \right) e^{-\tau k_{OFF}} \right) g_1 \text{ for } i = 3, 4, \dots, n$$

$$\frac{\hat{C}_2^{IM}}{\hat{C}_1} = \alpha\beta \quad (10B)$$

$$\frac{\hat{C}_i^{IM}}{\hat{C}_1} = \beta g_1 \left(\frac{\hat{C}_{i-1}^{IM}}{\hat{C}_1 \beta} \right) \text{ for } i = 3, 4, \dots, n$$

Here β is the immobile fraction. \hat{C}_1 is the total concentration ($= \hat{C}_1^M + \hat{C}_1^{IM}$), α still represents the fraction of fluorescent bound molecules bleached. The contribution of mobile and immobile pools to the recovery need to be separately accounted for as shown in Equation 10A and 10B (the superscript M refers to the mobile fraction, IM refers to the immobile fraction). The fluorescence intensity in a FRAP experiment normalized to the initial fluorescence just before the photobleaching pulse should be fit

$$\text{to } \frac{\hat{C}_i^M}{\hat{C}_1} + \frac{\hat{C}_i^{IM}}{\hat{C}_1}.$$

Calculations of Normalized Recovery: the Behavior of Equation 5-6A and 6B

We explored the behavior of Eq. 5-6A and 6B numerically. As seen from Equation 5-6, the recovery process depends on the parameter group τk_{OFF} , the parameter α , and the parameter group $\lambda\omega$. Fixing $\alpha = 0.4$ (a typical value for bleaching in experiments) and assuming $\lambda\omega = 0.2$, solutions to Equation 5-6 are plotted for different values of τk_{OFF} (Figure 5-2). Because ω is kept constant ($= \tau/10$), the value of τ can be thought of

as constant in Figure 5-2 (although its actual value is not relevant since the solution depends on the parameter group τk_{OFF}).

Figure 5-2 shows that when too many frames are collected over the characteristic time scale of the recovery process (i.e. $\tau \ll 1/k_{OFF}$), there is a significant decrease in net recovery owing to bleaching during image capture. This is because bleaching during image capture occurs too frequently such that significant recovery due to protein exchange between successive image captures does not occur resulting in a steady state with low recovery. The extent of recovery increases with increases τk_{OFF} . The photobleaching process during image capture itself can create an erroneous impression of an 'immobile' fraction. Also shown in Figure 5-2 is the 'observed' data superimposed with the 'unobserved' dynamics and the dynamics of bleaching.

Effect of the Immobile Fraction on FRAP Recovery Without Bleaching of Free Protein)

Figure 5-3A shows calculations of recovery in the presence of an immobile fraction. The parameter values are identical to Figure 5-2, but solutions to Equation 10A and 10B are plotted along with 30 % immobile fraction i.e. $\beta = 0.3$. As seen, the recovery does not reach a steady state in comparable frame numbers (compare with Figure 5-2). Unlike the results in Figure 5-2, Figure 5-3A shows the presence of a peak in intensity such that the fluorescence intensity initially increases but then decreases. This is due to the fact that the immobile fraction (which by definition cannot exchange during the recovery process) continues to get bleached during the imaging process (as indicated by the decaying grey line in Figure 5-3B). Also, due to the bleaching of the immobile fraction, there can also be parameter conditions where the total intensity decays instead

of recovering (see decaying curve in Figure 5-3A). For Equation 10A and 10B, a steady state is only achieved when the immobile fraction is completely bleached.

Figure 5-3C shows the effect of the immobile fraction itself on the recovery curve. With an increasing immobile fraction, the recovery transients show a pronounced decay, and for high enough values, the recovery falls below the initial fluorescence value.

Figure 5-3D shows the effect of $\lambda_1\omega$ on the recovery process; the extent of photobleaching during image capture again significantly decreases the net recovery; a maximum in fluorescence intensity is predicted

Analysis of Focal Adhesion Protein Exchange

As an example of the application of the model above, we performed FRAP analysis of the focal adhesion protein GFP-VASP. As we have shown before(133), the recovery curves in the case of focal adhesion proteins yield the parameter k_{OFF} . We first measured the immobile fraction in the chosen adhesion (Figure 5-4) by performing an initial bleach, capturing a single image immediately after bleach and a second image ~80 seconds later (when the recovery transients were determined to reach a steady state). The immobile fraction was calculated from the formula $\beta = \frac{\hat{C}_1 - \hat{C}_\infty}{\hat{C}_1(1 - \alpha)}$ and was found to be 0.0263 (solid circles in Figure 5-4B show the normalized concentrations immediately after bleach $\hat{C}_2 / \hat{C}_1 = \alpha$ and after recovery $\hat{C}_\infty / \hat{C}_1$).

Next, FRAP analysis was performed on the same focal adhesion in which β was measured above. The unknown parameters (as seen from Equation 5-10) are $\lambda_1\omega$, $\lambda_2\omega$ and k_{OFF} . First, a FRAP experiment was performed such that relatively little photobleaching occurred during image capture. The intensity of the free protein was

approximately constant (Figure 5-4D). The normalized recovery was fit to a model (Figure 5-4B); as seen the model satisfactorily captures the recovery and the subsequent, slight decline in the fluorescence recovery. The recovery is substantially less than the recovery observed in the experiment to calculate the immobile fraction above, suggesting an effect of photobleaching due to image capture on the bound fluorescence in the focal adhesion. If this data was used to erroneously calculate the immobile fraction, it would yield a value of $\beta = 0.48$, a significantly different value than the actual value determined above.

Next the experiment was repeated in the same focal adhesion but under higher excitation laser intensities to induce more photobleaching of the cytoplasmic pool. The fluorescence recovery occurred with a marked decrease in the intensity at later times. The model again was able to describe the decrease in the intensities, and parameters could be estimated. Importantly, the k_{OFF} determined from the two different experiments matched very well (0.17 s^{-1} versus 0.18 s^{-1}). Also, the $\lambda_2\omega$ value determined from fitting in Figure 5-4E is close to that from fitting in Figure 5-4C (0.012 versus 0.009). This suggests that the model is able to estimate the kinetics of dissociation accurately despite the effects of photobleaching during image capture. When the data in Fig. 4B was fit to the conventional model $\frac{\hat{C}(t) - \alpha\hat{C}_1}{\hat{C}_\infty - \alpha\hat{C}_1} = 1 - e^{-tk_{OFF}}$, the value of k_{OFF} was found to be 0.3, a clear difference in the value obtained from the above model (Figure 5-5).

Discussion

The analysis of FRAP experiments is an ongoing area of research. Among the many complicating factors(88), the effect of photobleaching by the image capture itself

has not received much attention. In this paper, we propose an approach to account for this by explicitly including photobleaching into the modeling of the fluorescence recovery process. The method involves modeling the unobserved dynamics (which by definition are unaffected by photobleaching), and modeling the photobleaching during the period of observation. As the observation occurs at discrete time intervals (i.e. images collected at discrete time intervals), the photobleaching is modeled to occur at discrete time intervals superimposed on the unobserved dynamics that occur continuously.

A simple conclusion from the modeling is that the immobile fraction should not be calculated from the FRAP curve itself (as is common practice). Instead, the number of frames should be minimized, preferably to only three frames: one before bleach, one immediately after, and one when the recovery reaches a steady state (the characteristic time scale for the steady state can be established from separate FRAP experiments). As seen in Figure 5-4B, the value of β would be 0.4838 if calculated from the FRAP experiment data (*) instead of 0.0263 from an independent experiment (solid circles) with only three frames collected. Another important concept is that the immobile fraction continues to be photobleached by the image capture process, leading to decay in the total fluorescence. Therefore, the FRAP curve is a combination of dynamics due to exchange of the mobile species, bleaching of the recovered portion due to the imaging process and the decay due to bleaching of the immobile fraction.

The main utility of this approach is when the bleaching during image capture significantly changes the FRAP dynamics. To test the extent of bleaching, the approach should be to first estimate the immobile fraction as described above. Then when the FRAP experiment is performed, the apparent immobile fraction from the FRAP

experiment should be compared with the measured immobile fraction. A decrease from the actual immobile fraction indicates the extent to which photobleaching during image capture is relevant in the experiment. The effect of photobleaching may be unavoidable either due to the fact that the fluorophore may be particularly susceptible to bleaching or the intensity of the fluorophore in some cells may be lower than others requiring a higher excitation intensity leading to higher bleaching. In this situation, Equation 10A and 10B should be used to fit the FRAP experiment. The parameters that are known in these equations are α , β and τ (measured or known directly from the experiment). The fitting should determine the values of $\lambda_1\omega$, $\lambda_2\omega$ and k_{OFF} . In situations where the diffusing cytoplasmic (or membranous) molecules can be tracked (such as in the example in Figure 5-4), it is useful to determine the value of $\lambda_2\omega$ from fitting the cytoplasmic pool, such that only two parameters need to be estimated.

An interesting prediction is that when the immobile fraction is present, the fluorescence in a FRAP experiment can reach a maximum and decay subsequently. The decay is due to the bleaching of the immobile fraction. Eventually, a steady state is reached when the bleaching due to image capture is compensated by recovery (unobserved dynamics). In the absence of the immobile fraction, the fluorescence reaches a steady state without reaching a peak. If bleaching due to image capture is so severe that the free molecules (in the cytoplasm) are bleached with each captured image, then there will be significant decay in the FRAP experiment and no steady state will be reached.

Sometimes researchers vary the time interval during FRAP experiments such that images are collected at a higher rate at the beginning of the recovery, and a smaller

rate at later stages. We explored the prediction of Eq. 6 with parameters $k_{OFF} = 0.2$, $\alpha = 0.2$, $\lambda \omega = 0.2$, $\tau = 2s, 4s$ and $6s$ (τ increased after every 10 images). At every increase τ , the steady state fluorescence recovery is predicted to increase (Figure 5-6A) leading to ‘bumps’ in the recovery process. The increase is due to a longer time interval between image captures that allows for more recovery in between successive image capture events (the bleaching due to image capture remains the same). If a conventional model $\frac{\hat{C}(t) - \alpha\hat{C}_1}{\hat{C}_\infty - \alpha\hat{C}_1} = 1 - e^{-k_{OFF}t}$ is used to fit this model-generated data, the k_{OFF} is estimated to be 0.085, which is much different from the real value $k_{OFF} = 0.2$ (Figure 5-6B).

This approach is applicable to more complicated situations. The method is to substitute Equation 5-4 with the relevant model for the unobserved dynamics (for example, models that include equations for coupled transport and binding). The main concept is to replace the initial condition for the unobserved dynamics in between frames with the bleaching-corrected concentration from the previous time interval. Thus, the approach is general and should work for any FRAP analysis.

If the values of the bleaching parameter λ are calculated not from FRAP experiments, but from whole-cell imaging experiments with Equation 5-3, then it is important to ensure identical imaging conditions for the corresponding FRAP experiments. This is because λ depends on experimental conditions including the exposure time and the excitation intensity; changing imaging conditions will change λ , thereby invalidating the analysis for the FRAP experiment.

Summary of the Model

Fluorescence recovery after photobleaching (FRAP) is a powerful technique to study protein kinetics in living cells. A lot of interesting work has been done using this technique. However, some important factors have been ignored when interpreting the results of FRAP experiment in those past study. A key factor is bleaching due to the image capture. In this chapter, we proposed a new model which including the effect of bleaching due to the image capture. The model was tested in the analysis of our experimental results. This model gives us better interpretation of FRAP experiments.

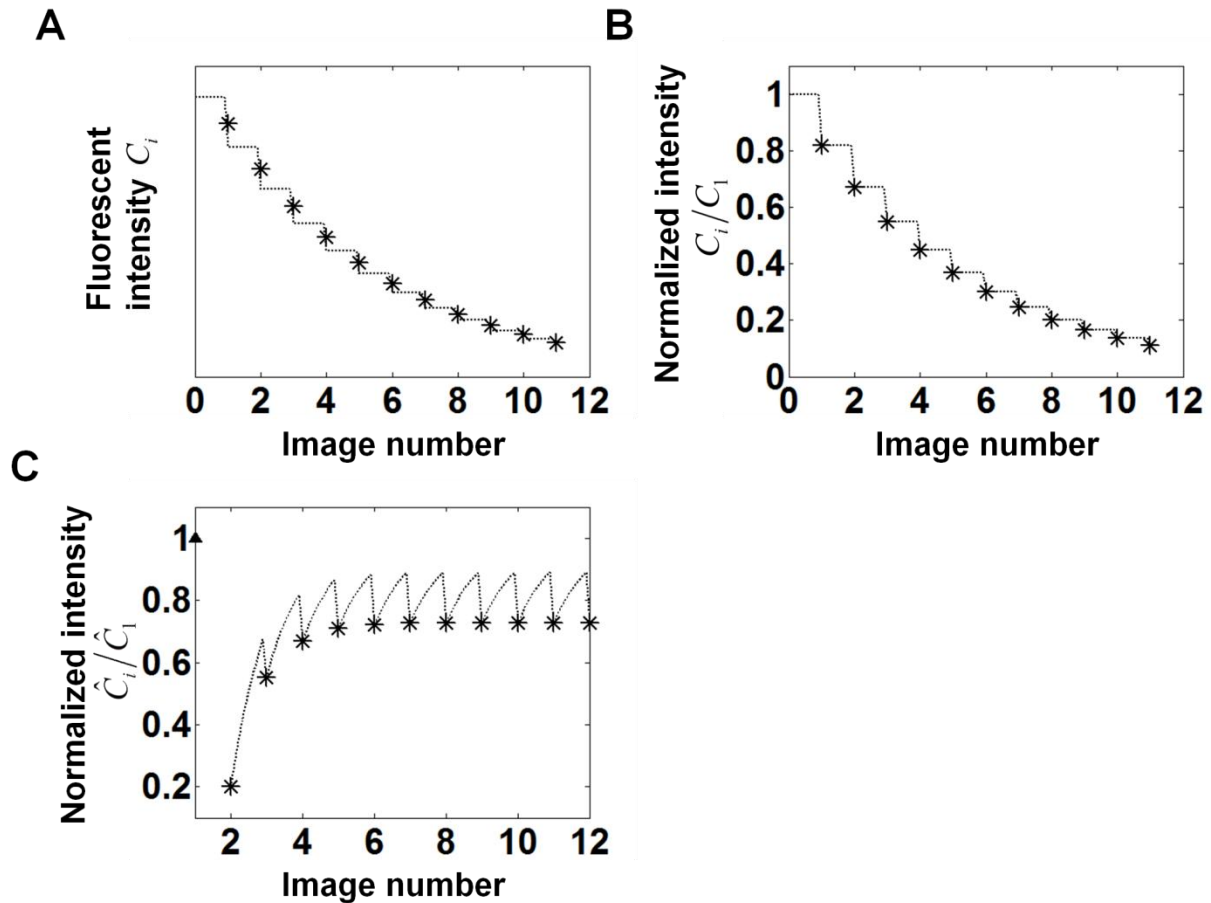


Figure 5-1. Hypothetical effect of photobleaching due to imaging capture on a whole cell imaging experiment. (A) The dotted lines indicate the actual decay of the fluorescence due to photobleaching during image capture. * indicates the measured intensity from the resulting image. (B) Averaging involved in the imaging process is cancelled by normalization (see text for more details). The normalized average fluorescence is now equal to $\frac{C_i}{C_1}$ as seen in the plot. (C)

Effect of photobleaching on hypothetical FRAP recovery. The dotted curve is the actual dynamics consisting of (unobserved) recovery interspersed by bleaching during image capture, * indicates measured intensity. The solid triangle at $i=1$ indicates the normalized initial intensity before photobleaching.

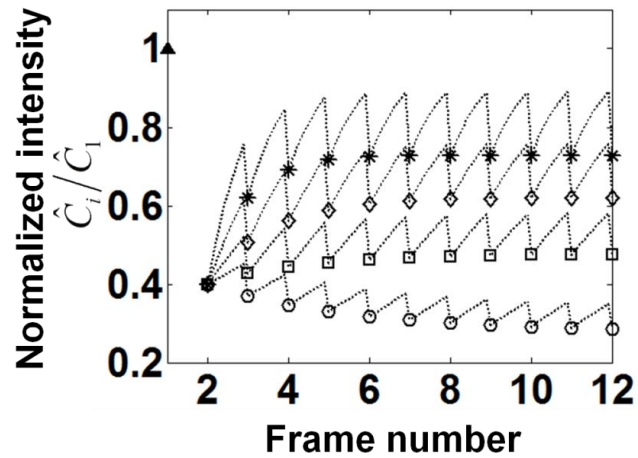


Figure 5-2. Solutions to Equation 5-6 showing how photobleaching during image capture can give the erroneous impression of an 'immobile' fraction. Recovery curves are shown with $\alpha = 0.4$, $\lambda\omega = 0.2$, $\tau k_{OFF} = 1$ (*), 0.5 (\diamond), 0.25 (\square) and 0.1 (\circ) (from top to bottom). For plotting purposes, ω is assumed to be $\tau/10$. The solid triangle at $i = 1$ indicates the normalized initial intensity before photobleaching.

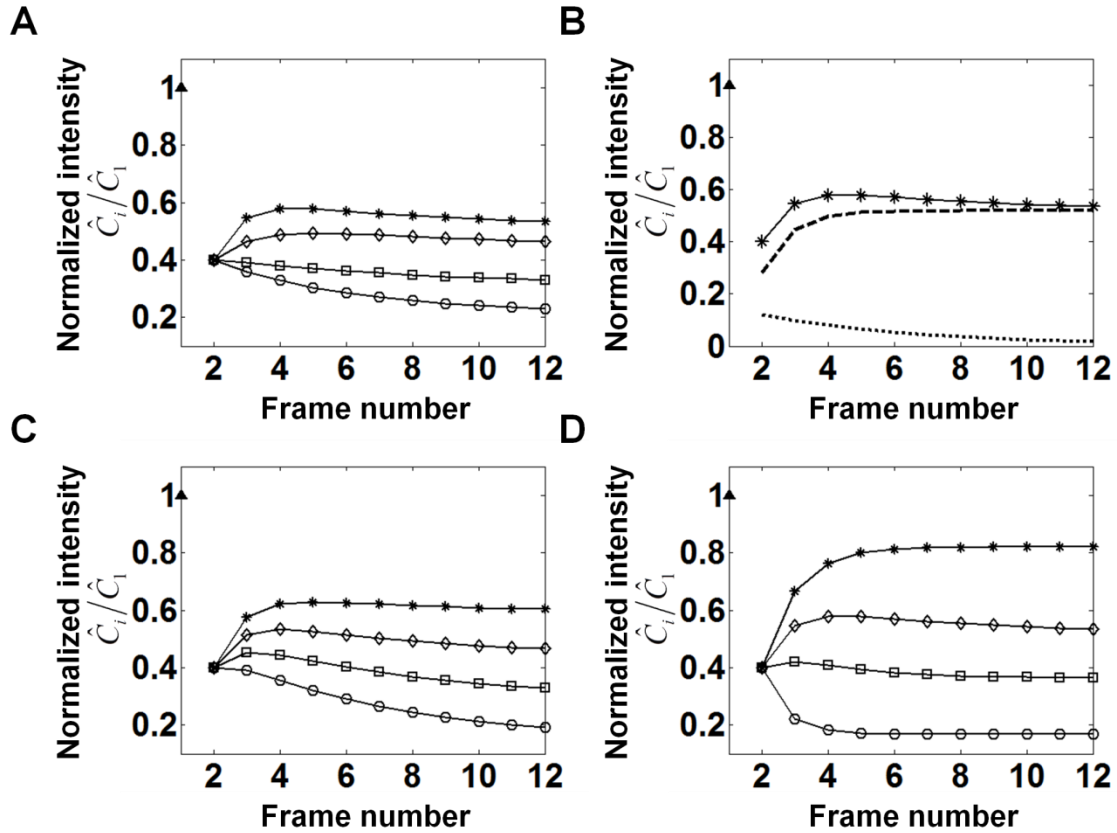


Figure 5-3. Solutions to Equation 5-10A and 10B that account for the presence of an actual immobile fraction. (A) Observed recovery curves with $\alpha = 0.4$, $\beta = 0.3$ (immobile fraction), $\lambda_1\omega = 0.2$, $\lambda_2\omega \ll 1$ (i.e. negligible photobleaching of the cytoplasmic molecules such that $g_2 = 1$) and $\tau k_{OFF} = 1$ (*), 0.5 (\diamond), 0.25 (\square), 0.1 (\circ) (from top to bottom). (B) Illustration of behavior of mobile (dashed line) and immobile fractions (dotted line) during recovery for $\tau k_{OFF} = 1$ (* indicates total intensity). The immobile fraction can be seen to decay due to bleaching during image capture, resulting in a decrease in the total fluorescent intensity. (C) Effect of the immobile fraction on the observed recovery curves. $\alpha = 0.4$, $\lambda_1\omega = 0.2$, $\lambda_2\omega \ll 1$, $\tau k_{OFF} = 1$ and $\beta = 0.2$ (*), 0.4 (\diamond), 0.8 (\square), 0.6 (\circ) (from top to bottom). Pronounced transients are observed in the recovery. (D) Effect of the bleaching function $\lambda_1\omega$ on recovery. Observed recovery curves with $\alpha = 0.4$, $\beta = 0.3$, $\lambda_2\omega \ll 1$, $\tau k_{OFF} = 1$, and $\lambda_1\omega = 10^{-6}$ (*), 0.2 (\diamond), 0.46 (\square), 1.1 (\circ) (from top to bottom). Solid triangles at $i = 1$ in all figures indicate the normalized initial intensity before the photobleaching.

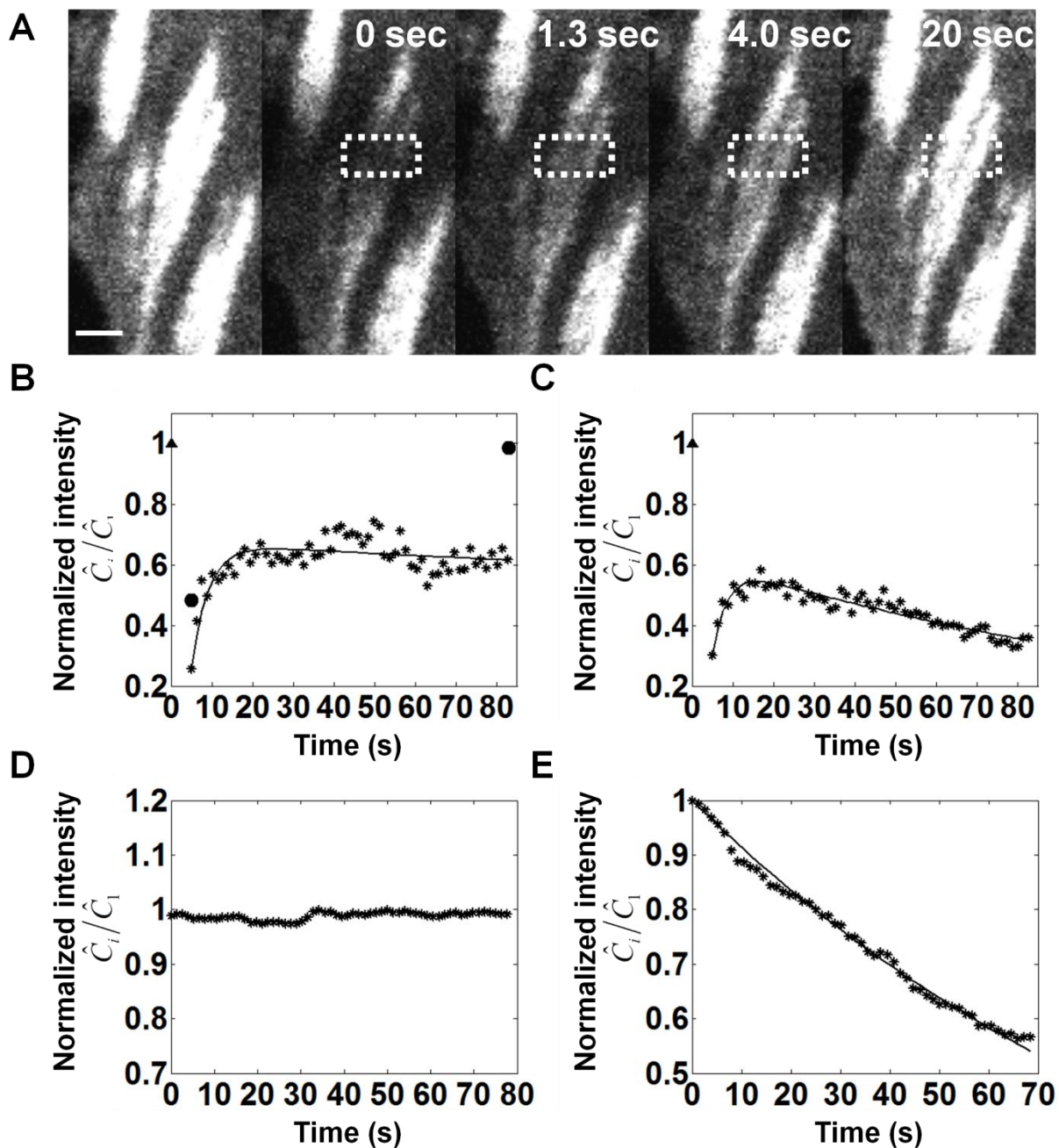


Figure 5-4. Example of the application of Equation 5-10A and 10B for fitting a GFP-VASP FRAP experiment. (A) Captured images from a FRAP experiment in an NIH3T3 fibroblast expressing GFP-VASP. The box shows the bleach spot. Scale bar, 1 μm . (B) Observed recovery with only slight apparent bleaching of the free molecules (in the cytoplasm) due to image capture. The excitation laser intensity was 4%. The solid curve is the fitting of the data to the model in Eq 9. The immobile fraction $\beta = 0.0263$ was estimated from a separate experiment (solid circles) in the same focal adhesion as described in **Material and Methods**. The value of α was determined from the fluorescence values

before and immediately after the bleach, and $\tau = 1.3\text{s}$ in the experiment. The fitting yielded the parameters $\lambda_1\omega = 0.0902$, $\lambda_2\omega = 0.0014$, $k_{OFF} = 0.17\text{ s}^{-1}$. (C) Observed recovery in the same focal adhesion from a second FRAP experiment with apparent bleaching. The excitation laser intensity was increased to 10%. The fluorescence is observed to go through a peak and then decrease due to bleaching caused by image capture. The fitting of the data to the model gave the parameters $\lambda_1\omega = 0.1301$, $\lambda_2\omega = 0.0091$, $k_{OFF} = 0.18\text{ s}^{-1}$. The value of k_{OFF} is very close to that estimated from the fitting in (B) thus validating the model. Solid triangles in (B) and (C) indicate the normalized initial intensity before the photobleaching. (D) Fluorescent intensity profile in the cytoplasm (free molecules) in experiment (B), which shows there is no detectable photobleaching of cytoplasmic molecules. (E) Fluorescent intensity profile of the cytoplasm (free molecules) in experiment (C) showing a clear decrease in the concentration due to pronounced bleaching. Fitting of the cytoplasmic intensity to Eq. 3 yields the bleaching parameter $\lambda_2\omega = 0.0118$, which is very close to the value determined from the fitting in (C). The model for the cytoplasmic intensity was fit to 70 of the 80 seconds for which the data was collected (corresponding to 53 measurements); the first 10 seconds showed a significant deviation possibly due to deviations in focus.

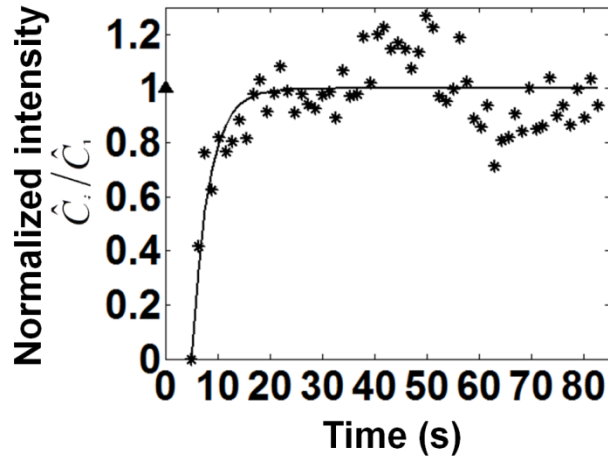


Figure 5-5. Typical fitting for a GFP-VASP FRAP experiment. The same FRAP experiment data as shown in Fig. 4B was fit to $\frac{\hat{C}(t) - \alpha\hat{C}_1}{\hat{C}_\infty - \alpha\hat{C}_1} = 1 - e^{-tk_{OFF}}$. The fitting yielded $k_{OFF} = 0.30$.

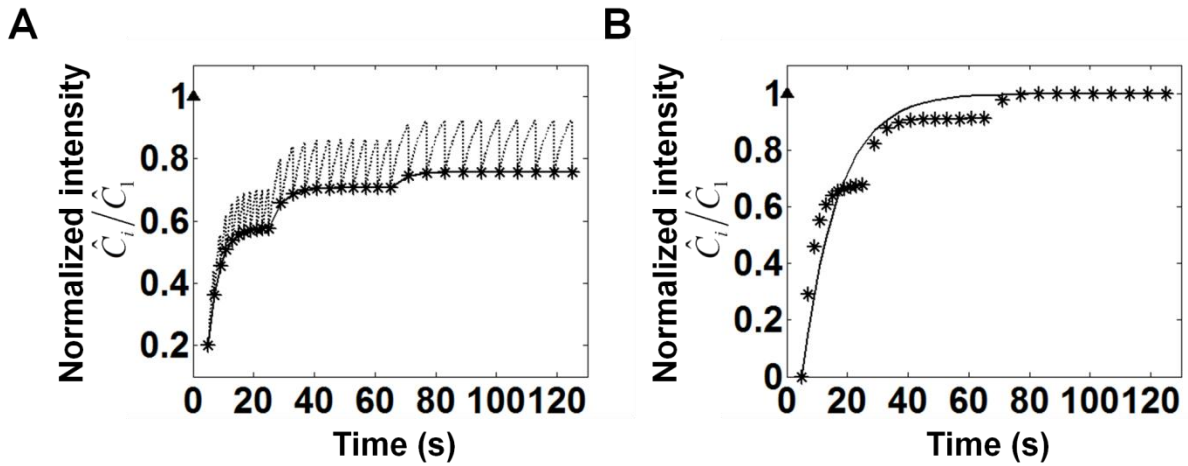


Figure 5-6. Illustration of typical fitting failed to estimate k_{OFF} in experiments with different time interval τ . (A) Observed recovery curve (solid line and *) calculated by Eq. 6 with parameters $k_{OFF} = 0.2$, $\alpha = 0.2$, $\lambda\omega = 0.2$, $\tau = 2s$, $4s$, $6s$ (it increases after every 10 frames). Dot lines show unobserved dynamics. (B) The solid line is fitting to the data in (A) to $\frac{\hat{C}(t) - \alpha\hat{C}_1}{\hat{C}_\infty - \alpha\hat{C}_1} = 1 - e^{-tk_{OFF}}$. The fitting yielded the parameter $k_{OFF} = 0.0846$.

CHAPTER 6 CONCLUSIONS

Molecular motors in living cells play very important roles in mechanotransduction and intracellular traffic. This dissertation focussed on molecular motor forces and their effects on nuclear and meicrotubule mechanics. Our findings significantly advance the understanding of nuclear movement and related cytoskeletal mechanics as summarized below.

Summary of Findings

Nuclear Rotation in Living Cells

Nuclear rotation has been observed in different types of cells for decades, and it is especially visible in certain cell types like fibroblasts. However, the biological function of nuclear rotation remains unknown. In this study, the focus was on investigating the mechanism for torque generation on the nucleus. We found that the angle of nuclear rotation is directionally persistent on a time scale of tens of minutes, but rotationally diffusive on longer time scales, and this rotation required the activity of the microtubule motor dynein. Based on these results, a mechanical model describing torque generation on the nucleus was proposed. A key prediction of the model is that the magnitude of nuclear rotation depends on the distance between the centrosome and nuclear centroid, which was confirmed by nuclear rotation experiments in patterned cells.

Nuclear Translation in Living Cells

Whether the nucleus is primarily “pushed” into position by compressive cytoskeletal forces, or “pulled” by tensile cytoskeletal forces is still controversial. In our study, we designed two independent experiments utilizing two novel techniques, protein photo activation and cell micromanipulation to investigate force exerted on the nucleus.

The results suggest that there is a tug of war between forward pulling and rearward pulling forces on the nuclear surface and the contractile force transmits through the nucleus from cell leading edge to the trailing edge in single migrating cells.

Effects of Dynein on Microtubule Mechanics and Centrosome Centering

Contrasting models of centrosome centering have been proposed in the past decade, and the main argument between these models is whether the cell positions the centrosome by pulling force or pushing force from dynamic microtubules. We approached this problem from single microtubule mechanics. By using femtosecond laser ablation, we showed that the freed minus-end fragments generated by severing microtubules didn't not straighten as expected if the buckling was caused by compressive forces. Moreover, the curvature of the minus-ended severed MT increased in most cases. When dynein was inhibited, the freed minus-end fragments did straighten out after severing. We proposed a model for dynein pulling force generation and conducted simulations of centrosome centering using the model. According to our model, microtubules are under tension along most of their length, while tips near the cell periphery are likely to be under compression due to polymerization forces. The simulations further confirmed that dynein-dependent forces are essential for centering the centrosome in endothelial cells and a balance of tensile and frictional forces from the dynein motors is sufficient to explain centrosome centering.

FRAP Model Accounting for Immobile Molecules and Bleaching due to Image Capture

FRAP is a popular technique to study protein diffusion and binding kinetics in living cells. A lot of research has been done using this technique(85-92, 133), though an important factor, the bleaching effect due to image capture, has not received attention.

The analysis of FRAP data is normally done by fitting the data to a continuous kinetic model. However, when the loss of fluorescence due to image capture is considered, the recovery function is affected at regular intervals due to image capture which occurs at certain time intervals. To provide a better interpretation of the FRAP data, we proposed a new model which accounts for the bleaching due to image capture. We also designed experiments from which we can calculate the fraction of immobile fluorescent molecules with minimum effect of the photobleaching. The kinetic parameters obtained by fitting of FRAP data with bleaching due to image capture at different levels were very close to each other, which validates our model to be reasonable and effective.

Future Work

Further Investigation on Nuclear Movement

Microtubule motor kinesin in nuclear rotation

In Chapter 2, a nuclear rotation model based on force generated by microtubule motor dynein walking on dynamic microtubules was proposed. The other microtubule motor kinesin is also known to affect intracellular transport, microtubule depolymerization and spindle formation(14, 30, 145, 163). Similar to dynein, kinesin-1, one member of kinesin family, walks on microtubule toward the plus end. It has recently been found to form complexes with nesprin-2 by associating with and recruiting kinesin light chain1 (KLC1) to the outer nuclear membrane(164). Kinesin-1/nesprin-2/SUN-domain macromolecular assemblies, spanning the entire nuclear envelope (NE), function in cell polarization by anchoring cytoskeletal structures to the nuclear lamina(164). Therefore, kinesin could play a role in nuclear rotation.

To investigate this, we could use the methods developed in Chapter 2. If kinesin-1 is shown to affect nuclear rotation, we can incorporate forces generated by kinesin into our model.

Actomyosin contraction and nuclear positioning

We found that the nucleus is subject to contractile forces generated by actomyosin from both the leading edge and the trailing edge. While these studies gave us a good understanding of the nature of forces driving nuclear motion, the magnitude of this actomyosin contractile force is unknown.

To measure the actomyosin contractile force, we can combine the protein photo activation technique with traction force microscopy(59, 125). The strategy is to seed cells on to soft substrate (eg. polyacrylamide gels) with fluorescent nano beads embedded, and then conduct the experiment as described in Chapter 3. By recording the bead movement upon photo activation, we should be able to estimate the scale of the contractile force generated by actomyosin.

A further study of long term nuclear movement upon photo activation could also provide a good readout of the force generation by actomyosin. An issue with such experiments is that cells are migrating and constantly changing their shape, which in turn introduces a lot of complexity in characterizing actomyosin contractile force induced nuclear translation. Micropatterning could eliminate the effects of both cell migration and shape changes, which provides an effective system to focus on the effect of actomyosin contractile force on nuclear translation. It would also be interesting to observe what would happen to the nucleus and the centrosome over time by carrying out photo activation in patterned squared cells, since there is no polarity in these cells as the centrosome overlaps with the nucleus (Figure 2-7).

The role of intermediate filament in nuclear movement

Among the three components of cytoskeleton, the role of intermediate filaments (IF) in nuclear movement is relatively unknown. Fluorescent images of NIH 3T3 fibroblasts and BCE cells transfected with vimentin plasmid show that intermediate filaments are present throughout the cell and form a very dense network around the nucleus (Figure 6-1). There are no known examples of IF-dependent cell movements or motor proteins that move along intermediate filaments. Therefore, the basket-like network of IF around the nucleus would most likely introduce frictional forces that oppose movements of the nucleus.

Consistent with this idea, Gerashchenko *et al.*(49) showed that vimentin IFs inhibit nuclear rotation, and variant proteins of the mutated wild type gene for vimentin that lacked considerable fragments of the N- and C-terminal domains restored nuclear anchoring.

Some proteins have been identified as the connectors between IF and the nucleus. Ralston *et al.*(165) showed that the desmin knock-out mouse muscle had mispositioned nuclei. Vimentin was found to be closely associated with the nucleus and mutant forms of vimentin exhibit nuclear morphology defects (166). A newly identified KASH protein, nesprin-3, likely functions to connect the outer nuclear membrane to intermediate filaments (167). Plectin, a plakin family member, consists of an actin-binding domain, an extended coiled-coil domain, and an intermediate filament-binding domain and can crosslink actin filaments to intermediate filaments (168). It is hypothesized that nesprin-3 and plectin together could extend from the outer nuclear membrane into the cytoplasm to interact with intermediate filaments (167).

Therefore, using the methods we developed in this thesis, we should be able to investigate the role of IF in nuclear rotation and translation by interrupting the connections between IF and the nucleus. These studies could also potentially give us better understanding of IF mechanics.

Nuclear Positioning under the Influence of Extracellular Forces

Endothelial cells form the inner wall of blood vessels. They are constantly subjected to shear stresses created by blood flow. Thus, an interesting problem is to investigate how the cell positions its nucleus under such a condition.

A typical device for shear stress experiment is the parallel plate flow chamber as described in(169). Lee *et al.*(48) have shown that shear stress caused cell polarization, in which it appeared that the centrosome moved against the direction of flow. However, it is also possible that the nucleus could have moved downstream while the centrosome stayed in the same position, similar to what has been observed in nuclear movement in wounded cells(5). Some related questions to be answered are how the nuclear translation and centrosome positioning coordinate with cell migration under shear stress? What are the effects of motor forces (ie., dynein and actomyosin) on the nuclear movement under shear stress? Combining shear stress flow experiment with the methods that we used to study motor forces and nuclear positioning (eg., tracking nuclear position, centrosome position and cell centroid, inhibition of dynein and myosin etc.), we should be able to answer such questions and improve our understanding of nuclear movement in general.

Cell Migration During Wound Healing

The scratch wound healing assay has been used as an effective method to study collective cell migration speed for decades. While this method is easy to carry out and

gives clear results in comparing cell migration under different conditions(59), it is missing some key features that are observed during the wound healing *in vivo*. One of these is that cells need to clean up the debris of cells in the wound to be able to move on, while it is a clean wound in the scratch wound healing assay.

Our group has developed a new stamping wound healing assay which addressed this issue(170). The method involves the physical contact of a soft mold with raised features onto confluent epithelial cells. With this method, we successfully created well-defined wounds with dead cell debris in the wound area. Our previous study has shown that the debris clearing process was remarkably efficient with no trace of debris detectable after clearance. The rate of wound closure in the presence of cell debris was found to be comparable to that in the absence of cell debris.

In the body, other cells like macrophages and neutrophils might also be involved in the wound healing process. A macrophage is supposed to phagocytose (engulf and then digest) cellular debris, and neutrophils are an important part of the innate immune system. They are one of the first-responders of inflammatory cells to migrate towards the site of inflammation. So it would be very interesting to see how these cells react to the wounding. The strategy would be to first co-culture macrophages or neutrophils with fibroblasts or epithelial cells, then create a wound using our stamping assay and record cell migrations. Macrophage or neutrophils can be labeled with a fluorescent tracker, so we can differentiate their movement from fibroblasts or epithelial cells. These experiments would significantly advance the *in vitro* wound healing study.

Effects of Other Motor Forces on Microtubule Mechanics

We discussed motor protein dynein as the major force generator in shaping microtubules. However, we do not rule out the possible contribution by kinesin, which

can also link a microtubule to the cytoskeleton. Similar laser ablation experiments can be done to microtubules in kinesin inhibited cells to verify the effect of kinesin on microtubule mechanics. If a significant effect is observed, we can incorporate kinesin forces into the motor model in a manner similar to dynein but with opposite direction.

A key assumption made in in Chapter 4 was that the underlying cytomatrix that the dynein binds to for pulling on microtubules is stationary (as the schematic in Figure 6-2). However in migrating cells, the underlying cytomatrix is highly dynamic due to the constant polymerization of actin filaments and the subsequent shape changes of the cell. Acto-myosin contraction has been shown to cause MTs buckling and promote MTs breaking in motile cells(72, 73, 171). This is consistent with our model discussed before, in which the pulling force on microtubules generated by dynein requires anchorage of dynein to the F-actin network. So when acto-myosin retrograde flow occurs, it could generate forces on the dynein that binds to the F-actin network, and consequently transfer forces onto the MTs.

The protein photo activation technique would be an excellent method to study effect of acto-myosin retrograde flow on microtubule mechanics. In our previous study, we noticed that when lamellipodia formed upon the photo activation of Rac-1, there was continuous acto-myosin flow being generated in the region of activation (Figure 6-3). We also observed remodeling of the stress fiber network in this region (Figure 6-3D and Figure 6-3E). Therefore, if we track the shape of GFP-tubulin labeled microtubules in the vicinity of the newly forming lamellipodia with time and compare the curvature of bent microtubules before and after the photo activation, we will be able to quantitatively test the effect of acto-myosin retrograde flow on microtubule mechanics. Furthermore,

the same experiment could be done in dynein inhibited cells. According to our hypothesis, inhibition of dynein would disrupt the linkage between F-actin network and microtubules and hence the effect of acto-myosin retrograde flow on microtubules would be reduced.

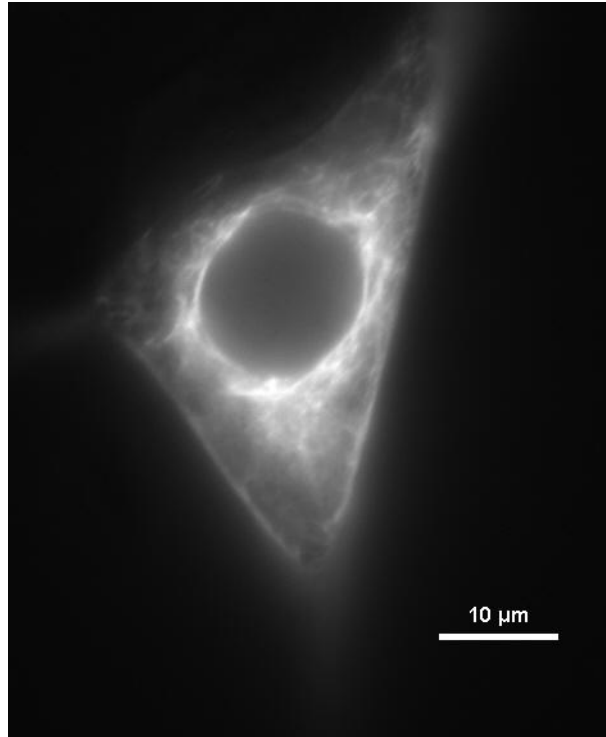


Figure 6-1. Image of intermediate filament in living cells. NIH 3T3 fibroblasts were transfected with CFP-vimentin. Intermediate filaments are most concentrated around the nucleus.

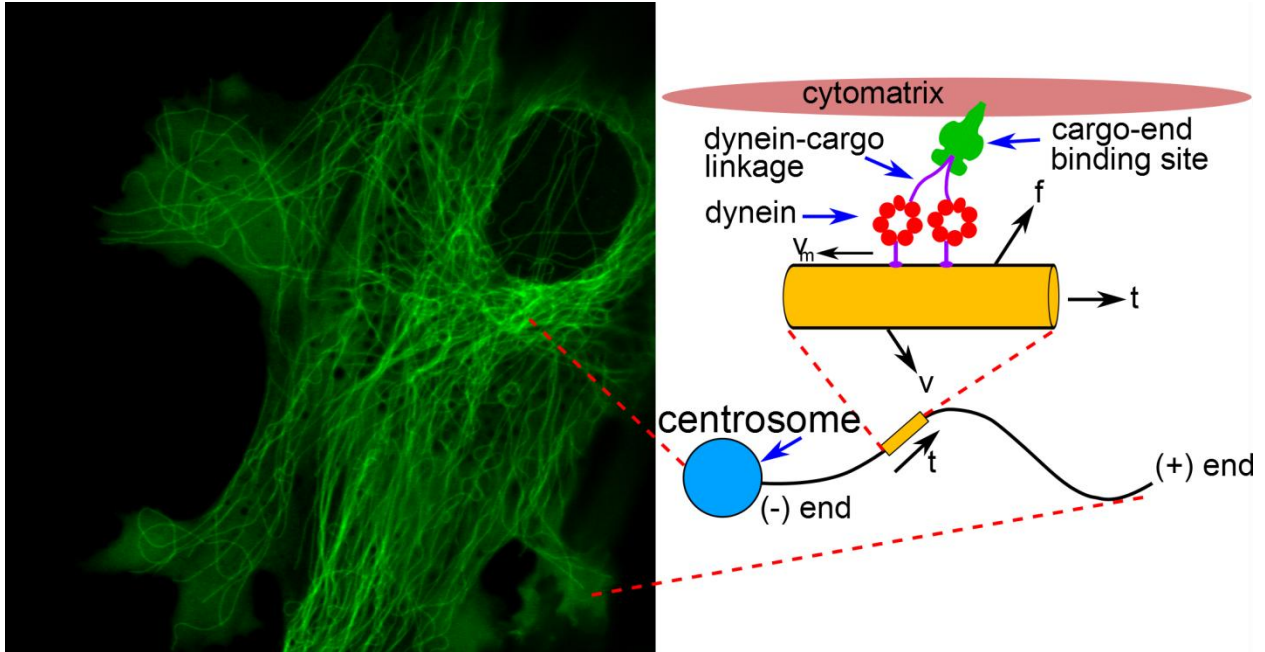


Figure 6-2. Cartoon of a dynein motor indicating how the minus-directed motor bound to the cytomatrix exerts a force towards the microtubule plus end. Individual dynein molecules walk towards the microtubule minus end at a speed v_m (along the local tangent direction, \hat{t}) that depends on the opposing force f . Each segment of the microtubule moves relative to the cytoskeleton with a velocity v .

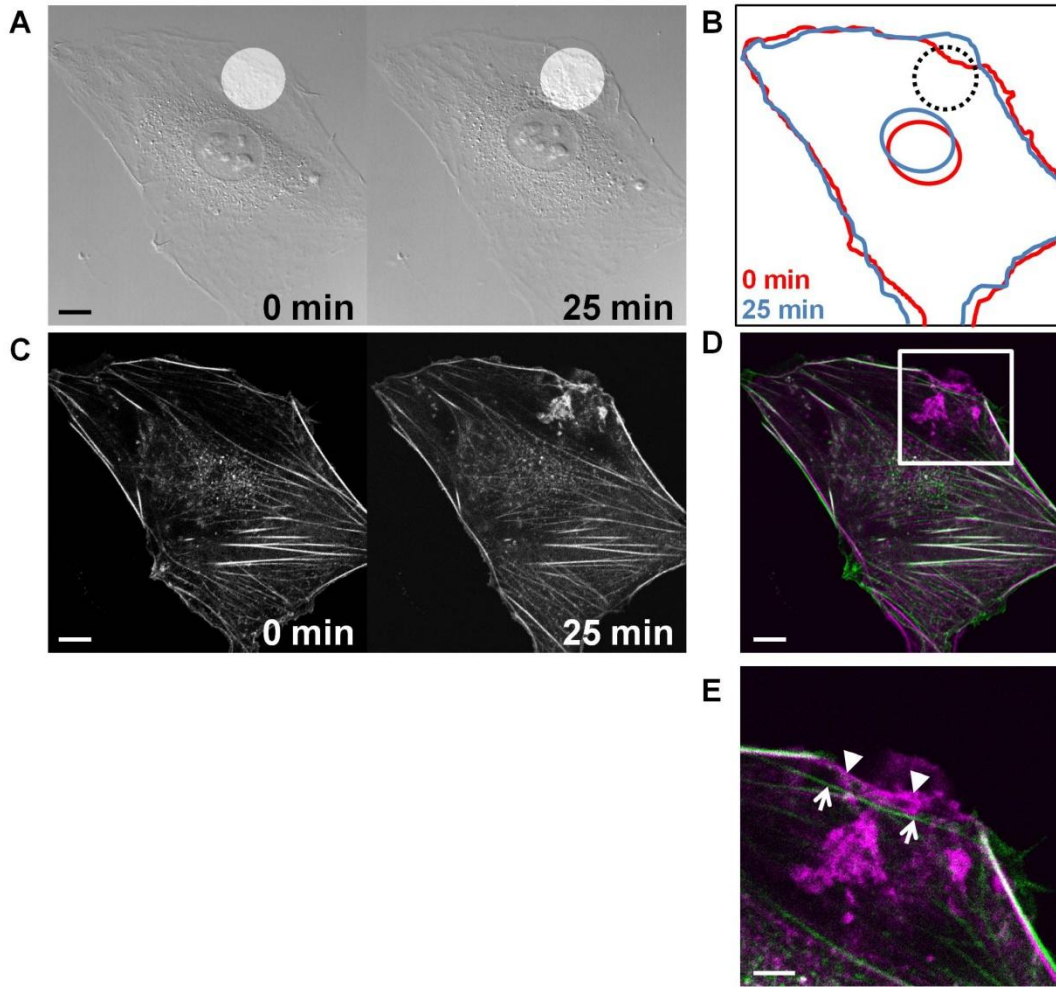


Figure 6-3. Formation of acto-myosin retrograde flow and stress fiber remodeling upon photo activation of Rac-1. A) DIC images of a NIH 3T3 fibroblast at the beginning and the end of photo-activation. The nucleus moved towards the activation. Bright spots are the activation region. (B) Super imposition of the cell out line and nucleus from frame 0 minute (red; beginning of Rac1 activation) and 30 minute (blue, end of Rac1 activation). Dash line circle is the activation region. (C) GFP-actin expressed NIH 3T3. No visual movement or the stress fiber was observed. (D) Overlay image of actin cytoskeleton at 0 minute (green) and 30 minute (magenta). No significant visual changes of stress fibers were observed. (E) Zoom-in image of the white square region in (D). Actin cytoskeleton underwent remodeling at the activation site. The stress fiber at 0 minute (open arrow head, green) disappeared at 30 minute, a new stress fiber was forming (arrow head, magenta). Lots of free actin (magenta) accumulated at the activation site. Scale bars (A), (C) and (D), 10 μm ; (E) 5 μm .

APPENDIX A MATLAB CODE FOR NUCLEAR ROTATION ANALYSIS

The strategy of nuclear rotation tracking was previous described in Material and Methods in Chapter 2.

```
%Start of NuclearRotation.m
clc
clear all
close all

matfiles=dir((fullfile('H:', 'nuclear rotation control
data', 'longtimedata', '112709-1-11data', '*.tif')));

num=5;%This is the size around the correlation peak to which we fit a
Paraboloid fitting, may be changed respective to the resolution of the image
template = imread(matfiles(1).name);
%Crop images of two nucleoli as templates
[croptemplate1, rectcroptemplate1] = imcrop(template);
[croptemplate2, rectcroptemplate2] = imcrop(template);
%Coordinates of the templates
x1 = rectcroptemplate1(1,1);
y1 = rectcroptemplate1(1,2);
width1=rectcroptemplate1(1,3);
height1=rectcroptemplate1(1,4);
x2 = rectcroptemplate2(1,1);
y2 = rectcroptemplate2(1,2);
width2=rectcroptemplate2(1,3);
height2=rectcroptemplate2(1,4);
%Recrop templates with roundup size. We round this because the way MATLAB
program works
croptemplate1=imcrop(template, [round(x1) round(y1) width1 height1]);
croptemplate2=imcrop(template, [round(x2) round(y2) width1 height1]);
%Image correlation give the displacement of the features
c1 = normxcorr2(croptemplate1,template);
c2 = normxcorr2(croptemplate2,template);
%Gaussian fitting to get the peak position in subpixels
[max_c1, imax] = max(c1(:));
[ypeak1old, xpeak1old] = ind2sub(size(c1),imax(1));
image=c1(ypeak1old-num:ypeak1old+num,xpeak1old-num:xpeak1old+num);
[param,px,py]=Gaussianpeaknew1(image);
zo = param(1); xpeaknew=param(2); ypeaknew= param(3); zn=param(4);
wnx=param(5); wny=param(6); theta=param(7);
x_sub=xpeak1old-num-1;
y_sub=ypeak1old-num-1;
xpeak1=xpeaknew+x_sub;
ypeak1=ypeaknew+y_sub;

[max_c2, imax1] = max(c2(:));
[ypeak2old, xpeak2old] = ind2sub(size(c2),imax1(1));
image=c2(ypeak2old-num:ypeak2old+num,xpeak2old-num:xpeak2old+num);
[param,px,py]=Gaussianpeaknew1(image);
```

```

zo = param(1); xpeaknew=param(2); ypeaknew= param(3); zn=param(4);
wnx=param(5); wny=param(6); theta=param(7);
x_sub=xpeak2old-num-1;
y_sub=ypeak2old-num-1;
xpeak2=xpeaknew+x_sub;
ypeak2=ypeaknew+y_sub;

%Calculate the actual positions
corr1{1}=c1;
corr2{1}=c2;
py1(1)=ypeak1;%x coordinates of starting points of croptemplate1 in
correlation
px1(1)=xpeak1;%y coordinates of starting points of croptemplate1 in
correlation
py2(1)=ypeak2;%x coordinates of starting points of croptemplate2 in
correlation
px2(1)=xpeak2;%y coordinates of starting points of croptemplate2 in
correlation
imag{1}=template;
magr1=sqrt((px2(1)-px1(1))^2+(py2(1)-py1(1))^2);
mag(1)=magr1%distances between two features in each image

%coordinates for the new templates in image{1}
w1=px1(1)-x1;
h1=py1(1)-y1;
w2=px2(1)-x2;
h2=py2(1)-y2;
ang(1)=0;
ang1(1)=0

t=50%Set how many images in the small loop, which use the same templates

for n=0:28%Set how many big loops (total number of images/number of images in
a small loop)
    a=1+t*n;
    xn1=px1(a)-w1;
    yn1=py1(a)-h1;
    xn2=px2(a)-w2;
    yn2=py2(a)-h2;

    croptemplaten1=imcrop(imag{a},[round(xn1) round(yn1) width1 height1]);
    croptemplaten2=imcrop(imag{a},[round(xn2) round(yn2) width1 height1]);
    croptemp1{1+n}=croptemplaten1;
    croptemp2{1+n}=croptemplaten2;

    figure(n+1)
    imshow(imag{a})
    hold on
    plot(px1(a)-size(croptemp1{n+1},2)/2,py1(a)-size(croptemp1{n+1},1)/2,'*')
    plot(px2(a)-size(croptemp2{n+1},2)/2,py2(a)-size(croptemp2{n+1},1)/2,'*')

for i = 2:t+1
    b=i+t*n;

image=imread(matfiles(b).name);

```

```

imag{b}=image;
c1 = normxcorr2(croptemplaten1,image);
c2 = normxcorr2(croptemplaten2,image);

[max_c1, imax] = max(c1(:));
[ypeak1old, xpeak1old] = ind2sub(size(c1),imax(1));
image=c1(ypeak1old-num:ypeak1old+num,xpeak1old-num:xpeak1old+num);
[param,px,py]=Gaussianpeaknew1(image);
zo = param(1); xpeaknew=param(2); ypeaknew= param(3); zn=param(4);
wnx=param(5); wny=param(6); theta=param(7);
x_sub=xpeak1old-num-1;
y_sub=ypeak1old-num-1;
xpeak1=xpeaknew+x_sub;
ypeak1=ypeaknew+y_sub;

[max_c2, imax1] = max(c2(:));
[ypeak2old, xpeak2old] = ind2sub(size(c2),imax1(1));
image=c2(ypeak2old-num:ypeak2old+num,xpeak2old-num:xpeak2old+num);
[param,px,py]=Gaussianpeaknew1(image);
zo = param(1); xpeaknew=param(2); ypeaknew= param(3); zn=param(4);
wnx=param(5); wny=param(6); theta=param(7);
x_sub=xpeak2old-num-1;
y_sub=ypeak2old-num-1;
xpeak2=xpeaknew+x_sub;
ypeak2=ypeaknew+y_sub;

py1(b)=ypeak1;
px1(b)=xpeak1;
py2(b)=ypeak2;
px2(b)=xpeak2;
%Calculate rotation angles using positions of two nucleoli
r1dotr2=(px2(a)-px1(a))*(px2(b)-px1(b))+(py2(a)-py1(a))*(py2(b)-py1(b));
magr1=sqrt((px2(a)-px1(a))^2+(py2(a)-py1(a))^2);
magr2=sqrt((px2(b)-px1(b))^2+(py2(b)-py1(b))^2);
angle = acosd(r1dotr2/magr1/magr2);

mag(b)=magr2;%Distance between two features in each image
ang(b)=angle;

one=atand((py1(a)-py2(a))/(px1(a)-px2(a)));
two=atand((py1(b)-py2(b))/(px1(b)-px2(b)));
angle1 = (one-two);

ang1(b)=angle1+ang1(a);%Accumulative rotation angles

end
end

```

APPENDIX B MATLAB CODE FOR NUCLEAR TRANSLATION ANALYSIS

Tracking nuclear positions in photoactivation experiments described in Chapter 3.

```
%Start of NuclearTranslation.m
clc
clear all
close all

matfiles=dir((fullfile('F:', 'Rac1NuclearTranslation', 'data', 'blebbistatin', '1
21610-4', '*.tif')));

%Position of activation center
i=2;%
image=imread(matfiles(i).name);
imag{i}=image;
imshow(imag{i});
[x1,y1]=ginput(12);%Choose a certain number of points to fit to a eclipse
ellipse_c=fit_ellipse(x1,y1);%Fit to a eclipse
xc1=ellipse_c.X0_in;
yc1=ellipse_c.Y0_in;%X,y coordinates of the center of the eclipse

imshow(imag{i});
[x2,y2]=ginput(12);
ellipse_c=fit_ellipse(x2,y2);
xc2=ellipse_c.X0_in;
yc2=ellipse_c.Y0_in;

imshow(imag{i});
[x3,y3]=ginput(12);
ellipse_c=fit_ellipse(x3,y3);
xc3=ellipse_c.X0_in;
yc3=ellipse_c.Y0_in;

xc=mean([xc1 xc2 xc3]);
yc=mean([yc1 yc2 yc3]);%Use the mean of results from three fittings as the
position of activation center

%Position of nuclei
m=31;
for i=1:m%length(matfiles)
    image=imread(matfiles(i).name);
    imag{i}=image;
    imshow(imag{i});
    [x,y]=ginput(12);
    ellipse_t = fit_ellipse(x,y);
    ellipse{i}=ellipse_t;
    xtrans(i)=ellipse_t.X0_in;
    ytrans(i)=ellipse_t.Y0_in;
end
%Calculate the distance between nuclear centroid and the activation center
%at each time point
```

```

for k=1:m;
    dl(k)=sqrt((xtrans(k)-xc)^2+(ytrans(k)-yc)^2);
end
%Calculate the changes of distance between nuclear centroid and the
activation center
%at each time point from time zero
d(1)=0;
for j=2:m;
    d(j)=dl(1)-dl(j);
end

clear imag

t=[0:5:5*(m-1)];
plot(t,d)

figure
plot(xtrans,ytrans,'-*',xc,yc,'o')
%Convert to actual length
px=0.087;%set the pixel size
xt=xtrans*px;
yt=ytrans*px;
xca=xc*px;
yca=yc*px;
dt=d*px;
%move the activation center as the origin of coordinates
xt0=xt-xca;
yt0=yt-yca;
xca0=0;
yca0=0;
%move the original position of the nucleus as the origin of coordinates
xtt=xt-xt(1);
ytt=yt-yt(1);
xcat=xca-xt(1);
yca0=yca-yt(1);
rotangle=atand(yca0/xcat);

```

APPENDIX C MATLAB CODE FOR CENTROSOME POSITION ANALYSIS

Tracking centrosome positions in experiments described in Chapter 3 and Chapter

4.

```
%Start of centrosome.m
clc
clear all
close all

n=1; %Starting image for analysis
m=28; %Ending image for analysis
threshold=2; % Set thresholding parameter, this depends on the image quality
num=5; % This is the size around the correlation peak to which we fit a
Paraboloid fitting, may be changed respective to the resolution of the image
px=0.088;% Pixel size

%Read the image files and collect information
matfiles2 =dir((fullfile('F:', 'newRac1NuclearTranslation', 'newdata',
'centrosome', '041311-3', 'centrosome', '*.tif')));
size_matfiles2=size(matfiles2);
for i =1:size_matfiles2(1)
temp_image = imread(matfiles2(i).name);
size_image=size(temp_image);
imag{i}=temp_image;
end

%Crop a template from the first image
[template, rectcrop] =imcrop(imag{1}, [min(min(imag{n})), max(max(imag{n}))]);
rectcrop(1)=round(rectcrop(1));
rectcrop(2)=round(rectcrop(2));
width=round(rectcrop(3));
height=round(rectcrop(4));
[template, rectcrop]=imcrop(imag{1}, [rectcrop(1), rectcrop(2), width, height]);%
We round this because the way MATLAB program works

save_template{1}=template;
save_rectcrop{1}=rectcrop;

%Eliminating noise based on the threshold given
imag_cent{1}=template;
imag_max=max(max(imag_cent{1}));
size_imag=size(template);
for i = 1:size_imag(1)
    for j = 1:size_imag(2)
        if imag_cent{1}(i,j)<imag_max/threshold
            imag_cent{1}(i,j)=0;
        else
            imag_cent{1}(i,j)=imag_cent{1}(i,j);
        end
    end
end
```

```

end
%Use built-in MATLAB functions to make a binary and calculate centroids
L = bwlabel(imag_centr{1});
s = regionprops(L, 'Centroid');

%Record the centroid coordinates
xcord(1)=s(1).Centroid(1)+rectcrop(1)-1;%coordinates of the centroids
ycord(1)=s(1).Centroid(2)+rectcrop(2)-1;
xCent(1)=xcord(1);
yCent(1)=ycord(1);

for g=2:m

image=imag{g};

[c,corner_y(g),corner_x(g),xrefined,yrefined,cvalue]=process(template,image,num); %This gives the corner position in the ith image of the old template
(i.e. from the i-1 image). The main code passes three things to the custom
function "process" including the template from image i-1, image i and the
parameter num.

x_offset(g)=round(rectcrop(1))-corner_x(g);
y_offset(g)=round(rectcrop(2))-corner_y(g); %this is the measured offset
immediately between images cvalues(g)=cvalue;

%Updated positions are calculated with the offsets and stored
xcord(g)=xcord(g-1)-x_offset(g);
ycord(g)=ycord(g-1)-y_offset(g);

dc(1)=0;
dc(g)= sqrt(x_offset(g)^2+y_offset(g)^2);

%Updated positions are used to determine the template position in image i
templatex=round(xcord(g)-width/2);
templatey=round(ycord(g)-height/2);

%Cropping new template for the next correlation
[template,rectcrop]=imcrop(imag{g},[templatex,templatey,width,height]);

%Refine the new template position by calculating the centroid
imag_centr{g}=template;
imag_max=max(max(imag_centr{g}));
size_imag=size(template);
for i = 1:size_imag(1)
    for j = 1:size_imag(2)
        if imag_centr{g}(i,j)<imag_max/threshold
            imag_centr{g}(i,j)=0;
        else
            %imag_centr(i,j)=255;
            imag_centr{g}(i,j)=imag_centr{g}(i,j);
        end
    end
end
end
end

```

```

L = bwlabel(imag_centr{g});
s = regionprops(L, 'Centroid');
%Store the centroid position as a secondary position for each time frame
xCent(g)=s(1).Centroid(1)+rectcrop(1)-1;
yCent(g)=s(1).Centroid(2)+rectcrop(2)-1;
%Redefine the new template positions using the calculated centroid
templatex=round(xCent(g)-width/2);
templatey=round(yCent(g)-height/2);

[template,rectcrop]=imcrop(imag{g},[templatex,templatey,width,height]);
%Save template and template coordinates
save_template{g}=template;
save_rectcrop{g}=rectcrop;

end
%Calculate the position in length
x=xCent*px;
y=yCent*px;
xd=xcord*px;
yd=ycord*px;
%Plot positions, template, binary images as subimages together
for l=n:m-1,

    image=imread(matfiles2(l).name);
    ima{1}=image;
    figure(l)
    subplot(1,4,1)
    imshow(ima{1})
    subplot(1,4,2)
    imshow(imag{1},[min(min(imag{n})),max(max(imag{n}))])
    hold on
    plot(xcord(1), ycord(1), 'bx')
    hold on
    plot(xCent(1), yCent(1), 'rx')
    subplot(1,4,3)
    imshow(save_template{1},[min(min(imag{n})),max(max(imag{n}))])
    subplot(1,4,4)
    imshow(imag_centr{1},[min(min(imag{n})),max(max(imag{n}))])

end

```

APPENDIX D
MODEL FOR MICROTUBULE MECHANICS AND CENTROSOME CENTERING

Microtubule Mechanics

The relaxation time of a bent microtubule in a viscous fluid can be estimated from the equation of motion for small displacements, u , from the straight configuration (146, 172)

$$m\ddot{u} + \xi\dot{u} + Bu'''' = 0 \quad (\text{D-1})$$

where m is the mass per unit length of the filament, ξ is the frictional resistance per unit length, and $B \simeq 25 \text{ pN } \mu\text{m}^2$ (52) is the flexural rigidity. The solutions are a linear combination of trigonometric and hyperbolic functions with a wave vector k . For a free-ended segment in the lowest energy mode $kl = 1.875$; thus, for a typical segment length ($l \simeq 3 \mu\text{m}$) $k \simeq 0.6 \mu\text{m}^{-1}$. Neglecting inertia, in the overdamped limit the relaxation time is given by

$$\tau = \frac{\xi}{Bk^4} \quad (\text{D-2})$$

The frictional resistance is given by $\xi = 4\pi\mu / \ln 2A$, where μ is the effective viscosity of the background fluid and the aspect ratio of the segment $A \simeq 120$. Estimates of the viscosity of cellular fluids range from 10^{-3} Pa s (water) to 10^{-1} Pa s (173, 174) and the corresponding relaxation times for $3 \mu\text{m}$ segments are in the range $10^{-3} - 10^{-1} \text{ s}$. Observations of microtubule straightening in dynein inhibited cells indicate that the effective viscosity controlling the relaxation of microtubules is much larger. We take a value $\mu = 10 \text{ Pa s}$, which gives a relaxation time of approximately 7 s for a $3 \mu\text{m}$ segment, similar to the experimental data in Figure 4-3A.

Model for Dynein Forces

In this model, the force exerted by a dynein molecule is assumed to depend on the displacement of the motor from the point of attachment to the microtubule (in a space-fixed frame), and has contributions from the motion of the microtubule as well as the motor. Individual dynein molecules walk toward a microtubule minus end at a speed v_m that depends on the opposing force, \mathbf{f} . For simplicity, the force-speed relation for dynein motors is taken as linear (109),

$$\frac{v_m}{v_0} = 1 - \frac{\mathbf{t} \cdot \mathbf{f}}{f_{max}} \quad (\text{D-3})$$

where v_0 is the speed of an unstressed motor, f_{max} is the motor stall force, and \mathbf{t} is a unit vector directed toward the plus end of the microtubule. The force on the cytomatrix linkage increases as dynein translates and begins to exert tension, while motion of the microtubule itself can also contribute to a change in force. Assuming that the dynein-linkages can be approximated as linear springs with stiffness κ ,

$$\frac{d\mathbf{f}}{dt} = -\kappa(\mathbf{v} - v_m \mathbf{t}) \quad (\text{D-4})$$

where \mathbf{v} is the local velocity of the microtubule relative to the cytoskeleton. The time-dependent force from a single motor follows from Equation D-3 and Equation D-4 with the initial condition $\mathbf{f}(0) = 0$;

$$\mathbf{f}(t) = f_{max} \left(1 - \frac{\mathbf{v} \cdot \mathbf{t}}{v_0}\right) (1 - e^{-t/\tau}) \mathbf{t} - \kappa \mathbf{v} \cdot (\mathbf{1} - \mathbf{t} \mathbf{t}) t \quad (\text{D-5})$$

where the timescale for the motor to stall $\tau = f_{max}/\kappa v_0$. Typical values for the parameters are: $\kappa = 1000 \text{ pN}\mu\text{m}^{-1}$, $v_0 = 0.8 \mu\text{m s}^{-1}$, and $f_{max} = 8 \text{ pN}$ (52, 109), leading to a timescale $\tau = 0.01\text{s}$.

Dynein linkages between the cytomatrix and the microtubule are assumed to dissociate with a first-order rate constant k_{off} , so that the probability of a linkage remaining at time t is $P(t) = e^{-k_{off} t}$. Thus the average force exerted by a single linkage over a time interval T is $\langle \mathbf{f}_l \rangle = T^{-1} \int_0^T \mathbf{f}(t) P(t) dt$. The mean linkage lifetime is k_{off}^{-1} and thus there are $k_{off} T$ linkages broken and reformed in the time interval T . The average force exerted by a dynein linkage that is associating and dissociating from the microtubule is therefore

$$\langle \mathbf{f} \rangle = k_{off} \int_0^\infty \mathbf{f}(t) P(t) dt = f_0 \left(1 - \frac{\mathbf{v} \cdot \mathbf{t}}{v_0} \right) \mathbf{t} - \frac{\kappa}{k_{off}} \mathbf{v} \cdot (\mathbf{1} - \mathbf{t} \mathbf{t}) \quad (\text{D-6})$$

where $f_0 = f_{max} / (1 + k_{off} \tau)$ is the average force per linkage on a stationary actomyosin cortical network. The best estimate of the dynein off rate is $k_{off} \sim 1 \text{ s}$, so that the mean motor force is essentially the same as the maximum force, $f_0 \simeq f_{max}$. The force per unit length of the microtubule, \mathbf{K} , can then be obtained by multiplying Equation D-6 by the density of dynein linkages per unit length, ρ ,

$$\mathbf{K} = \rho \langle \mathbf{f} \rangle = \rho f_0 \left(1 - \frac{\mathbf{v} \cdot \mathbf{t}}{v_0} \right) \mathbf{t} - \rho \gamma \mathbf{v} \cdot (\mathbf{1} - \mathbf{t} \mathbf{t}) \quad (\text{D-7})$$

where $\gamma = \kappa / k_{off}$ is the friction coefficient for lateral motion per dynein linkage.

Simulation Methods.

The numerical simulations are based on an algorithm for integrating the equations of motion of an elastic filament (175). In addition, we include length changes in the microtubule to incorporate polymerization and depolymerization of the microtubules. The length of the microtubule is taken to be a continuous variable, described by a stochastic differential equation that includes switches to catastrophe (depolymerization) and recovery (polymerization). The parameters are taken from experimental

measurements (116, 117): $v_{pol} = 0.1 \mu\text{m s}^{-1}$, $v_{depol} = 0.3 \mu\text{m s}^{-1}$, $k_{cat} = 0.05\text{s}^{-1}$, and $k_{rec} = 0.2\text{s}^{-1}$. Segments are added or removed from each microtubule during the simulation, according to the calculated changes in length. The model for dynein motors, Equation D-7, is included in the force balance that describes the evolution of each microtubule, Equation 4-2, which leads to an expression for the microtubule velocity in terms of the coordinates. The conformation of each microtubule is then updated with a time step of the order of $1 \mu\text{s}$.

The dynamics of the centrosome were simulated by distributing microtubules around the centrosome with a uniform distribution of angles; the microtubules are coupled to the centrosome by stiff springs. In the experiments on animal cells many of the microtubules are observed to get pinned when they reach the cell boundary; typically these microtubules buckle as shown in Figure 4-10. However it is sometimes observed that the microtubules slide along the cell boundary as shown in Figure 4-10A and occasionally microtubules apparently stop growing (Figure 4-10B). We include the possibility of microtubule pinning by an angle dependent rate $k \cos \theta$, where θ is the angle between the tangent at the tip of the microtubule and the normal to the cell surface. We take the rate constant $k = 0.2 \text{ s}^{-1}$ and the unpinning rate as k . With this choice of kinetics about 2/3 of the microtubules are pinned at any one time, similar to the experimental observations. The remaining microtubules continue to polymerize as their tips slide along the cell surface. We also reduce the growth rate of pinned microtubules by 50% in comparison with the free microtubules to account for stalling in the polymerization kinetics. However, in simulations of *in vitro* microtubule growth, we

allowed the microtubules to slide freely along the surface, mimicking the effect of the smooth glass walls.

Simulations of Microtubule Buckling

The simulation illustrated in Figure 4-8B models a minus-ended microtubule after severing, corresponding to the experiment shown in Figure 4-3A. The microtubule is pinned at the plus end, but a similar result would follow from the frictional resistance of an additional segment out of the field of view. The simulation shows a small initial buckle under the action of a continuous distribution of dynein motors. We observe a growth in the amplitude of the buckle with time, and a gradual pushing of the buckle towards the plus end. The simulation reproduces the key features of the experiment shown in Figure 4-3A and on a similar time scale. Variations in the assumed dynein off rate (k_{off}) would be reflected by corresponding changes in the predicted timescale.

Simulations of Centrosome Centering

Simulations of centrosome centering are illustrated in Figure 4-9C and D. We compare the dynamics of a radial array of polymerizing microtubules with and without the forces and friction from the dynein motors. The parameters (motor density, motor friction, and friction from the background fluid) are the same as in the single microtubule simulations. Simulations with motors show that microtubules are heavily buckled near the cell periphery whereas in the absence of motors the wavelengths of the buckled microtubules are much longer. With dynein motors pulling the microtubules, the centrosome centers with a time constant of about 10 min but simulations without motors suggest that polymerization forces are unable to center the centrosome under *in vivo* conditions. The centrosome remains essentially in place for the duration of the simulation (100 min).

Figure 4-1 compares simulations of centrosome centering with experimental measurements of the fluctuations in centrosome position. The microtubule network develops by polymerization from a radial array of stubs (Figure 4-9C) during the first 5 min of the simulation. After the microtubule network has filled the cell, an initially off-center centrosome moves towards the center with a relaxation time of approximately 12 min (time to decay to $1/e$ of its initial displacement). The relaxation time in animal cells, measured from the autocorrelation function of fluctuations in centrosome position was about 8 min, with a standard deviation of 4 min (determined from 14 trajectories of 1-2 hours each).

We have also simulated *in vitro* centering of an centrosome to compare with data in Ref. (77). In that work it was shown that polymerizing forces could center the centrosome by pushing from the cell boundary. The key changes in the simulation parameters were the cell size (12 μm) and the viscosity of the background fluid (10^{-3} Pa s). In addition we eliminated microtubule pinning at the cell boundaries to model the slippage along the glass wall. The polymerization kinetics were tuned to produce microtubules with average lengths of approximately 20 and 40 μm , again to correspond to the conditions of the experiments. The simulations reproduce the key features of the experiments (77); with the shorter (20 μm) microtubules the centrosome centers rapidly but with the longer (40 μm) microtubules it drifts to an off center location. It can be seen that the longer microtubules buckle significantly and therefore exert much less force than the shorter ones, which remain more or less straight. Under *in vivo* conditions, with a larger cell (40 μm) and a larger viscosity of the background fluid (> 1 Pa s), polymerization forces are much too small to center the centrosome.

It is interesting to compare the buckling of the microtubules with the *in vivo* simulation without motors. Under *in vivo* conditions the microtubules buckle into higher order modes because the friction is so large that they do not relax to the minimum energy state before the next segment polymerizes, whereas under *in vitro* conditions, with a much smaller viscosity, the microtubules buckle into the lowest order mode.

Centrosome Relaxation Time

The centrosome relaxation time can be estimated based on a model of linear rigid microtubules. Assuming each microtubule is pinned at the cell periphery and the centrosome is moving with a velocity \mathbf{v}_c , the lateral velocity of the microtubule segment at a distance l from the periphery is $(\mathbf{1} - \mathbf{t}\mathbf{t}) \cdot \mathbf{v}_c l/L$, where L is the (time-dependent) contour length of the microtubule; the tangential velocity is assumed to be constant since the microtubule is rigid. The force exerted on the centrosome from a single microtubule is then found by integrating over the contour length,

$$\mathbf{F}_i = \rho f_0 L_i \mathbf{t}_i \left(1 - \frac{\mathbf{v}_c \cdot \mathbf{t}_i}{v_0}\right) - \frac{\rho \gamma L_i}{2} \mathbf{v}_c \cdot (\mathbf{1} - \mathbf{t}_i \mathbf{t}_i) \quad (\text{D-8})$$

Balancing the forces on the centrosome gives the velocity,

$$\mathbf{v}_c = \left\{ \frac{\sum_i f_0 L_i \mathbf{t}_i}{\sum_i \left(\frac{f_0 L_i}{v_0} \mathbf{t}_i \mathbf{t}_i + \frac{\gamma L_i}{2} (\mathbf{1} - \mathbf{t}_i \mathbf{t}_i) \right)} \right\} \quad (\text{D-9})$$

It follows from Equation D-9 that, when dynein-motor forces dominate, the centrosome velocity is independent of dynein density.

The time scale for centrosome centering can be estimated by considering a displacement of the centrosome from the cell center by a small distance ε along the x -axis. The force balance in the x direction is

$$\langle F_x \rangle_\theta = \rho f_0 \left\{ \langle L(\theta) \cos \theta \rangle_\theta - \frac{v_{c,x}}{v_0} \langle L(\theta) \cos^2 \theta \rangle_\theta \right\} - \frac{\rho \gamma v_{c,x}}{2} \langle L(\theta) \sin^2 \theta \rangle_\theta \quad (\text{D-10})$$

where $\langle \dots \rangle_\theta$ represents the mean over a uniform angular distribution and $L(\theta)$ is the length of the microtubule spanning the distance between the centrosome and the cell periphery.

For small displacements from the center of a circular cell, $L(\theta) \simeq R - \varepsilon \cos \theta$.

Evaluating the moments of L in Equation D-10 to lowest order in ε/R ,

$$\langle F_x \rangle_\theta = \rho f_0 \left\{ -\frac{1}{2} \varepsilon - \frac{v_{c,x}}{v_0} \left(\frac{R}{2} \right) \right\} - \frac{\rho \gamma v_{c,x}}{2} \left(\frac{R}{2} \right) = 0 \quad (\text{D-11})$$

Equation D-11 can be solved for $v_{c,x}$ to yield a linear relaxation equation for the displacement ε in terms of its time derivative $d\varepsilon/dt = v_{c,x} = -\varepsilon/\tau_c$, where the relaxation time for centrosome centering is given by

$$\tau_c = R \left(\frac{1}{v_0} + \frac{\gamma}{2f_0} \right) \quad (\text{D-12})$$

Significantly, τ_c , which is the characteristic time for the centrosome to center, is predicted to depend only on the cell size and molecular parameters, not the number of microtubules. Different cell shapes only affect this result to a numerical pre-factor. For the parameters we have chosen, $\tau_c = 24$ min, assuming a circular cell with the same area as the BCE cells.

APPENDIX E
 λ FOR BLEACHING OF FREE PROTEIN IN THE CYTOPLASM

The photobleaching rate constant λ will in general be different for the cytoplasm compared to a confined structure like the focal adhesion. This is because the confocal slice volume V_c in which the majority of bleaching occurs does not encompass the whole cytoplasm, while it can encompass confined structures like the focal adhesion (~100 nm compared to a vertical cross-section of the confocal plane of around 600 nm). Assuming that the cytoplasm is well-mixed, and that bleaching occurs in a smaller volume corresponding to the confocal slice volume, a balance on the free molecules during image capture yields

$$\frac{d(CV_{cyto})}{dt} = -\lambda_m CV_c \Rightarrow \frac{dC}{dt} = -\frac{\lambda_m V_c}{V_{cyto}} C \quad (E-1)$$

where λ_m is the photobleaching rate constant (s^{-1}) for the free protein molecules and V_{cyto} is the volume of the cytoplasm. Comparing this to equation (1) yields the effective bleaching constant for the cytoplasm: $\lambda \equiv \frac{\lambda_m V_c}{V_{cyto}}$. The effective bleaching rate constant is small for a large volume such as the cytoplasm due to the small value of V_c / V_{cyto} . For a confined structure like the focal adhesion or a promoter array in the nucleus, the rate constant will be larger as the volume of the structure is small (or comparable) compared to the confocal slice volume. Another consideration is the fact that free molecules rapidly diffuse in and out of the confocal slice, resulting in less bleaching than would occur in a confined structure. Based on these considerations, the bleaching functions are assumed to be different for the free and bound species (g_1 and g_1).

APPENDIX F MATLAB CODE FOR FRAP MODELING AND SIMULATION

These are Matlab programs for the modeling discussed in Chapter 5. All the notations are consistent through different programs unless otherwise specified.

Simulation of Bleaching Dynamics in Image Capture Process

These are the programs to generate Figure 5-1. Figure 5-2 used similar program.

Comparison of Observed Dynamics and Actual Dynamics

```
%Start of FRAPfig1A.m
clear all
close all
clc

m=12;%Number of frames
a=0.9;%Value of alpha
lamdaw2=0.2;%Value of lamda*omega
interval=5;%Time intervals between frames
omega=0.5;%Value of omega

%observed dynmaics
fw2=(exp(lamdaw2)-1)/lamdaw2;%function for intensity averaging due to image
capture process
g2=exp(-lamdaw2);%function for bleaching due to image capture
koff=0.2;
tau=interval; % in seconds, this is the time between frames
t=[0:1:m-1];
C(1) = a*fw2;
for i = 2:m
    C(i)= a*g2^(i-1)*fw2;
end
figure(1)
plot(t(2:m),C(2:m),'*k','markersize',12)

%real dynamics
scale=tau/omega;
tr=[0:0.5:(m-1)*tau];
Cr(1)=a;
for i=1:m-1;
    for k=((i-1)*scale+2):((i-1)*scale+10);
        Cr(k)=Cr((i-1)*scale+1);
    end
    j=i*scale+1;
    Cr(j)=Cr(j-1)*g2;
end
hold on
plot(tr/tau,Cr,':k','markersize',10)
hold on
for i=1:m-1;
    plot(tr((i-1)*scale+10)/tau,Cr((i-1)*scale+10),'ok','markersize',10)
```

```
end
```

Modeling of Normalized Bleaching Dynamics

```
%Start of FRAPfig1B.m
clear all
close all
clc

m=12;
a=1;%alpha starts at 1 because of normalization
lamdaw2=0.2;
interval=5;
omega=0.5;

%normalized observed intensity
fw2=(exp(lamdaw2)-1)/lamdaw2;
g2=exp(-lamdaw2);
koff=0.2;
tau=interval;
t=[0:1:m-1];
C(1)=1;
for i=2:m
    C(i)=C(1)*g2^(i-1);
end
figure(1)
plot(t(2:m),C(2:m),'*k','markersize',12)

%normalized real dynamics
scale=tau/omega;
tr=[0:0.5:(m-1)*tau];
Cr(1)=1;
for i=1:m-1;
    for k=((i-1)*scale+2):((i-1)*scale+10);
        Cr(k)=Cr((i-1)*scale+1);
    end
    j=i*scale+1;
    Cr(j)=Cr(j-1)*g2;
end
hold on
plot(tr/tau,Cr,':k','markersize',10)
hold on
for i=1:m-1;
    plot(tr((i-1)*scale+10)/tau,Cr((i-1)*scale+10),'ok','markersize',10)
end
```

Simulation of FRAP

This is the program used in Figure 5-3. The program can be adjusted to simulate different $\lambda_1\omega$, $\lambda_2\omega$ and τ_{OFF} and immobile fraction β . Here we use τ_{OFF} as an example

```
%Start of FRAPfig3A.m
clear all
close all
clc

m=11;
a=0.4;
b=0.3;%Value for immobile fraction
lamdaw1=0.2;%Value of lamda*omega at the focal adhesion
lamdaw2=0.000000000001;%Value of lamda*omega for the free protein

C0=1;%this is normalized intensity before bleaching
alpha=a;
imfrac=b;
beta=[1-imfrac imfrac];%mobile and immobile fraction
g1=exp(-lamdaw1);%bleaching function for focal adhesion
g2=exp(-lamdaw2);%bleaching function for free protein
ktau=1;%Value of tau*koff
frac=0;%ratio of koff for mobile and immobile, it's zero for completely
immobile
Ktau=[ktau ktau*frac];
t=0:1:m-1;
Cm(1)=alpha*beta(1);%normalized intensity of the first frame after bleaching
for mobile fraction
Ci(1)=alpha*beta(2);%normalized intensity of the first frame after bleaching
for immobile fraction
for i = 2:m
    Cm(i)= C0*beta(1)*(g2^(i-2)-(g2^(i-2)-Cm(i-1)/beta(1))*exp(-
Ktau(1)))*g1;%normalized intensity of mobile fraction
    Ci(i)= C0*beta(2)*(g2^(i-2)-(g2^(i-2)-Ci(i-1)/beta(2))*exp(-
Ktau(2)))*g1;%normalized intensity of immobile fraction
end
C=Cm+Ci;%normalized total fluorescence
figure(1)
plot(t,C,'-k','MarkerSize',10)
```

Model Fitting of FRAP

These are the programs used in model fitting in Figure 5-4.

Define Fitting Function of FRAP Model

This is for focal adhesion FRAP fitting.

```

%Start of FA3T3FRAPpara.m
function sse=FA3T3FRAPpara(param,input1,input2,input3,input4,input5,data1)
C0=input1;%define input parameter 1 to 5
alpha= input2;
L=input3;
tau=input4;
imfrac=input5;
lamdaw1=param(1); % define parameters 1 to 5 that need to be estimated by
fitting
lamdaw2=param(2);
g1=exp(-lamdaw1);
g2=exp(-lamdaw2);
koff=param(3);
beta=[1-imfrac imfrac];
Cm(1)=alpha*beta(1);
Ci(1)=alpha*beta(2);
for i = 2:L
    Cm(i)= C0*beta(1)*(g2^(i-2)-(g2^(i-2)-Cm(i-1)/beta(1))*exp(-tau*koff))*g1;
    Ci(i)= C0*beta(2)*Ci(i-1)/beta(2)*g1;
end
C=Cm+Ci;
Error1=C-data1;
sse=sum(Error1.^2);% When curvefitting, a typical quantity to minimize is the
sum of squares error

```

Fitting Focal Adhesion FRAP Experiment Data to the Model

```

%Start of FA3T3FRAPfitting
clear all
close all
clc

load 3T3FRAP020212cell116.mat%load data from experiment
C0=1;
%for FRAP without bleaching
intra=intreca'/C0a;%normalize intensity by deviding experiment data by the
intensity before bleaching
t=time;%time series of the experiment
alpha=intra(1);
L=length(intra);%number of frames in the experiment
tau=t(2)-t(1);%time interval in the experiment
imfrac=im;%iimmobile fraction calculated from independent experiment of the
same focal adhesion
Starting=[0.1, 0.1, exp(-tau*0.2)];%initial guess for the fitting
options=optimset('Display','iter');
Estimates=fminsearch(@FA3T3FRAPpara,Starting,options,C0,alpha,L,tau,imfrac,in
tra);%call fitting function "FA3T3FRAPpara.m"

%read values from fitting and plot the result
Cm(1)=alpha*(1-imfrac);
Ci(1)=alpha*imfrac;
g1=exp(-Estimates(1));
g2=exp(-Estimates(2));
for i=2:L;

```

```

    Cm(i)=C0*(1-imfrac)*(g2^(i-2)-(g2^(i-2)-Cm(i-1)/(1-imfrac))*exp(-
tau*Estimates(3)))*g1;
    Ci(i)=C0*imfrac*Ci(i-1)/imfrac*g1;
end
lamdaw1a=Estimates(1);
lamdaw2a=Estimates(2);
g1a=g1;
g2a=g2;
koffa=Estimates(3);
Ca=Cm+Ci;
figure(1)
plot(t+5,intra,'*k')
hold on
plot(t+5,Ca,'r')
hold on
plot(t(1),C0,'^k','markersize',10)

```

Define Fitting Function for Free Molecule Intensity

This is for bleaching of free protein fitting.

```

%Start of bleachpara.m
function sse=bleachpara(params,input1,input2,data1)
intf=input1;
L=input2;
lamdaw2=params(1);
g2=exp(-lamdaw2);
Cf(1)=intf(1);
for i=2:L;
    Cf(i)=Cf(1)*g2^(i-1);
end
error=Cf-data1;
sse=sum(error.^2);

```

Fitting Free Molecule Intensity in Focal Adhesion FRAP Experiments

```

%Start of FRAPbleachingfitting.m
clear all
close all
clc

load 3T3FRAP020212cell116.mat
intf=intb'/intb;
L=length(intf);
t=time;
tau=t(2)-t(1);
Starting=rand(1,1);
options=optimset('Display','iter');
Estimates=fminsearch(@bleachpara,Starting,options,intf,L,intf);

lamdaw2=Estimates(1);
g2=exp(-Estimates(1));
Cf(1)=intf(1);
for i=2:L;

```

```

    Cf(i)=Cf(1)*g2^(i-1);
end
plot(t,intf,'*')
hold on
plot(t,Cf,'r')

```

Simulation of FRAP with Multiple Time Intervals

This is the program used for simulation in Figure 5-6.

```

%Start of MultiTausimu.m
clear all
close all
clc

m=10;
a=0.2;
lamdaw1=0.2;
lamdaw2=0.000000000001;
interval=2;
omega=0.2;

C0=1;
alpha=a;
g1=exp(-lamdaw1);
g2=exp(-lamdaw2);
koff=0.2;
taul=interval;%the first time interval
t1=0:m;
C(1)=alpha;
alpha(1)=alpha;
for i=2:m+1
    C(i)= C0*(g2^(i-2)-(g2^(i-2)-alpha(i-1))*exp(-(taul-omega)*koff))*g1;
    alpha(i)=(g2^(i-2)-(g2^(i-2)-alpha(i-1))*exp(-(taul-omega)*koff))*g1;
end

scale=taul/omega;
tr1=0:omega:m*taul;
Cr(1)=C(1);
ralpha(1)=a;
for i=1:m;
    for k=((i-1)*scale+2):(i*scale);
        Cr(k)=C0*(1-(1-ralpha(i))*exp(-(tr1(k)-(i-1)*taul)*koff));
    end
    j=i*scale+1;
    Cr(j)=Cr(j-1)*exp(-lamdaw1);
    ralpha(i+1)=Cr(j)/C0;
end

tau2=2*interval;%the second time interval
t2=m+1:2*m;
alpha(m+1)=C(m+1)/C0;

```

```

for i=m+2:2*m+1
    C(i)= C0*(g2^(i-2)-(g2^(i-2)-alpha(i-1))*exp(-(tau2-omega)*koff))*g1;
    alpha(i)=(g2^(i-2)-(g2^(i-2)-alpha(i-1))*exp(-(tau2-omega)*koff))*g1;
end

scale2=tau2/omega;
tr2=(m*tau1+omega):omega:(m*tau1+m*tau2);
ralpha(m+1)=alpha(m+1);
for i=m+1:2*m;
    for k=((i-m-1)*scale2+2):((i-m)*scale2);
        Cr(m*scale+k)=C0*(1-(1-ralpha(i))*exp(-(tr2(k-1)-m*tau1-(i-m-1)*tau2)*koff));
    end
    j=m*scale+(i-m)*scale2+1;
    Cr(j)=Cr(j-1)*exp(-lamdaw1);
    ralpha(i+1)=Cr(j)/C0;
end

tau3=3*interval;%the third time interval
t3=2*m+1:3*m;
alpha(2*m+1)=C(2*m+1)/C0;
for i=2*m+2:3*m+1
    C(i)= C0*(g2^(i-2)-(g2^(i-2)-alpha(i-1))*exp(-(tau3-omega)*koff))*g1;
    alpha(i)=(g2^(i-2)-(g2^(i-2)-alpha(i-1))*exp(-(tau3-omega)*koff))*g1;
end

scale3=tau3/omega;
tr3=(m*tau1+m*tau2+omega):omega:(m*tau1+m*tau2+m*tau3);
ralpha(2*m+1)=alpha(2*m);
for i=2*m+1:3*m;
    for k=((i-2*m-1)*scale3+2):((i-2*m)*scale3);
        Cr(m*scale+m*scale2+k)=C0*(1-(1-ralpha(i))*exp(-(tr3(k-1)-m*tau1-m*tau2-(i-2*m-1)*tau3)*koff));
    end
    j=m*scale+m*scale2+(i-2*m)*scale3+1;
    Cr(j)=Cr(j-1)*exp(-lamdaw1);
    ralpha(i+1)=Cr(j)/C0;
end

ts=1:m;
t=[tau1*t1 tau1*m+tau2*ts tau1*m+tau2*m+tau3*ts];
tr=[tr1 tr2 tr3];
plot(t+5,C,'-k','markersize',12)
hold on
plot(tr+5,Cr,':k')
hold on
plot(t(1),C0,'^k','markersize',10)

```

LIST OF REFERENCES

1. Jaalouk, D. E., and J. Lammerding. 2009. Mechanotransduction gone awry. *Nat Rev Mol Cell Biol.* 10:63-73.
2. Starr, D. A. 2009. A nuclear-envelope bridge positions nuclei and moves chromosomes. *J Cell Sci.* 122:577-586.
3. Zhang, X., R. Xu, B. Zhu, X. Yang, X. Ding, S. Duan, T. Xu, Y. Zhuang, and M. Han. 2007. Syne-1 and Syne-2 play crucial roles in myonuclear anchorage and motor neuron innervation. *Development.* 134:901-908.
4. Wang, N., J. D. Tytell, and D. E. Ingber. 2009. Mechanotransduction at a distance: mechanically coupling the extracellular matrix with the nucleus. *Nat Rev Mol Cell Biol.* 10:75-82.
5. Gomes, E. R., S. Jani, and G. G. Gundersen. 2005. Nuclear movement regulated by Cdc42, MRCK, myosin, and actin flow establishes MTOC polarization in migrating cells. *Cell.* 121:451-463.
6. Baye, L. M., and B. A. Link. 2008. Nuclear migration during retinal development. *Brain Res.* 1192:29-36.
7. Stearns, T. 1997. Motoring to the finish: kinesin and dynein work together to orient the yeast mitotic spindle. *J Cell Biol.* 138:957-960.
8. Gros-Louis, F., N. Dupre, P. Dion, M. A. Fox, S. Laurent, S. Verreault, J. R. Sanes, J. P. Bouchard, and G. A. Rouleau. 2007. Mutations in SYNE1 lead to a newly discovered form of autosomal recessive cerebellar ataxia. *Nat Genet.* 39:80-85.
9. Burke, B., and C. L. Stewart. 2002. Life at the edge: the nuclear envelope and human disease. *Nat Rev Mol Cell Biol.* 3:575-585.
10. Mattout, A., T. Dechat, S. A. Adam, R. D. Goldman, and Y. Gruenbaum. 2006. Nuclear lamins, diseases and aging. *Curr Opin Cell Biol.* 18:335-341.
11. Warren, D. T., Q. Zhang, P. L. Weissberg, and C. M. Shanahan. 2005. Nesprins: intracellular scaffolds that maintain cell architecture and coordinate cell function? *Expert Rev Mol Med.* 7:1-15.
12. Levy, J. R., and E. L. Holzbaur. 2008. Dynein drives nuclear rotation during forward progression of motile fibroblasts. *J Cell Sci.* 121:3187-3195.
13. Zhou, K., M. M. Rolls, D. H. Hall, C. J. Malone, and W. Hanna-Rose. 2009. A ZYG-12-dynein interaction at the nuclear envelope defines cytoskeletal architecture in the *C. elegans* gonad. *J Cell Biol.* 186:229-241.

14. Fridolfsson, H. N., N. Ly, M. Meyerzon, and D. A. Starr. 2010. UNC-83 coordinates kinesin-1 and dynein activities at the nuclear envelope during nuclear migration. *Dev Biol.* 338:237-250.
15. Crisp, M., Q. Liu, K. Roux, J. B. Rattner, C. Shanahan, B. Burke, P. D. Stahl, and D. Hodzic. 2006. Coupling of the nucleus and cytoplasm: role of the LINC complex. *J Cell Biol.* 172:41-53.
16. Starr, D. A. 2011. Watching nuclei move: Insights into how kinesin-1 and dynein function together. *Bioarchitecture.* 1:9-13.
17. Worman, H. J., and G. G. Gundersen. 2006. Here come the SUNs: a nucleocytoskeletal missing link. *Trends Cell Biol.* 16:67-69.
18. Starr, D. A., and J. A. Fischer. 2005. KASH 'n Karry: the KASH domain family of cargo-specific cytoskeletal adaptor proteins. *Bioessays.* 27:1136-1146.
19. Wilhelmsen, K., M. Ketema, H. Truong, and A. Sonnenberg. 2006. KASH-domain proteins in nuclear migration, anchorage and other processes. *J Cell Sci.* 119:5021-5029.
20. Tzur, Y. B., K. L. Wilson, and Y. Gruenbaum. 2006. SUN-domain proteins: 'Velcro' that links the nucleoskeleton to the cytoskeleton. *Nat Rev Mol Cell Biol.* 7:782-788.
21. Zhang, Q., J. N. Skepper, F. Yang, J. D. Davies, L. Hegyi, R. G. Roberts, P. L. Weissberg, J. A. Ellis, and C. M. Shanahan. 2001. Nesprins: a novel family of spectrin-repeat-containing proteins that localize to the nuclear membrane in multiple tissues. *J Cell Sci.* 114:4485-4498.
22. Padmakumar, V. C., T. Libotte, W. Lu, H. Zaim, S. Abraham, A. A. Noegel, J. Gotzmann, R. Foisner, and I. Karakesisoglou. 2005. The inner nuclear membrane protein Sun1 mediates the anchorage of Nesprin-2 to the nuclear envelope. *J Cell Sci.* 118:3419-3430.
23. Zhang, Q., C. D. Ragnauth, J. N. Skepper, N. F. Worth, D. T. Warren, R. G. Roberts, P. L. Weissberg, J. A. Ellis, and C. M. Shanahan. 2005. Nesprin-2 is a multi-isomeric protein that binds lamin and emerin at the nuclear envelope and forms a subcellular network in skeletal muscle. *J Cell Sci.* 118:673-687.
24. Hale, C. M., A. L. Shrestha, S. B. Khatau, P. J. Stewart-Hutchinson, L. Hernandez, C. L. Stewart, D. Hodzic, and D. Wirtz. 2008. Dysfunctional connections between the nucleus and the actin and microtubule networks in laminopathic models. *Biophys J.* 95:5462-5475.

25. Houben, F., C. H. Willems, I. L. Declercq, K. Hochstenbach, M. A. Kamps, L. H. Snoeckx, F. C. Ramaekers, and J. L. Broers. 2009. Disturbed nuclear orientation and cellular migration in A-type lamin deficient cells. *Biochim Biophys Acta*. 1793:312-324.
26. Huxley, H. E. 1957. The double array of filaments in cross-striated muscle. *J Biophys Biochem Cytol*. 3:631-648.
27. Burkhardt, J. K., C. J. Echeverri, T. Nilsson, and R. B. Vallee. 1997. Overexpression of the dynamitin (p50) subunit of the dynactin complex disrupts dynein-dependent maintenance of membrane organelle distribution. *J Cell Biol*. 139:469-484.
28. Cortesy-Theulaz, I., A. Pauloin, and S. R. Pfeffer. 1992. Cytoplasmic dynein participates in the centrosomal localization of the Golgi complex. *J Cell Biol*. 118:1333-1345.
29. Ebner, A., R. Godemann, K. Stamer, S. Illenberger, B. Trinczek, and E. Mandelkow. 1998. Overexpression of tau protein inhibits kinesin-dependent trafficking of vesicles, mitochondria, and endoplasmic reticulum: implications for Alzheimer's disease. *J Cell Biol*. 143:777-794.
30. Pilling, A. D., D. Horiuchi, C. M. Lively, and W. M. Saxton. 2006. Kinesin-1 and Dynein are the primary motors for fast transport of mitochondria in Drosophila motor axons. *Mol Biol Cell*. 17:2057-2068.
31. Roux, K. J., M. L. Crisp, Q. Liu, D. Kim, S. Kozlov, C. L. Stewart, and B. Burke. 2009. Nesprin 4 is an outer nuclear membrane protein that can induce kinesin-mediated cell polarization. *Proc Natl Acad Sci U S A*. 106:2194-2199.
32. Tsai, J. W., K. H. Bremner, and R. B. Vallee. 2007. Dual subcellular roles for LIS1 and dynein in radial neuronal migration in live brain tissue. *Nat Neurosci*. 10:970-979.
33. Fridolfsson, H. N., and D. A. Starr. 2010. Kinesin-1 and dynein at the nuclear envelope mediate the bidirectional migrations of nuclei. *J Cell Biol*. 191:115-128.
34. Lye, R. J., M. E. Porter, J. M. Scholey, and J. R. McIntosh. 1987. Identification of a microtubule-based cytoplasmic motor in the nematode *C. elegans*. *Cell*. 51:309-318.
35. Paschal, B. M., S. M. King, A. G. Moss, C. A. Collins, R. B. Vallee, and G. B. Witman. 1987. Isolated flagellar outer arm dynein translocates brain microtubules in vitro. *Nature*. 330:672-674.

36. Paschal, B. M., H. S. Shpetner, and R. B. Vallee. 1987. MAP 1C is a microtubule-activated ATPase which translocates microtubules in vitro and has dynein-like properties. *J Cell Biol.* 105:1273-1282.
37. Vale, R. D. 2003. The molecular motor toolbox for intracellular transport. *Cell.* 112:467-480.
38. Asai, D. J., and M. P. Koonce. 2001. The dynein heavy chain: structure, mechanics and evolution. *Trends Cell Biol.* 11:196-202.
39. Gennerich, A., and R. D. Vale. 2009. Walking the walk: how kinesin and dynein coordinate their steps. *Curr Opin Cell Biol.* 21:59-67.
40. Reck-Peterson, S. L., A. Yildiz, A. P. Carter, A. Gennerich, N. Zhang, and R. D. Vale. 2006. Single-molecule analysis of dynein processivity and stepping behavior. *Cell.* 126:335-348.
41. Mosley-Bishop, K. L., Q. Li, L. Patterson, and J. A. Fischer. 1999. Molecular analysis of the klarsicht gene and its role in nuclear migration within differentiating cells of the Drosophila eye. *Curr Biol.* 9:1211-1220.
42. Kracklauer, M. P., S. M. Banks, X. Xie, Y. Wu, and J. A. Fischer. 2007. Drosophila klaroid encodes a SUN domain protein required for Klarsicht localization to the nuclear envelope and nuclear migration in the eye. *Fly (Austin).* 1:75-85.
43. Malone, C. J., L. Misner, N. Le Bot, M. C. Tsai, J. M. Campbell, J. Ahringer, and J. G. White. 2003. The C. elegans hook protein, ZYG-12, mediates the essential attachment between the centrosome and nucleus. *Cell.* 115:825-836.
44. Albrecht-Buehler, G. 1984. Movement of Nucleus and Centrosphere in 3T3 Cells. In *Cancer Cells: The transformed phenotype.* A. J. Levine, G. F. V. Woude, W. C. Toop, and J. D. Watson, editors. Cold Spring Harbor Laboratory, Newyork. 87~96.
45. Allen, V. W., and D. L. Kropf. 1992. Nuclear rotation and lineage specification in Pelvetia embryos. *Development.* 11.
46. Ji, J. Y., R. T. Lee, L. Vergnes, L. G. Fong, C. L. Stewart, K. Reue, S. G. Young, Q. Zhang, C. M. Shanahan, and J. Lammerding. 2007. Cell nuclei spin in the absence of lamin b1. *J Biol Chem.* 282:20015-20026.
47. Pomerat, C. M. 1953. Rotating nuclei in tissue cultures of adult human nasal mucosa. *Exp Cell Res.* 5:191-196.

48. Lee, J. S., M. I. Chang, Y. Tseng, and D. Wirtz. 2005. Cdc42 mediates nucleus movement and MTOC polarization in Swiss 3T3 fibroblasts under mechanical shear stress. *Mol Biol Cell*. 16:871-880.
49. Gerashchenko, M. V., I. S. Chernouvanenko, M. V. Moldaver, and A. A. Minin. 2009. Dynein is a motor for nuclear rotation while vimentin IFs is a "brake". *Cell Biol Int*. 33:1057-1064.
50. Friedl, P., K. Wolf, and J. Lammerding. 2011. Nuclear mechanics during cell migration. *Curr Opin Cell Biol*. 23:55-64.
51. Vicente-Manzanares, M., K. Newell-Litwa, A. I. Bachir, L. A. Whitmore, and A. R. Horwitz. 2011. Myosin IIA/IIB restrict adhesive and protrusive signaling to generate front-back polarity in migrating cells. *J Cell Biol*. 193:381-396.
52. Howard, J. 2001. *Mechanics of Motor Proteins and the Cytoskeleton*. Sinauer, Sunderland, MA.
53. Huxley, A. F. 1957. Muscle structure and theories of contraction. *Prog Biophys Biophys Chem*. 7:255-318.
54. Huxley, A. F., and R. Niedergerke. 1954. Structural changes in muscle during contraction; interference microscopy of living muscle fibres. *Nature*. 173:971-973.
55. Huxley, H., and J. Hanson. 1954. Changes in the cross-striations of muscle during contraction and stretch and their structural interpretation. *Nature*. 173:973-976.
56. Folker, E. S., C. Ostlund, G. W. Luxton, H. J. Worman, and G. G. Gundersen. 2011. Lamin A variants that cause striated muscle disease are defective in anchoring transmembrane actin-associated nuclear lines for nuclear movement. *Proc Natl Acad Sci U S A*. 108:131-136.
57. Luxton, G. W., E. R. Gomes, E. S. Folker, E. Vintinner, and G. G. Gundersen. 2010. Linear arrays of nuclear envelope proteins harness retrograde actin flow for nuclear movement. *Science*. 329:956-959.
58. Martini, F. J., and M. Valdeolmillos. 2010. Actomyosin contraction at the cell rear drives nuclear translocation in migrating cortical interneurons. *J Neurosci*. 30:8660-8670.
59. Chancellor, T. J., J. Lee, C. K. Thodeti, and T. Lele. 2010. Actomyosin tension exerted on the nucleus through nesprin-1 connections influences endothelial cell adhesion, migration, and cyclic strain-induced reorientation. *Biophys J*. 99:115-123.

60. Sims, J. R., S. Karp, and D. E. Ingber. 1992. Altering the cellular mechanical force balance results in integrated changes in cell, cytoskeletal and nuclear shape. *J Cell Sci.* 103 (Pt 4):1215-1222.
61. Maniotis, A. J., C. S. Chen, and D. E. Ingber. 1997. Demonstration of mechanical connections between integrins, cytoskeletal filaments, and nucleoplasm that stabilize nuclear structure. *Proc Natl Acad Sci U S A.* 94:849-854.
62. Buxboim, A., I. L. Ivanovska, and D. E. Discher. 2010. Matrix elasticity, cytoskeletal forces and physics of the nucleus: how deeply do cells 'feel' outside and in? *J Cell Sci.* 123:297-308.
63. Wu, Y. I., D. Frey, O. I. Lungu, A. Jaehrig, I. Schlichting, B. Kuhlman, and K. M. Hahn. 2009. A genetically encoded photoactivatable Rac controls the motility of living cells. *Nature.* 461:104-108.
64. Tassin, A. M., and M. Bornens. 1999. Centrosome structure and microtubule nucleation in animal cells. *Biol Cell.* 91:343-354.
65. Vernos, I., and E. Karsenti. 1996. Motors involved in spindle assembly and chromosome segregation. *Curr Opin Cell Biol.* 8:4-9.
66. Waters, J. C., R. W. Cole, and C. L. Rieder. 1993. The force-producing mechanism for centrosome separation during spindle formation in vertebrates is intrinsic to each aster. *J Cell Biol.* 122:361-372.
67. Cole, N. B., and J. Lippincott-Schwartz. 1995. Organization of organelles and membrane traffic by microtubules. *Curr Opin Cell Biol.* 7:55-64.
68. Danowski, B. A., A. Khodjakov, and P. Wadsworth. 2001. Centrosome behavior in motile HGF-treated PtK2 cells expressing GFP-gamma tubulin. *Cell Motil Cytoskeleton.* 50:59-68.
69. Savoian, M. S., and C. L. Rieder. 2002. Mitosis in primary cultures of *Drosophila melanogaster* larval neuroblasts. *J Cell Sci.* 115:3061-3072.
70. Verstraeten, V. L., L. A. Peckham, M. Olive, B. C. Capell, F. S. Collins, E. G. Nabel, S. G. Young, L. G. Fong, and J. Lammerding. 2011. Protein farnesylation inhibitors cause donut-shaped cell nuclei attributable to a centrosome separation defect. *Proc Natl Acad Sci U S A.* 108:4997-5002.
71. Salmon, W. C., M. C. Adams, and C. M. Waterman-Storer. 2002. Dual-wavelength fluorescent speckle microscopy reveals coupling of microtubule and actin movements in migrating cells. *J Cell Biol.* 158:31-37.

72. Waterman-Storer, C. M., and E. D. Salmon. 1997. Actomyosin-based retrograde flow of microtubules in the lamella of migrating epithelial cells influences microtubule dynamic instability and turnover and is associated with microtubule breakage and treadmilling. *J Cell Biol.* 139:417-434.
73. Brangwynne, C. P., F. C. MacKintosh, S. Kumar, N. A. Geisse, J. Talbot, L. Mahadevan, K. K. Parker, D. E. Ingber, and D. A. Weitz. 2006. Microtubules can bear enhanced compressive loads in living cells because of lateral reinforcement. *J Cell Biol.* 173:733-741.
74. Inoue, S., and E. D. Salmon. 1995. Force generation by microtubule assembly/disassembly in mitosis and related movements. *Mol Biol Cell.* 6:1619-1640.
75. Tran, P. T., L. Marsh, V. Doye, S. Inoue, and F. Chang. 2001. A mechanism for nuclear positioning in fission yeast based on microtubule pushing. *J Cell Biol.* 153:397-411.
76. Howard, J. 2006. Elastic and damping forces generated by confined arrays of dynamic microtubules. *Phys Biol.* 3:54-66.
77. Holy, T. E., M. Dogterom, B. Yurke, and S. Leibler. 1997. Assembly and positioning of microtubule asters in microfabricated chambers. *Proc Natl Acad Sci U S A.* 94:6228-6231.
78. Burakov, A., E. Nadezhdina, B. Slepchenko, and V. Rodionov. 2003. Centrosome positioning in interphase cells. *J Cell Biol.* 162:963-969.
79. Dujardin, D. L., and R. B. Vallee. 2002. Dynein at the cortex. *Curr Opin Cell Biol.* 14:44-49.
80. Zhu, J., A. Burakov, V. Rodionov, and A. Mogilner. 2010. Finding the cell center by a balance of dynein and myosin pulling and microtubule pushing: a computational study. *Mol Biol Cell.* 21:4418-4427.
81. Vogel, S. K., N. Pavin, N. Maghelli, F. Julicher, and I. M. Tolic-Norrelykke. 2009. Self-organization of dynein motors generates meiotic nuclear oscillations. *PLoS Biol.* 7:e1000087.
82. Bicek, A. D., E. Tuzel, A. Demtchouk, M. Uppalapati, W. O. Hancock, D. M. Kroll, and D. J. Odde. 2009. Anterograde microtubule transport drives microtubule bending in LLC-PK1 epithelial cells. *Mol Biol Cell.* 20:2943-2953.
83. Ingber, D. E. 2003. Tensegrity I. Cell structure and hierarchical systems biology. *J Cell Sci.* 116:1157-1173.

84. Palazzo, A. F., H. L. Joseph, Y. J. Chen, D. L. Dujardin, A. S. Alberts, K. K. Pfister, R. B. Vallee, and G. G. Gundersen. 2001. Cdc42, dynein, and dynactin regulate MTOC reorientation independent of Rho-regulated microtubule stabilization. *Curr Biol.* 11:1536-1541.
85. Kaufman, E. N., and R. K. Jain. 1990. Quantification of transport and binding parameters using fluorescence recovery after photobleaching. Potential for in vivo applications. *Biophys J.* 58:873-885.
86. Kaufman, E. N., and R. K. Jain. 1991. Measurement of mass transport and reaction parameters in bulk solution using photobleaching. Reaction limited binding regime. *Biophys J.* 60:596-610.
87. Mueller, F., T. S. Karpova, D. Mazza, and J. G. McNally. 2012. Monitoring dynamic binding of chromatin proteins in vivo by fluorescence recovery after photobleaching. *Methods Mol Biol.* 833:153-176.
88. Mueller, F., D. Mazza, T. J. Stasevich, and J. G. McNally. 2010. FRAP and kinetic modeling in the analysis of nuclear protein dynamics: what do we really know? *Curr Opin Cell Biol.* 22:403-411.
89. Phair, R. D., S. A. Gorski, and T. Misteli. 2004. Measurement of dynamic protein binding to chromatin in vivo, using photobleaching microscopy. *Methods Enzymol.* 375:393-414.
90. Phair, R. D., and T. Misteli. 2001. Kinetic modelling approaches to in vivo imaging. *Nat Rev Mol Cell Biol.* 2:898-907.
91. Stenoien, D. L., K. Patel, M. G. Mancini, M. Dutertre, C. L. Smith, B. W. O'Malley, and M. A. Mancini. 2001. FRAP reveals that mobility of oestrogen receptor-alpha is ligand- and proteasome-dependent. *Nat Cell Biol.* 3:15-23.
92. Wagner, S., S. Chiosea, M. Ivshina, and J. A. Nickerson. 2004. In vitro FRAP reveals the ATP-dependent nuclear mobilization of the exon junction complex protein SRm160. *J Cell Biol.* 164:843-850.
93. Deschout, H., J. Hagman, S. Fransson, J. Jonasson, M. Rudemo, N. Loren, and K. Braeckmans. 2010. Straightforward FRAP for quantitative diffusion measurements with a laser scanning microscope. *Opt Express.* 18:22886-22905.
94. Smisdom, N., K. Braeckmans, H. Deschout, M. vandeVen, J. M. Rigo, S. C. De Smedt, and M. Ameloot. 2011. Fluorescence recovery after photobleaching on the confocal laser-scanning microscope: generalized model without restriction on the size of the photobleached disk. *J Biomed Opt.* 16:046021.

95. Stasevich, T. J., F. Mueller, A. Michelman-Ribeiro, T. Rosales, J. R. Knutson, and J. G. McNally. 2010. Cross-validating FRAP and FCS to quantify the impact of photobleaching on in vivo binding estimates. *Biophys J.* 99:3093-3101.
96. Sprague, B. L., R. L. Pego, D. A. Stavreva, and J. G. McNally. 2004. Analysis of binding reactions by fluorescence recovery after photobleaching. *Biophys J.* 86:3473-3495.
97. Sprague, B. L., and J. G. McNally. 2005. FRAP analysis of binding: proper and fitting. *Trends Cell Biol.* 15:84-91.
98. Braeckmans, K., K. Remaut, R. E. Vandenbroucke, B. Lucas, S. C. De Smedt, and J. Demeester. 2007. Line FRAP with the confocal laser scanning microscope for diffusion measurements in small regions of 3-D samples. *Biophys J.* 92:2172-2183.
99. Kang, M., C. A. Day, E. DiBenedetto, and A. K. Kenworthy. 2010. A quantitative approach to analyze binding diffusion kinetics by confocal FRAP. *Biophys J.* 99:2737-2747.
100. Kang, M., C. A. Day, K. Drake, A. K. Kenworthy, and E. DiBenedetto. 2009. A generalization of theory for two-dimensional fluorescence recovery after photobleaching applicable to confocal laser scanning microscopes. *Biophys J.* 97:1501-1511.
101. Kang, M., and A. K. Kenworthy. 2008. A closed-form analytic expression for FRAP formula for the binding diffusion model. *Biophys J.* 95:L13-15.
102. van Royen, M. E., P. Farla, K. A. Mattern, B. Geverts, J. Trapman, and A. B. Houtsmuller. 2009. Fluorescence recovery after photobleaching (FRAP) to study nuclear protein dynamics in living cells. *Methods Mol Biol.* 464:363-385.
103. Russell, R. J., S. L. Xia, R. B. Dickinson, and T. P. Lele. 2009. Sarcomere mechanics in capillary endothelial cells. *Biophys J.* 97:1578-1585.
104. Chancellor, T. J., J. Lee, C. K. Thodeti, and T. Lele. Actomyosin tension exerted on the nucleus through nesprin-1 connections influences endothelial cell adhesion, migration, and cyclic strain-induced reorientation. *Biophys J.* 99:115-123.
105. Fink, J., M. Thery, A. Azioune, R. Dupont, F. Chatelain, M. Bornens, and M. Piel. 2007. Comparative study and improvement of current cell micro-patterning techniques. *Lab Chip.* 7:672-680.
106. Paddock, S. W., and G. Albrecht-Buehler. 1988. Rigidity of the nucleus during nuclear rotation in 3T3 cells. *Exp Cell Res.* 175:409-413.

107. Quintyne, N. J., S. R. Gill, D. M. Eckley, C. L. Crego, D. A. Compton, and T. A. Schroer. 1999. Dynactin is required for microtubule anchoring at centrosomes. *J Cell Biol.* 147:321-334.
108. King, S. J., C. L. Brown, K. C. Maier, N. J. Quintyne, and T. A. Schroer. 2003. Analysis of the dynein-dynactin interaction in vitro and in vivo. *Mol Biol Cell.* 14:5089-5097.
109. Toba, S., T. M. Watanabe, L. Yamaguchi-Okimoto, Y. Y. Toyoshima, and H. Higuchi. 2006. Overlapping hand-over-hand mechanism of single molecular motility of cytoplasmic dynein. *Proc Natl Acad Sci U S A.* 103:5741-5745.
110. Khatau, S. B., C. M. Hale, P. J. Stewart-Hutchinson, M. S. Patel, C. L. Stewart, P. C. Searson, D. Hodzic, and D. Wirtz. 2009. A perinuclear actin cap regulates nuclear shape. *Proc Natl Acad Sci U S A.* 106:19017-19022.
111. Yamada, M., S. Toba, T. Takitoh, Y. Yoshida, D. Mori, T. Nakamura, A. H. Iwane, T. Yanagida, H. Imai, L. Y. Yu-Lee, T. Schroer, A. Wynshaw-Boris, and S. Hirotsune. mNUDC is required for plus-end-directed transport of cytoplasmic dynein and dynactins by kinesin-1. *EMBO J.* 29:517-531.
112. They, M., V. Racine, M. Piel, A. Pepin, A. Dimitrov, Y. Chen, J. B. Sibarita, and M. Bornens. 2006. Anisotropy of cell adhesive microenvironment governs cell internal organization and orientation of polarity. *Proc Natl Acad Sci U S A.* 103:19771-19776.
113. Brock, A. L., and D. E. Ingber. 2005. Control of the direction of lamellipodia extension through changes in the balance between Rac and Rho activities. *Mol Cell Biomech.* 2:135-143.
114. Evans, E. 2001. Probing the relation between force--lifetime--and chemistry in single molecular bonds. *Annu Rev Biophys Biomol Struct.* 30:105-128.
115. Gennerich, A., A. P. Carter, S. L. Reck-Peterson, and R. D. Vale. 2007. Force-induced bidirectional stepping of cytoplasmic dynein. *Cell.* 131:952-965.
116. Gliksmann, N. R., R. V. Skibbens, and E. D. Salmon. 1993. How the transition frequencies of microtubule dynamic instability (nucleation, catastrophe, and rescue) regulate microtubule dynamics in interphase and mitosis: analysis using a Monte Carlo computer simulation. *Mol Biol Cell.* 4:1035-1050.
117. Shelden, E., and P. Wadsworth. 1993. Observation and quantification of individual microtubule behavior in vivo: microtubule dynamics are cell-type specific. *J Cell Biol.* 120:935-945.

118. Harper, S. M., L. C. Neil, and K. H. Gardner. 2003. Structural basis of a phototropin light switch. *Science*. 301:1541-1544.
119. Yao, X., M. K. Rosen, and K. H. Gardner. 2008. Estimation of the available free energy in a LOV2-J alpha photoswitch. *Nat Chem Biol*. 4:491-497.
120. Wang, X., L. He, Y. I. Wu, K. M. Hahn, and D. J. Montell. 2010. Light-mediated activation reveals a key role for Rac in collective guidance of cell movement in vivo. *Nat Cell Biol*. 12:591-597.
121. Machacek, M., L. Hodgson, C. Welch, H. Elliott, O. Pertz, P. Nalbant, A. Abell, G. L. Johnson, K. M. Hahn, and G. Danuser. 2009. Coordination of Rho GTPase activities during cell protrusion. *Nature*. 461:99-103.
122. Lauffenburger, D. A., and A. F. Horwitz. 1996. Cell migration: a physically integrated molecular process. *Cell*. 84:359-369.
123. Chen, W. T. 1981. Mechanism of retraction of the trailing edge during fibroblast movement. *J Cell Biol*. 90:187-200.
124. Amy, R. L., and R. Storb. 1965. Selective mitochondrial damage by a ruby laser microbeam: an electron microscopic study. *Science*. 150:756-758.
125. Kumar, S., I. Z. Maxwell, A. Heisterkamp, T. R. Polte, T. P. Lele, M. Salanga, E. Mazur, and D. E. Ingber. 2006. Viscoelastic retraction of single living stress fibers and its impact on cell shape, cytoskeletal organization, and extracellular matrix mechanics. *Biophys J*. 90:3762-3773.
126. Stachowiak, M. R., and B. O'Shaughnessy. 2009. Recoil after severing reveals stress fiber contraction mechanisms. *Biophys J*. 97:462-471.
127. Tanner, K., A. Boudreau, M. J. Bissell, and S. Kumar. 2010. Dissecting regional variations in stress fiber mechanics in living cells with laser nanosurgery. *Biophys J*. 99:2775-2783.
128. Heisterkamp, A., I. Z. Maxwell, E. Mazur, J. M. Underwood, J. A. Nickerson, S. Kumar, and D. E. Ingber. 2005. Pulse energy dependence of subcellular dissection by femtosecond laser pulses. *Opt Express*. 13:3690-3696.
129. Shen, N., D. Datta, C. B. Schaffer, P. LeDuc, D. E. Ingber, and E. Mazur. 2005. Ablation of cytoskeletal filaments and mitochondria in live cells using a femtosecond laser nanoscissor. *Mech Chem Biosyst*. 2:17-25.

130. Berns, M. W., J. Aist, J. Edwards, K. Strahs, J. Girton, P. McNeill, J. B. Rattner, M. Kitzes, M. Hammer-Wilson, L. H. Liaw, A. Siemens, M. Koonce, S. Peterson, S. Brenner, J. Burt, R. Walter, P. J. Bryant, D. van Dyk, J. Coulombe, T. Cahill, and G. S. Berns. 1981. Laser microsurgery in cell and developmental biology. *Science*. 213:505-513.
131. Gabel, C. V. 2008. Femtosecond lasers in biology: nanoscale surgery with ultrafast optics. *Contemporary Physics*. 49(6):391-411.
132. Colombelli, J., A. Besser, H. Kress, E. G. Reynaud, P. Girard, E. Caussinus, U. Haselmann, J. V. Small, U. S. Schwarz, and E. H. Stelzer. 2009. Mechanosensing in actin stress fibers revealed by a close correlation between force and protein localization. *J Cell Sci*. 122:1665-1679.
133. Lele, T. P., J. Pendse, S. Kumar, M. Salanga, J. Karavitis, and D. E. Ingber. 2006. Mechanical forces alter zyxin unbinding kinetics within focal adhesions of living cells. *J Cell Physiol*. 207:187-194.
134. Farhadifar, R., J. C. Roper, B. Aigouy, S. Eaton, and F. Julicher. 2007. The influence of cell mechanics, cell-cell interactions, and proliferation on epithelial packing. *Curr Biol*. 17:2095-2104.
135. Tinevez, J. Y., U. Schulze, G. Salbreux, J. Roensch, J. F. Joanny, and E. Paluch. 2009. Role of cortical tension in bleb growth. *Proc Natl Acad Sci U S A*. 106:18581-18586.
136. Mayer, M., M. Depken, J. S. Bois, F. Julicher, and S. W. Grill. 2010. Anisotropies in cortical tension reveal the physical basis of polarizing cortical flows. *Nature*. 467:617-621.
137. Moore, J. K., V. Magidson, A. Khodjakov, and J. A. Cooper. 2009. The spindle position checkpoint requires positional feedback from cytoplasmic microtubules. *Curr Biol*. 19:2026-2030.
138. Stiess, M., N. Maghelli, L. C. Kapitein, S. Gomis-Ruth, M. Wilsch-Brauninger, C. C. Hoogenraad, I. M. Tolic-Norrelykke, and F. Bradke. 2010. Axon extension occurs independently of centrosomal microtubule nucleation. *Science*. 327:704-707.
139. Colombelli, J., E. G. Reynaud, J. Rietdorf, R. Pepperkok, and E. H. Stelzer. 2005. In vivo selective cytoskeleton dynamics quantification in interphase cells induced by pulsed ultraviolet laser nanosurgery. *Traffic*. 6:1093-1102.
140. Wakida, N. M., C. S. Lee, E. T. Botvinick, L. Z. Shi, A. Dvornikov, and M. W. Berns. 2007. Laser nanosurgery of single microtubules reveals location-dependent depolymerization rates. *J Biomed Opt*. 12:024022.

141. Brangwynne, C. P., G. H. Koenderink, E. Barry, Z. Dogic, F. C. MacKintosh, and D. A. Weitz. 2007. Bending dynamics of fluctuating biopolymers probed by automated high-resolution filament tracking. *Biophys J.* 93:346-359.
142. Bicek, A. D., E. Tuzel, D. M. Kroll, and D. J. Odde. 2007. Analysis of microtubule curvature. *Methods Cell Biol.* 83:237-268.
143. Tao, W., R. J. Walter, and M. W. Berns. 1988. Laser-transected microtubules exhibit individuality of regrowth, however most free new ends of the microtubules are stable. *J Cell Biol.* 107:1025-1035.
144. Brangwynne, C. P., F. C. MacKintosh, and D. A. Weitz. 2007. Force fluctuations and polymerization dynamics of intracellular microtubules. *Proc Natl Acad Sci U S A.* 104:16128-16133.
145. Yamada, M., S. Toba, T. Takitoh, Y. Yoshida, D. Mori, T. Nakamura, A. H. Iwane, T. Yanagida, H. Imai, L. Y. Yu-Lee, T. Schroer, A. Wynshaw-Boris, and S. Hirotsune. 2010. mNUDC is required for plus-end-directed transport of cytoplasmic dynein and dynactins by kinesin-1. *EMBO J.* 29:517-531.
146. Landau, L. D., and E. M. Lifshitz. 1986. Theory of elasticity (Course of Theoretical Physics). Butterworth–Heinemann.
147. Manneville, J. B., M. Jehanno, and S. Etienne-Manneville. 2010. Dlg1 binds GKAP to control dynein association with microtubules, centrosome positioning, and cell polarity. *J Cell Biol.* 191:585-598.
148. Mitchison, T., and M. Kirschner. 1984. Dynamic instability of microtubule growth. *Nature.* 312:237-242.
149. Dogterom, M., J. W. Kerssemakers, G. Romet-Lemonne, and M. E. Janson. 2005. Force generation by dynamic microtubules. *Curr Opin Cell Biol.* 17:67-74.
150. Dogterom, M., and B. Yurke. 1998. Microtubule Dynamics and the Positioning of Microtubule Organizing Centers. *Phys. Rev. Lett.* 81:485-488.
151. Foethke, D., T. Makushok, D. Brunner, and F. Nedelec. 2009. Force- and length-dependent catastrophe activities explain interphase microtubule organization in fission yeast. *Mol Syst Biol.* 5:241.
152. Manneville, J. B., and S. Etienne-Manneville. 2006. Positioning centrosomes and spindle poles: looking at the periphery to find the centre. *Biol Cell.* 98:557-565.
153. Pinot, M., F. Chesnel, J. Z. Kubiak, I. Arnal, F. J. Nedelec, and Z. Gueroui. 2009. Effects of confinement on the self-organization of microtubules and motors. *Curr Biol.* 19:954-960.

154. Tolic-Norrelykke, I. M. 2010. Force and length regulation in the microtubule cytoskeleton: lessons from fission yeast. *Curr Opin Cell Biol.* 22:21-28.
155. Lindemann, C. B., and A. J. Hunt. 2003. Does axonemal dynein push, pull, or oscillate? *Cell Motil Cytoskeleton.* 56:237-244.
156. Benson, D. M., J. Bryan, A. L. Plant, A. M. Gotto, Jr., and L. C. Smith. 1985. Digital imaging fluorescence microscopy: spatial heterogeneity of photobleaching rate constants in individual cells. *J Cell Biol.* 100:1309-1323.
157. Rodrigues, I., and J. Sanches. 2010. Denoising of LSFCM images with compensation for the photoblinking/photobleaching effects. *Conf Proc IEEE Eng Med Biol Soc.* 2010:4292-4295.
158. Dragestein, K. A., W. A. van Cappellen, J. van Haren, G. D. Tsididis, A. Akhmanova, T. A. Knoch, F. Grosveld, and N. Galjart. 2008. Dynamic behavior of GFP-CLIP-170 reveals fast protein turnover on microtubule plus ends. *J Cell Biol.* 180:729-737.
159. Lele, T. P., and D. E. Ingber. 2006. A mathematical model to determine molecular kinetic rate constants under non-steady state conditions using fluorescence recovery after photobleaching (FRAP). *Biophys Chem.* 120:32-35.
160. Lele, T. P., C. K. Thodeti, J. Pendse, and D. E. Ingber. 2008. Investigating complexity of protein-protein interactions in focal adhesions. *Biochem Biophys Res Commun.* 369:929-934.
161. Sharp, Z. D., M. G. Mancini, C. A. Hinojos, F. Dai, V. Berno, A. T. Szafran, K. P. Smith, T. P. Lele, D. E. Ingber, and M. A. Mancini. 2006. Estrogen-receptor-alpha exchange and chromatin dynamics are ligand- and domain-dependent. *J Cell Sci.* 119:4101-4116.
162. Bulinski, J. C., D. J. Odde, B. J. Howell, T. D. Salmon, and C. M. Waterman-Storer. 2001. Rapid dynamics of the microtubule binding of ensconsin in vivo. *J Cell Sci.* 114:3885-3897.
163. Meyerzon, M., H. N. Fridolfsson, N. Ly, F. J. McNally, and D. A. Starr. 2009. UNC-83 is a nuclear-specific cargo adaptor for kinesin-1-mediated nuclear migration. *Development.* 136:2725-2733.
164. Schneider, M., W. Lu, S. Neumann, A. Brachner, J. Gotzmann, A. A. Noegel, and I. Karakesisoglou. 2010. Molecular mechanisms of centrosome and cytoskeleton anchorage at the nuclear envelope. *Cell Mol Life Sci.* 68:1593-1610.

165. Ralston, E., Z. Lu, N. Biscocho, E. Soumaka, M. Mavroidis, C. Prats, T. Lomo, Y. Capetanaki, and T. Ploug. 2006. Blood vessels and desmin control the positioning of nuclei in skeletal muscle fibers. *J Cell Physiol.* 209:874-882.
166. Toivola, D. M., G. Z. Tao, A. Habtezion, J. Liao, and M. B. Omary. 2005. Cellular integrity plus: organelle-related and protein-targeting functions of intermediate filaments. *Trends Cell Biol.* 15:608-617.
167. Wilhelmsen, K., S. H. Litjens, I. Kuikman, N. Tshimbalanga, H. Janssen, I. van den Bout, K. Raymond, and A. Sonnenberg. 2005. Nesprin-3, a novel outer nuclear membrane protein, associates with the cytoskeletal linker protein plectin. *J Cell Biol.* 171:799-810.
168. Fuchs, E., and I. Karakesisoglou. 2001. Bridging cytoskeletal intersections. *Genes Dev.* 15:1-14.
169. Prince, J. L., and R. B. Dickinson. 2003. Kinetics and Forces of Adhesion for a Pair of Capsular/Unencapsulated Staphylococcus Mutant Strains. *Langmuir.* 19 (1):154–159.
170. Lee, J., Y. L. Wang, F. Ren, and T. P. Lele. 2010. Stamp wound assay for studying coupled cell migration and cell debris clearance. *Langmuir.* 26:16672-16676.
171. Gupton, S. L., W. C. Salmon, and C. M. Waterman-Storer. 2002. Converging populations of f-actin promote breakage of associated microtubules to spatially regulate microtubule turnover in migrating cells. *Curr Biol.* 12:1891-1899.
172. Love, A. E. H. 1944. A treatise on the mathematical theory of elasticity. Dover.
173. Bicknese, S., N. Periasamy, S. B. Shohet, and A. S. Verkman. 1993. Cytoplasmic viscosity near the cell plasma membrane: measurement by evanescent field frequency-domain microfluorimetry. *Biophys J.* 65:1272-1282.
174. Fushimi, K., and A. S. Verkman. 1991. Low viscosity in the aqueous domain of cell cytoplasm measured by picosecond polarization microfluorimetry. *J Cell Biol.* 112:719-725.
175. Ladd, A. J. C., and G. Misra. 2009. A symplectic integration method for elastic filaments. *J Chem Phys.* 130:124909.

BIOGRAPHICAL SKETCH

Jun Wu was born in Chishui City, Guizhou Province, China in 1983 to Daili Wu and Songhui Liu. He graduated from Zunyi Hangtian High School in Zunyi, Guizhou Province, China in 2001. In 2005, he received a Bachelor of Science degree in chemical engineering and technology from Tianjin University, Tianjin, China. He joined Dr. Xinggong Li's group in the National Research Center of Distillation at Tianjin University and studied computational fluid dynamics of crystallization separation process. He received a Master of Science degree in chemical engineering from Tianjin University in 2007. He entered the PhD program in the Chemical Engineering Department at the University of Florida in August 2007 and joined Dr. Tanmay Lele's group in October 2007. His research was focused on microtubule and nuclear mechanics in fibroblasts and endothelial cells. He earned his Doctor of Philosophy in chemical engineering from the University of Florida in 2012.